International PhD Thesis

Ultrasensitive Magneto-Optical Ellipsometry for depth-resolved Magnetometry

Doctoral Programme in Physics of Nanostructures and Advanced Materials
University of the Basque Country UPV/EHU

PhD candidate	**Carmen Martín Valderrama**
Thesis advisors	**Dr. Andreas Berger** **Dr. Ane Martinez de Guereñu**

Donostia / San Sebastián, September 2025

eman ta zabal zazu

Universidad del País Vasco
Euskal Herriko Unibertsitatea

Abstract

The overarching goal of this thesis is to develop and demonstrate a robust experimental methodology capable of unambiguously detecting and characterizing depth-dependent vector magnetization states in nanoscale multilayers. This goal is motivated by the crucial role that non-collinear spin configurations play in existing and emerging spintronic technologies and the longstanding challenge of resolving them experimentally. As such, this thesis addresses one of today's key challenges in magnetism, given that no universal methodology exists that can address this characterization challenge, even though most relevant aspects of multilayer magnetism and associated technology rely on depth-dependent spin structures, which are, however, almost never measured directly.

To establish a reliable foundation for this work, several key methodological steps were undertaken. First, the reflection matrix $\boldsymbol{R}$ used in linear magneto-optics was experimentally verified for arbitrary magnetization orientations of a collinear materials system, which is crucially necessary to facilitate the utilization of experimental deviations from $\boldsymbol{R}$ in more complex magnetic sample structures. Next, a linear superposition approach of the magneto-optical signal of the individual layers was developed and verified, confirming that the total magneto-optical signal in multilayers can be understood as a coherent sum of individual layer contributions.

With this solid methodological groundwork, the following key results were achieved. Generalized magneto-optical ellipsometry was applied to detect non-collinear magnetic states in carefully designed multilayer samples. The results demonstrate that the phase of the complex-valued magneto-optical coefficients is highly sensitive to deviations from collinearity, allowing for the unambiguous identification of non-collinear depth-dependent magnetization profiles. Furthermore, full vector magnetometry was achieved on a layer-resolved basis for a two-layer system, revealing the independent and field-dependent rotation of magnetization vectors in multilayers with tunable interlayer coupling. Additionally, an unexpected out-of-plane magneto-optical signal was observed in nominally in-plane multilayer systems. This anomalous signal could not be accounted for by bilinear or biquadratic coupling alone and could instead be attributed to interlayer Dzyaloshinskii–Moriya interaction, as confirmed by simulations.

These results were made possible through extensive preparatory work, which included the design and fabrication of epitaxial single-layer and multilayer thin films with precise control over anisotropy, composition, and interlayer spacing and coupling. Structural characterizations via x-ray diffraction confirmed the crystalline quality and epitaxial alignment of the films. Complementing the experimental work, detailed simulations based on coupled macrospin models were performed to interpret the complex magnetic behavior of such multilayers. These simulations successfully reproduced the field evolution of vector magnetization states and explained the emergence of out-of-plane signals driven by interlayer Dzyaloshinskii–Moriya interactions.

Altogether, this thesis establishes a comprehensive framework for layer-resolved vector magnetometry and provides critical insights into the physics of magnetic multilayers.

Resumen

El objetivo central de esta tesis es desarrollar y demostrar experimentalmente una metodología robusta capaz de detectar y caracterizar los estados del vector magnetización en función de la profundidad en muestras constituidas por multicapas nanométricas. Este objetivo está motivado por el papel crucial que desempeñan las configuraciones de espín no colineales en las tecnologías espintrónicas existentes y emergentes, y por el reto que supone determinarlas experimentalmente. En este sentido, esta tesis aborda uno de los aspectos actuales más relevantes en el campo del magnetismo, dado que no existe una metodología universal que pueda abordar este desafío de caracterización. Y es que, a pesar de que los factores más relevantes del magnetismo multicapa y la tecnología asociada se basan en estructuras de espín dependientes de la profundidad, estas casi nunca se miden directamente.

Para establecer una base fiable para este trabajo, se llevaron a cabo varios pasos metodológicos clave. En primer lugar, se verificó experimentalmente la validez de la matriz de reflexión $\boldsymbol{R}$ utilizada en magnetoóptica lineal, para orientaciones de magnetización arbitrarias de un sistema colineal. Esto es crucial ya que permitirá utilizar e interpretar las desviaciones experimentales de $\boldsymbol{R}$ en estructuras magnéticas más complejas. A continuación, se desarrollaron y se estudiaron las desviaciones de la aproximación de superposición lineal de la señal magnetoóptica de las capas individuales, confirmando que la señal magnetoóptica total medida en muestras constituidas por multicapas se puede entender como la suma de las contribuciones de las capas individuales.

Con esta sólida base metodológica, se obtuvieron los siguientes resultados. Se aplicó la elipsometría magnetoóptica generalizada (GME) para detectar estados magnéticos no-colineales en muestras multicapa cuidadosamente diseñadas. Los resultados demuestran que la fase de los coeficientes magnetoópticos complejos es muy sensible a las desviaciones de la colinealidad, lo que permite identificar sin ambigüedad los perfiles de magnetización no colineales dependientes de la profundidad. No solo se identificaron estos estados no-colineales, sino que también se consiguieron cuantificar: se logró resolver el comportamiento vectorial de la magnetización de cada capa en un sistema de dos capas. Es decir, se obtuvo, en función del campo magnético

aplicado, la rotación de los vectores de magnetización de cada capa en multicapas con capas magnéticas acopladas entre sí de manera controlada y prediseñada. Además, se observó una inesperada señal magnetoóptica fuera del plano en sistemas multicapa nominalmente en el plano. Esta señal anómala no puede explicarse solo por el acoplamiento bilineal o bicuadrático, sino que puede atribuirse a la interacción Dzyaloshinskii-Moriya entre capas, lo que ha sido confirmado mediante simulaciones.

Estos resultados fueron posibles gracias al exhaustivo y minucioso trabajo preparatorio, que incluyó el diseño y la fabricación de películas delgadas epitaxiales mono- y multicapa con un control preciso de la composición, la anisotropía, el espaciado, y el acoplamiento entre capas. Las caracterizaciones estructurales mediante difracción de rayos x confirmaron la calidad cristalina y la alineación epitaxial de las películas. Como complemento al trabajo experimental, se realizaron simulaciones detalladas basadas en modelos macrospin acoplados para interpretar el complejo comportamiento magnético de dichas multicapas. Estas simulaciones reprodujeron con éxito la evolución de los estados de magnetización vectorial en función del campo magnético aplicado y explicaron la aparición de señales fuera del plano impulsadas por las interacciones Dzyaloshinskii-Moriya entre capas.

En conjunto, esta tesis establece un marco fundamental para la magnetometría vectorial resuelta por capas en la nanoescala y proporciona nuevas herramientas e información sobre la física de las multicapas magnéticas.

Table of contents

ABSTRACT ……… iii

RESUMEN ……… v

CHAPTER 1: INTRODUCTION ……… 3

Chapter references ……… 8

CHAPTER 2: FUNDAMENTAL ASPECTS: FERROMAGNETIC THIN FILMS AND MAGNETO-OPTICAL PROPERTIES ……… 11

2.1 Overview of ferromagnetism and magnetic interactions ……… 12

2.2 Magnetization reversal and macro-spin model ……… 18

2.3 Light-matter interaction: principles of magneto-optics ……… 21

Chapter references ……… 28

CHAPTER 3: EXPERIMENTAL METHODS ……… 31

3.1 Thin film fabrication ……… 32

3.2 Structural characterization ……… 38

3.3 Conventional magnetic characterization ……… 43

3.4 Generalized magneto-optical ellipsometry ……… 45

Chapter references ……… 53

CHAPTER 4: REFLECTION MATRIX VERIFICATION ……… 57

4.1 Introduction and motivation ……… 58

4.2 Sample design and fabrication ……… 61

4.3 Results and discussion ……… 65

4.4 Conclusions and outlook ……… 77

Chapter references ……… 78

CHAPTER 5: LAYER-RESOLVED VECTOR MAGNETOMETRY ……… 81

5.1 Introduction and motivation ……… 83

5.2 Sample design and fabrication ……… 84

5.3 Results and discussion ……… 92

5.4 Conclusions and outlook ……… 108

Chapter references ……… 110

CHAPTER 6: OTHER APPLICATIONS OF GME ……… 111

6.1 Anomalous P-MOKE behavior in asymmetric Co/Tb multilayers that can be consistently explained by topological MOKE ……… 112

6.2 Anomalous polar MOKE observation in ex-change-coupled uniaxial magnetic thin films……………………………………………………………………………………122
Chapter references……………………………………………………………………………132

CHAPTER 7: CONCLUSIONS AND OUTLOOK……………………………135

LIST OF ABBREVIATIONS……………………………………………………141

LIST OF VARIABLES……………………………………………………………142

LIST OF PUBLICATIONS ………………………………………………………145

ACKNOWLEDGEMENTS…………………………………………………………147

Chapter 1

Introduction

One of today's key challenges in nanoscale magnetism and spintronics is the experimental verification and exact knowledge of spatial magnetization or spin structures, especially in non-homogeneous material systems. This is relevant because many phenomena, such as interlayer exchange coupling [1], as well as high-tech devices like magnetic random access memory, are crucially linked to the existence of specific nm-length scale spin structures, especially along the depth of their structures. Examples of key technological devices, such as hard disk drive components, rely on magnetization depth profile patterns [2]. Moreover, current scientific questions are directly linked to the magnetization depth profile [3], such as transport-induced spin accumulations, which are understood to occur in spintronic devices and facilitate their operation [4–7]. However, in almost all experimental work, spin accumulation is simply assumed and inferred from magneto-electronic characteristics, but not experimentally verified. Thus, much of the accumulated scientific literature contains controversial results, given that the heart of the underlying physics, i.e., transport-induced spin structures, is not actually measured. Therefore, lateral and especially depth-resolved magnetometry is a crucial challenge within magnetism research today, given that magnetic responses at different depths cannot simply be isolated in all these so very relevant systems.

In this context, nanoscale magnetic multilayers have received enormous attention from the research community in the last decades due to the wide range of phenomena they exhibit [8–12], which differ from those of single-film systems. These unique properties are impacted by the individual layer behavior, multilayer-generated interfaces, and their collective responses to external stimuli [10,13]. Moreover, aspects related to fabrication and characterization have substantially improved the growth quality and associated functionalities [10,14–17]. Prominent examples of nanoscale magnetic multilayer systems include giant magneto-resistive (GMR) and tunneling magneto-resistive (TMR) sensors used in hard disk drives [18–20]. These technologies have enabled a massive and continuing increase in data storage capacity, thereby playing a central role in today's information-driven society.

Moreover, these next-generation technologies rely not only on nanoscale magnetic multilayer systems but on their depth-dependent magnetic configurations, where adjacent magnetization vectors may not be aligned. Such non-collinear magnetic configurations arise from competing anisotropies and interlayer exchange coupling [21–23] and are critical for enabling functionalities in applications as racetrack memory, reconfigurable magnetic logic, and field-free switching logic [24–29]. Figure 1.1 illustrates several cases where such depth-dependent collinear and non-collinear configurations are technologically and scientifically relevant.

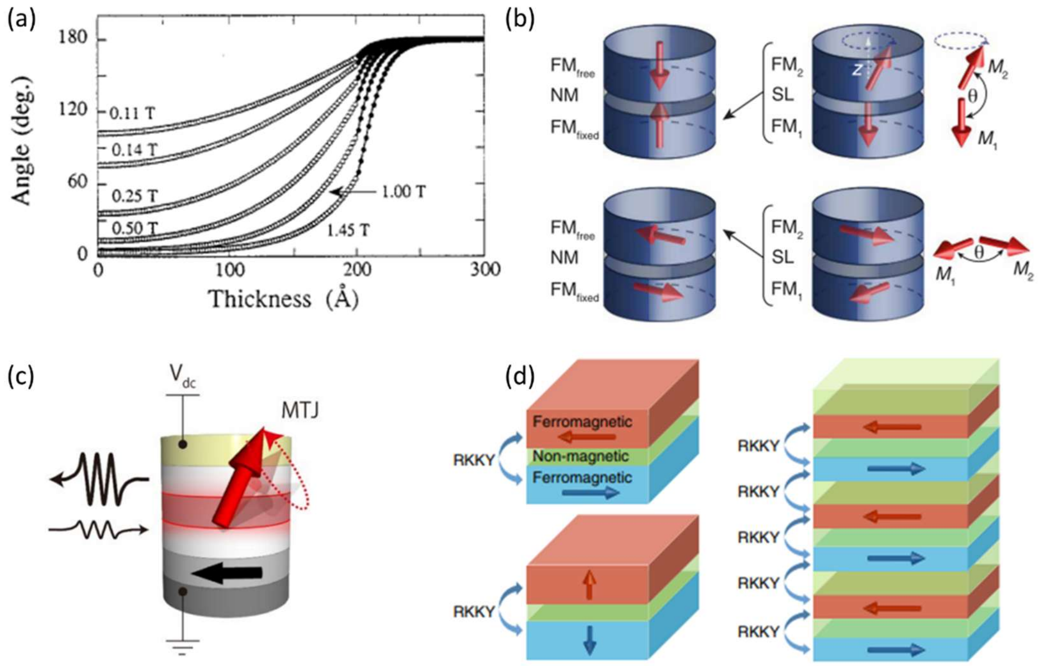

Figure 1.1 Examples demonstrating the technological and scientific relevance of depth-dependent magnetic configurations. (a) spin configuration determined from model calculations for Sm-Co/Fe (200 Å) [30]. *(b) non-collinear coupling structures to improve device applications* [23]. *(c) multilayer magnetic state for microwave amplification in a magnetic tunnel junction* [31]. *(d) schematic of synthetic antiferromagnets* [21].

Conventional static magnetic properties, as hysteresis loops, of the whole multilayer structure are generally determined by sensitive magnetometry measurements. Vibrating sample magnetometry (VSM) or superconducting quantum interference devices (SQUID) provide only volume-averaged measurements, lacking spatial resolution. However, it is often difficult to separate the magnetic contributions of all the involved ultrathin magnetic layers, while a clear interpretation of the physical properties and functionalities of these nanoscale devices requires such information. Despite their importance, the experimental characterization of such depth-dependent, layer-resolved vector magnetization states remains a major challenge. This is the key aspect to which my thesis is intended to make a meaningful contribution.

There are, nonetheless, some examples of analyzing the magnetic state of an individual subsurface layer in magnetic multilayers and doing so very precisely. The most successful technique is hereby x-ray magnetic circular dichroism (XMCD) [32–35]. However, despite its achievements, it has several limiting conditions: it is methodologically complex, needs large-scale facilities and sufficient highly expensive and highly competitive beamtimes. Moreover, it has elemental sensitivity and therefore layer-dependent magnetometry can only be achieved by means of XMCD if the magnetic layers of the structure have different elemental compositions, which is an additional limiting condition for many multilayer structures. Other x-ray-based techniques, such as x-ray magneto-optical Kerr effect or x-ray magnetic reflectivity, are presently being developed to serve as powerful tools for investigating magnetization depth profiles of specific magnetic elements in thin films and multilayers [35–37], given their potential to achieve sub-nanometer depth resolution. However, these techniques have not yet demonstrated their full potential, and furthermore, their data analysis will depend on magnetization depth profile models. The same can be said for polarized neutron reflectometry, which can achieve very good depth resolution but is also model-dependent, does not allow for a vector characterization of the magnetization, is generally time-consuming, and needs large-scale instruments [38,39]. These limitations highlight the need for more accessible and less assumption-dependent approaches.

Magneto-optical (MO) based techniques present a powerful and promising alternative. These methods are inherently sensitive to magnetization vector orientation [40]. Moreover, under appropriate conditions, they can distinguish layer-specific contributions [41–44]. MO-based techniques are widely used in magnetism and materials science by the applied physics community [41–43,45], as they are very sensitive to detect magnetism even in single atomic layers and can do so by utilizing widely applicable and cost-effective experimental setups. They have proven effective not only in simple ferromagnetic systems [46] but also in more complex magnetic order states [46–49]. Specifically, MO Kerr effect (MOKE) based techniques seem promising here due to their demonstrated ability to detect 3D vector magnetization [40], their sensitivity down to atomic-layer thickness [50], and the previously reported capacity for layer-resolved analysis in magnetic multilayers [41,51].

Among the developed MOKE techniques, generalized magneto-optical ellipsometry (GME) [40,52] is the most promising, given that it detects the full reflection matrix, i.e., the complete information that can be measured in a light reflection experiment. Moreover, it is non-destructive, contactless, applicable to a wide variety of material systems, does not have the limitation of being an element-specific technique, and does not inherently rely on model-dependent assumptions. Taking all of this into consideration, GME will be used in this study to further explore the capabilities of MO techniques and to test their ability to achieve layer-resolved vector magnetometry.

In this regard, the first step is to experimentally verify the reflection matrix $\boldsymbol{R}$ formalism, as it is the basis of the GME methodology and deviations from it would need appropriate interpretations. This experimental verification of the reflection matrix description in linear magneto-optics is done in Chapter 4. The reflection matrix is the result of rigorous albeit approximate theoretical derivations for numerous sample geometries and it has been extensively used, although its complete experimental verification had not been achieved due to limitations in simultaneous measurement of all matrix elements. By using a carefully designed and grown macrospin-type sample and exploiting the capabilities of GME, this chapter presents the accurate and precise verification of $\boldsymbol{R}$ for single layer magnetic films. This is crucially necessary to facilitate the utilization of experimental deviations from $\boldsymbol{R}$ in more complex magnetic sample structures for the purpose of developing and advancing MOKE characterization techniques.

Building on this foundation, Chapter 5 aims to achieve layer-resolved vector magnetometry. Starting from showing how deviations from $\boldsymbol{R}$ are related with non-collinear magnetic states in multilayers. Then, this non-collinear behavior is quantified for multilayer structures with two ferromagnetic (FM) layers. By measuring all complex-valued coefficients of $\boldsymbol{R}$ and applying a model of uncoupled (or partially coupled) macrospins, the angular evolution of the individual magnetization vectors of the two FM layers is overdetermined. Future steps towards disentangling the magnetization vectors of three FM layers in a multilayer system are also stated at the end of this chapter.

Accordingly, sample design, sample fabrication, and structural and other basic characterizations are a crucial part of this work as well, given that it provides the well-defined objects for the purpose of studying the methodology and the capabilities of GME. The fundamental aspects for the study of FM thin films and their MO properties are given in Chapter 2, and the experimental techniques and set-ups, with a focus on the GME, are presented in Chapter 3.

Lastly, given the exceptional capabilities of GME, unexpected MO observations are investigated in detail. This is included in Chapter 6, illustrating how GME is able to uncover the physical origin of emergent phenomena in multilayers related to topological MOKE observations and anomalous out-of-plane MOKE signals explained by interlayer DMI.

Finally, Chapter 7 synthesizes the conclusions of the thesis, summarizing how the GME methodology and the experimental characterization of depth-dependent, layer-resolved vector magnetization states give a framework for advanced MO analysis in nanomagnetism. An outlook is included with three different examples of complex magnetic systems started being studied with the GME. Figure 1.2 shows a general scheme of the thesis structure.

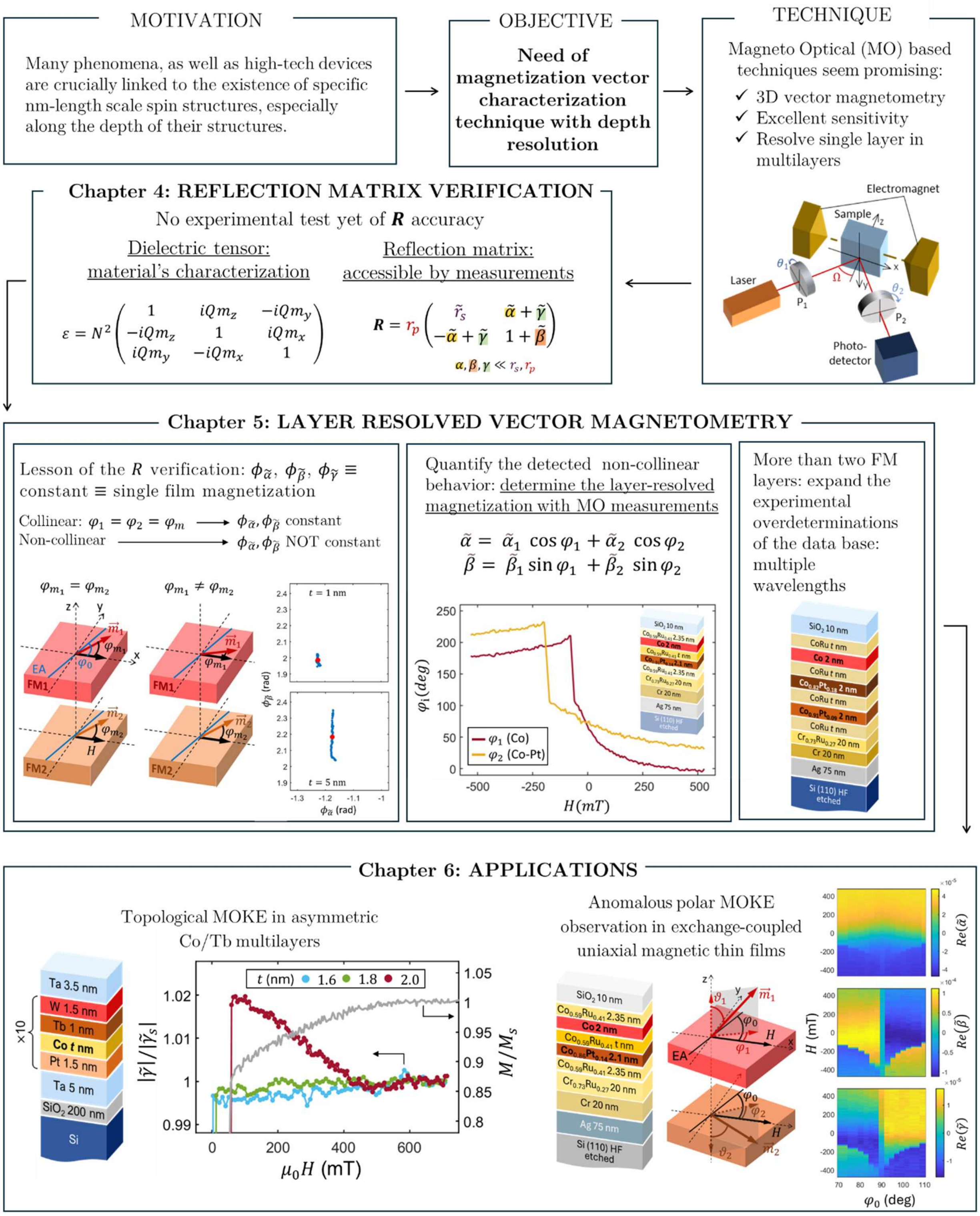

MOTIVATION

Many phenomena, as well as high-tech devices are crucially linked to the existence of specific nm-length scale spin structures, especially along the depth of their structures.

OBJECTIVE

Need of magnetization vector characterization technique with depth resolution

TECHNIQUE

Magneto Optical (MO) based techniques seem promising:

✓ 3D vector magnetometry
✓ Excellent sensitivity
✓ Resolve single layer in multilayers

Chapter 4: REFLECTION MATRIX VERIFICATION

No experimental test yet of ***R*** accuracy

Dielectric tensor: material's characterization

Reflection matrix: accessible by measurements

$$\varepsilon = N^2\begin{pmatrix} 1 & iQm_z & -iQm_y \\ -iQm_z & 1 & iQm_x \\ iQm_y & -iQm_x & 1 \end{pmatrix}$$

$$\boldsymbol{R} = r_p\begin{pmatrix} \tilde{r}_s & \tilde{\alpha}+\tilde{\gamma} \\ -\tilde{\alpha}+\tilde{\gamma} & 1+\tilde{\beta} \end{pmatrix}$$

$\alpha, \beta, \gamma \ll r_s, r_p$

Chapter 5: LAYER RESOLVED VECTOR MAGNETOMETRY

Lesson of the R verification: $\phi_{\tilde{\alpha}}$, $\phi_{\tilde{\beta}}$, $\phi_{\tilde{\gamma}} \equiv$ constant ≡ single film magnetization

Collinear: $\varphi_1 = \varphi_2 = \varphi_m \longrightarrow \phi_{\tilde{\alpha}}, \phi_{\tilde{\beta}}$ constant
Non-collinear $\longrightarrow \phi_{\tilde{\alpha}}, \phi_{\tilde{\beta}}$ NOT constant

Quantify the detected non-collinear behavior: determine the layer-resolved magnetization with MO measurements

$$\tilde{\alpha} = \tilde{\alpha}_1\cos\varphi_1 + \tilde{\alpha}_2\cos\varphi_2$$
$$\tilde{\beta} = \tilde{\beta}_1\sin\varphi_1 + \tilde{\beta}_2\sin\varphi_2$$

More than two FM layers: expand the experimental overdeterminations of the data base: multiple wavelengths

Chapter 6: APPLICATIONS

Topological MOKE in asymmetric Co/Tb multilayers

Anomalous polar MOKE observation in exchange-coupled uniaxial magnetic thin films

Figure 1.2 Scheme of the thesis structure, with the motivation, objective, main experimental technique and main results of the experimental chapters.

Chapter references

[1] P. Grünberg, R. Schreiber, Y. Pang, M. B. Brodsky, and H. Sowers, Layered Magnetic Structures: Evidence for Antiferromagnetic Coupling of Fe Layers across Cr Interlayers, Phys. Rev. Lett. **57**, 2442 (1986).

[2] A. Berger, N. Supper, Y. Ikeda, B. Lengsfield, A. Moser, and E. E. Fullerton, Improved media performance in optimally coupled exchange spring layer media, Appl. Phys. Lett. **93**, 122502 (2008).

[3] L. Fallarino, E. López Rojo, M. Quintana, J. S. Salcedo Gallo, B. J. Kirby, and A. Berger, Modifying Critical Exponents of Magnetic Phase Transitions via Nanoscale Materials Design, Phys. Rev. Lett. **127**, 147201 (2021).

[4] A. Fert, Nobel lecture: Origin, development, and future of spintronics nobel lecture: Origin, development, and future of spintronics, Rev. Mod. Phys. **80**, 1517 (2008).

[5] R. Wiesendanger, Nanoscale magnetic skyrmions in metallic films and multilayers: A new twist for spintronics, Nat. Rev. Mater. **1**, 16044 (2016).

[6] A. Hirohata, K. Yamada, Y. Nakatani, L. Prejbeanu, B. Diény, P. Pirro, and B. Hillebrands, Review on spintronics: Principles and device applications, J. Magn. Magn. Mater. **509**, 166711 (2020).

[7] A. Davidson, V. P. Amin, W. S. Aljuaid, P. M. Haney, and X. Fan, Perspectives of electrically generated spin currents in ferromagnetic materials, Phys. Lett. Sect. A Gen. At. Solid State Phys. **384**, 1 (2020).

[8] A. R. Fert, Magnetic and Transport Properties of Metallic Multilayers, Mater. Sci. Forum **59–60**, 439 (1991).

[9] W. Jiang, G. Chen, K. Liu, J. Zang, S. G. E. te Velthuis, and A. Hoffmann, Skyrmions in magnetic multilayers, Phys. Rep. **704**, 1 (2017).

[10] A. Sáenz-Trevizo and A. M. Hodge, Nanomaterials by design: A review of nanoscale metallic multilayers, Nanotechnology **31**, (2020).

[11] J. A. Arregi, P. Riego, A. Berger, and E. Y. Vedmedenko, Large interlayer Dzyaloshinskii-Moriya interactions across Ag-layers, Nat. Commun. **14**, 6927 (2023).

[12] R. Salikhov, F. Samad, S. Schneider, D. Pohl, B. Rellinghaus, B. Böhm, R. Ehrler, J. Lindner, N. S. Kiselev, and O. Hellwig, Multilayer Metamaterials with Ferromagnetic Domains Separated by Antiferromagnetic Domain Walls, Adv. Electron. Mater. **11**, 1 (2025).

[13] K. Stojak Repa, B. J. Kirby, and C. W. Miller, Tunable coupling in magnetic thin film heterostructures with a magnetic phase transition, Sci. Rep. **13**, 1 (2023).

[14] D. Sander et al., The 2017 Magnetism Roadmap, J. Phys. D. Appl. Phys. **50**, (2017).

[15] E. Y. Vedmedenko et al., The 2020 magnetism roadmap, J. Phys. D. Appl. Phys. **53**, 453001 (2020).

[16] F. J. Himpsel, J. E. Ortega, G. J. Mankey, and R. F. Willis, Magnetic nanostructures, Adv. Phys. **47**, 511 (1998).

[17] N. Lebbad, J. Voiron, B. Nguyen, and E. Chainet, Electrodeposition of metallic multilayers with modulated electric regimes, Thin Solid Films **275**, 216 (1996).

[18] J. Daughton, J. Brown, E. Chen, R. Beech, A. Pohm, and W. Kude, Magnetic Field Sensors Using GMR Multilayer, IEEE Trans. Magn. **30**, 4608 (1994).

[19] C. Reig, M. D. Cubells-Beltrán, and D. R. Muñoz, Magnetic field sensors based on Giant Magnetoresistance (GMR) technology: Applications in electrical current sensing, Sensors **9**, 7919 (2009).

[20] T. Nakatani, Z. Gao, and K. Hono, Read sensor technology for ultrahigh density magnetic recording, MRS Bull. **43**, 106 (2018).

[21] R. A. Duine, K. J. Lee, S. S. P. Parkin, and M. D. Stiles, Synthetic antiferromagnetic spintronics,

Nat. Phys. **14**, 217 (2018).

[22] X. Xie, X. Wang, W. Wang, X. Zhao, L. Bai, Y. Chen, Y. Tian, and S. Yan, Engineering Spin Configurations of Synthetic Antiferromagnet by Controlling Long-Range Oscillatory Interlayer Coupling and Neighboring Ferrimagnetic Coupling, Adv. Mater. **35**, 1 (2023).

[23] Z. R. Nunn, C. Abert, D. Suess, and E. Girt, Control of the noncollinear interlayer exchange coupling, Sci. Adv. **6**, eabd8861 (2020).

[24] S. S. P. Parkin, M. Hayashi, and L. Thomas, Magnetic Domain-Wall Racetrack Memory, Science (80-.). **320**, 190 (2008).

[25] W. He et al., Field-Free Spin-Orbit Torque Switching Enabled by the Interlayer Dzyaloshinskii-Moriya Interaction, Nano Lett. **22**, 6857 (2022).

[26] Z. Wang et al., Field-free spin-orbit torque switching of synthetic antiferromagnet through interlayer Dzyaloshinskii-Moriya interactions, Cell Reports Phys. Sci. **4**, 101334 (2023).

[27] Y. C. Li, Y. H. Huang, C. C. Huang, Y. T. Liu, and C. F. Pai, Field-Free Switching in Symmetry-Breaking Multilayers: The Critical Role of Interlayer Chiral Exchange, Phys. Rev. Appl. **20**, 1 (2023).

[28] C. Y. Lin, P. C. Wang, Y. H. Huang, W. B. Liao, M. Y. Song, X. Bao, and C. F. Pai, Field-Free Spin-Orbit Torque Switching via Oscillatory Interlayer Dzyaloshinskii-Moriya Interaction for Advanced Memory Applications, ACS Mater. Lett. **6**, 400 (2024).

[29] R. Lavrijsen, J. H. Lee, A. Fernández-Pacheco, D. C. M. C. Petit, R. Mansell, and R. P. Cowburn, Magnetic ratchet for three-dimensional spintronic memory and logic, Nature **493**, 647 (2013).

[30] E. E. Fullerton, J. S. Jiang, M. Grimsditch, C. H. Sowers, and S. D. Bader, Exchange-spring behavior in epitaxial hard / soft magnetic bilayers, **58**, 193 (1998).

[31] M. Goto, Y. Wakatake, U. K. Oji, S. Miwa, N. Strelkov, B. Dieny, H. Kubota, K. Yakushiji, A. Fukushima, and S. Yuasa, Microwave amplification in a magnetic tunnel junction induced by heat-to-spin conversion at the nanoscale, Nat. Nanotechnol. **14**, 3 (2019).

[32] G. Schütz, R. Wienke, W. Wilhelm, and E. Al., Spin-dependent x-ray absorption in Co / Pt multilayers and Co 50 Pt 50 alloy, J. Appl. Phys. **67**, 4456 (1990).

[33] P. Fischer and H. Ohldag, X-rays and magnetism, (n.d.).

[34] C. Donnelly and V. Scagnoli, Imaging three-dimensional magnetic systems with x-rays, J. Phys. Condens. Matter **32**, (2020).

[35] V. Bansal, J. M. Tonnerre, E. Mossang, L. Ortega, F. Fettar, J. Chatterjee, S. Auffret, I. L. Prejbeanu, and B. Dieny, Depth-resolved magnetization profile of MgO/CoFeB/W perpendicular half magnetic tunnel junctions, AIP Adv. **12**, 035129 (2022).

[36] V. Chardonnet et al., Toward ultrafast magnetic depth profiling using time-resolved x-ray resonant magnetic reflectivity, Struct. Dyn. **8**, 034305 (2021).

[37] M. Hennecke et al., Ultrafast element- and depth-resolved magnetization dynamics probed by transverse magneto-optical Kerr effect spectroscopy in the soft x-ray range, Phys. Rev. Res. **4**, L022062 (2022).

[38] G. P. Felcher, Polarized neutron reflectometry - a historical perspective, Phys. B **267–268**, 154 (1999).

[39] L. Fallarino, B. J. Kirby, M. Pancaldi, P. Riego, A. L. Balk, C. W. Miller, P. Vavassori, and A. Berger, Magnetic properties of epitaxial CoCr films with depth-dependent exchange-coupling profiles, Phys. Rev. B **95**, 134445 (2017).

[40] A. Berger and M. R. Pufall, Quantitative vector magnetometry using generalized magneto-optical ellipsometry, J. Appl. Phys. **85**, 4583 (1999).

[41] C. Martín Valderrama, M. Quintana, A. Martínez-De-Guerenu, T. Yamauchi, Y. Hamada, Y. Kurokawa, H. Yuasa, and A. Berger, Insertion layer magnetism detection and analysis using transverse magneto-optical Kerr effect (T-MOKE) ellipsometry, J. Phys. D. Appl. Phys. **54**, 435002 (2021).

[42] Z. Q. Qiu and S. D. Bader, Surface magneto-optic Kerr effect (SMOKE), J. Magn. Magn. Mater.

200, 664 (1999).

[43] A. Berger, S. Knappmann, and H. P. Oepen, Magneto-optical Kerr effect study of ac susceptibilities in ultrathin cobalt films, J. Appl. Phys. **75**, 5598 (1994).

[44] E. Oblak, P. Riego, L. Fallarino, A. Martínez-De-Guerenu, F. Arizti, and A. Berger, Ultrasensitive transverse magneto-optical Kerr effect measurements by means of effective polarization change detection, J. Phys. D. Appl. Phys. **50**, 23LT01 (2017).

[45] P. Riego, S. Tomita, K. Murakami, T. Kodama, N. Hosoito, H. Yanagi, and A. Berger, Enhanced magneto-optical Kerr effects in Py/Ag/Bi trilayers, J. Phys. D. Appl. Phys. **50**, 19LT01 (2017).

[46] A. Kimel, A. Zvezdin, S. Sharma, S. Shallcross, N. de Sousa, and A. García-Martín, The 2022 magneto-optics roadmap, J. Phys. D. Appl. Phys. **55**, 463003 (2022).

[47] T. Higo et al., Large magneto-optical Kerr effect and imaging of magnetic octupole domains in an antiferromagnetic metal, Nat. Photonics **12**, 73 (2018).

[48] T. Uchimura et al., Observation of domain structure in non-collinear antiferromagnetic Mn3Sn thin films by magneto-optical Kerr effect, Appl. Phys. Lett. **120**, (2022).

[49] S. Tomita, T. Suwa, P. Riego, A. Berger, N. Hosoito, and H. Yanagi, Enhanced Magneto-Optical Activities of Modulated Fe - Pt Multilayer Metamaterials, Phys. Rev. Appl. **11**, (2019).

[50] E. R. Moog and S. D. Bader, Smoke signals from ferromagnetic monolayers: p(1×1) Fe/Au(100), Superlattices Microstruct. **1**, 543 (1985).

[51] R. Weber, C. Martín Valderrama, L. Fallarino, and A. Berger, Dependence of the magneto-optical signal on the Co layer thickness asymmetry in Co/Pt/Co films, Phys. Rev. B **102**, 214434 (2020).

[52] A. Berger and M. R. Pufall, Generalized magneto-optical ellipsometry, Appl. Phys. Lett. **71**, 965 (1997).

Chapter 2

Fundamental aspects: Ferromagnetic thin films and magneto-optical properties

This chapter provides the fundamental aspects for the study of ferromagnetic (FM) thin films and their magneto-optical (MO) properties, as they will be referred to throughout this thesis. Important concepts are presented to establish a common understanding and provide context for the thesis, as well as for the establishment of a precise nomenclature; more detailed explanations are available in the cited literature.

This chapter is divided into three sections. Section 2.1 consists of an overview of ferromagnetism and magnetic interactions, including the key energy contributions and microscopic models governing the magnetic state. In Section 2.2 the process of magnetization reversal is explained, together with the magnetization behavior in the context of the macrospin model. Finally, the principles of light–matter interaction that give rise to MO effects are described in Section 2.3.

2.1 Overview of ferromagnetism and magnetic interactions

Magnetism has intrigued humankind for centuries. Already in ancient Greece, early knowledge of magnetism was present, as they knew a type of stone that could attract iron. Later, in China, but still a thousand years ago, magnetism was already applied in their technology, as in compasses. After quite some years, in the nineteenth century, the discovery of the relation between electricity and magnetism launched the electromagnetic revolution. Coming to the recent times, the most advanced applications of magnetism are closely related to the technology underlying magnetic storage and memory, which require well-controlled ultrathin metallic thin film structures. Today, there exists a fairly good knowledge about magnetism, but many open questions still remain [1,2].

The phenomenon of magnetism originates from the intrinsic (spin) and orbital angular momentum of electrons. The moments associated with each type of angular momentum have to be summed according to the rules of quantum mechanics. This gives rise to microscopic magnetic moments $\vec{\mu}$ [1]. Atoms with filled electronic shells lead to $\vec{\mu}$ equal to zero in the absence of an external field. In this case, an external magnetic field would induce a magnetic moment in the opposite direction. This is known as diamagnetism, an effect displayed in all materials, although not all materials are diamagnetic because other processes can overcome diamagnetism. It is reasoned by the classical electrodynamical effect that a magnetic field causes a circular current with itself that produces a magnetic field which is opposed to the inducing one. On the other hand, atoms with partially filled shells possess a non-zero $\vec{\mu}$. Now, when an external magnetic field $\vec{H}$ is applied, $\vec{\mu}$ tries to align parallel to it to minimize the energy, an effect called paramagnetism [1,3].

Macroscopically in solids, the net magnetic behavior depends on the interactions among these individual magnetic moments. The magnetic moment per unit volume is known as magnetization $\vec{M}$, which is the most used quantity to describe magnetic behavior in materials. There are two other magnetic field vectors that are used to describe magnetic-related effects, which are the magnetic field $\vec{H}$ and the magnetic induction $\vec{B}$. All three are related according to

$$\vec{B} = \mu_0\left(\vec{H} + \vec{M}\right) \tag{2.1}$$

with μ_0 being the permeability of free space.

How a material reacts to an external magnetic field $\vec{H}$ allows to classify it, as represented in Fig. 2.1. In diamagnetic materials, the individual magnetic moments are zero and

---

[1] Although protons and neutrons also have nuclear magnetic moments, these are significantly weaker in magnitude and are typically neglected in the context of solid-state magnetism.

$\vec{M}$ is zero for $\vec{H} = 0$. In paramagnetic materials, the individual magnetic moments are randomly oriented and also lead to $\vec{M} = 0$ in the absence of a field. The presence of an external magnetic field $\vec{H}$, leads generally to a linear response of $\vec{M}$ as,

$$\vec{M} = \chi \vec{H}, \tag{2.2}$$

where χ represents the magnetic susceptibility. For diamagnetic materials $\chi < 0$, and for paramagnetic materials $\chi > 0$, and therefore the magnetization being antiparallel or parallel to $\vec{H}$, respectively as illustrated in Fig. 2.1 [4,5].

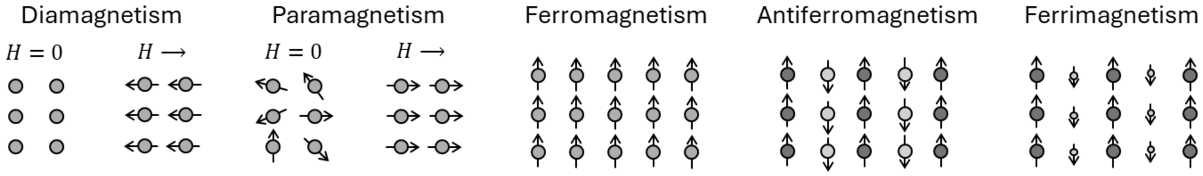

Figure 2.1. Types of magnetic order including diamagnetism, paramagnetism, ferromagnetism, antiferromagnetism, and ferrimagnetism, with the arrows representing the individual magnetic moments of the atoms.

In other types of materials, the atomic magnetic moments can interact with each other more strongly through the exchange interaction, leading to long-range magnetic ordering. Such ordering results in a non-linear relationship between $\vec{M}$ and $\vec{H}$, which is characteristic of ferromagnetism (see Fig. 2.1) and $\vec{M}$ can be non-zero even without external field $\vec{H}$. This particular $\vec{M}$ vs $\vec{H}$ relation is known as hysteresis loop. However, such long-range ordering of magnetic moments occurs only below a specific material-dependent temperature constant, known as Curie temperature T_C. When the temperature T exceeds T_C, the magnetic order is lost and $\vec{M} = 0$ in absence of $\vec{H}$, leading to a phase transition to a paramagnetic phase.

Antiferromagnets possess strongly interacting permanent magnetic moments generally oriented oppositely to their neighbors, such that the net magnetization is zero (see Fig. 2.1). Alignment of the magnetic moments can often be achieved at sufficiently large applied fields. If heated above the Neel temperature T_N of the antiferromagnet, it undergoes a phase transition to a paramagnetic phase.

In ferrimagnetic materials, sublattices of spins are antiparallel, as in antiferromagnetic materials, but unequal in magnitude, resulting in a net magnetization and therefore behaving similar as ferromagnets (see Fig 2.1).

Although this work focuses on ferromagnetic thin films and multilayers, it is important to note that additional interactions—such as the Dzyaloshinskii–Moriya interaction (DMI)—have to be taken into account and are responsible for more exotic types of magnetic order, including chiral and non-collinear spin textures [5]. Some of these interactions will be described in the next section and they will be addressed throughout the thesis.

2.1.1 Energy contributions in ferromagnetic materials

The primary mechanism behind ferromagnetism is the exchange interaction, a quantum mechanical effect resulting from the interplay between electrostatic (Coulomb) repulsion and the Pauli exclusion principle. The exchange interaction between the spins inside an atom is known as intra-atomic exchange and it determines the size of the atomic magnetic moments. Interatomic exchange between atomic magnetic moments ensures long-range magnetic order and determines the ordering (Curie or Néel) temperature.

The exchange interaction is the strongest magnetic interaction and is responsible for the alignment of the spin system. The effective exchange energy in the simplest case of a two electron system is given by $\mathcal{H}_{\text{bilinear}} = -J\,(\vec{S}_1 \cdot \vec{S}_2)$, where J is the exchange constant and $\vec{S}_1$ and $\vec{S}_2$ are the unit vectors of the spins ascribed to atoms 1 and 2. The sign of J determines whether the ground state is ferromagnetic ($J > 0$) or antiferromagnetic ($J < 0$) [5]. More generally, in extended lattices, this is generalized to the bilinear component of the Heisenberg Hamiltonian $\mathcal{H}_{\text{bilinear}} = -\sum_{(i,j)} J_{ij}\,(\vec{S}_{\text{i}} \cdot \vec{S}_{\text{j}})$, where the sum runs over interacting pairs and J_{ij} is the exchange integral between spins at sites i and j [1,5]. In multilayered systems, the exchange interaction can propagate across non-magnetic spacer layers, a phenomenon known as interlayer exchange coupling. This is well described by the Ruderman–Kittel–Kasuya–Yosida (RKKY) model [4–6], in which conduction electrons mediate an oscillatory interaction between magnetic layers. Depending on spacer thickness and material, this can yield ferromagnetic or antiferromagnetic coupling between layers. Thus, by modifying the interlayer thickness in the nanometer scale, the coupling can be finely tuned.

Additional to this bilinear exchange interaction, there is a non-collinear exchange known as biquadratic interaction that favors a perpendicular magnetization configuration, generally attributed to higher-order spin correlations. This energy contribution is expressed (for a two-electron system) as $\mathcal{H}_{\text{biquadratic}} = -J_2(\vec{S}_1 \cdot \vec{S}_2)^2$, with $J_2 < 0$.

Another exchange mechanism, particularly in systems with strong spin–orbit coupling and broken inversion symmetry, is the DMI antisymmetric exchange [6,7], which is described as $\mathcal{H}_{\text{DMI}} = -\vec{D}_{12} \cdot \vec{S}_1 \times \vec{S}_2$. This interaction induces a chirality, because $\vec{S}_1 \times \vec{S}_2$ depends on the sign of the angle formed by the two spins, and thus clockwise or counterclockwise rotations are not identical and one of them will be energetically favored depending on the DMI vector $\vec{D}_{12}$. DMI promotes canted spin configurations and can stabilize non-collinear spin textures, such as skyrmions, which are of significant interest for both fundamental studies and spintronic applications. Moreover, in recent years, ultrathin magnetic film systems have drawn considerable attention, as interfacial spins can also couple through the DMI mechanism when mediated by atoms with strong spin-orbit coupling in an adjacent metallic layer, a phenomenon known as "interfacial DMI".

Therefore, the exchange energy of many (multilayer) systems can be expressed as the sum of bilinear, biquadratic and DMI contributions. For a system of two spins $\vec{S}_1$ and $\vec{S}_2$, the exchange Hamiltonian can be written as

$$\begin{gathered}\mathcal{H}_{\text{ex}} = \mathcal{H}_{\text{bilinear}} + \mathcal{H}_{\text{biquadratic}} + \mathcal{H}_{\text{DMI}} = \\ = -J\left(\vec{S}_1 \cdot \vec{S}_2\right) - J_2\left(\vec{S}_1 \cdot \vec{S}_2\right)^2 - \vec{D}_{12} \cdot \vec{S}_1 \times \vec{S}_2.\end{gathered} \tag{2.3}$$

In addition to exchange, other key energy contributions determine magnetic behavior:

(i) Dipolar (magnetostatic) interactions, which originate from the magnetic field generated by one magnetic moment acting on another. Within the framework of classical electromagnetic theory, the corresponding dipolar Hamiltonian can be expressed as

$$\mathcal{H}_{\text{dip}} = -\frac{\mu_0}{2}\sum_{i\neq j} \vec{\mu}_i \cdot \vec{H}_{ij}^{dip}\,, \tag{2.4}$$

where $\vec{H}_{ij}^{dip}$ is the dipolar field at the position of $\vec{\mu}_i$, produced by $\vec{\mu}_j$. This field $\vec{H}_{ij}^{dip}$ is given by

$$\vec{H}_{ij}^{dip} = \frac{1}{4\pi}\frac{3\,\vec{r}_{ij}(\vec{\mu}_i \cdot \vec{\mu}_j)\text{-}\,\vec{\mu}_j\left|r_{ij}\right|^2}{\left|r_{ij}\right|^5}, \tag{2.5}$$

with $\vec{r}_{ij} = \vec{r}_i - \vec{r}_j$ being the vector connecting the i and j moments in two different lattice points. From Eq. (2.5), one can observe that dipole-dipole interactions are long-range in contrast to exchange interactions, although they are too weak to account for the ordering of most magnetic materials.

Given Eqs. (2.4)-(2.5), this magnetostatic energy is minimized when magnetic moments align parallel to the vectors connecting them. Thus, dipolar interactions tend to demagnetize any given structure, which is the reason why dipolar fields are referred to as demagnetizing fields as well.

In order to minimize both $\mathcal{H}_{dip}$ and $\mathcal{H}_{ex}$ at the same time, FM structures usually have magnetic domains separated by domain walls. In a uniformly magnetized structure, dipolar interactions are relatively large and favor the creation of separate domains with different magnetization vector orientations. But each domain created costs energy because of the domain wall, where the magnetic moments change from one direction to the other. So the formation of magnetic domains and the size of a domain wall is a balance between the dipolar energy and the exchange energy [1].

Dipolar interactions can also responsible for the formation of shape anisotropies. For example, in thin films, where the thickness is orders of magnitude smaller than the other two lateral dimensions, dipolar interactions favor the magnetic moments to align in the plane of the film. This specific fact is of particular relevance to this thesis, where thin films are of main importance, so having a single magnetic domain enables simple interpretations and magnetic characterizations of their properties.

(ii) Magneto-crystalline anisotropy, where the orientation of magnetic moments in a crystal is influenced by the crystal lattice itself. The spin–orbit interaction creates orbital magnetism and couples the spin system to the lattice, allowing energy and angular momentum exchange. The spin–orbit interaction is the very origin of magnetic anisotropy since the exchange interaction itself is isotropic and only the coupling of the spin to the lattice can “lock in” a macroscopic magnetization, making certain crystallographic directions energetically favorable for the alignment of magnetic moments, termed as easy axes (EA). Directions where the magnetization orientation is harder to orient or saturate are known as hard axes (HA) of the material. The crystal symmetry of the structure of the material can turn into uniaxial, biaxial or triaxial anisotropy, among others. A notable example that will be used in this thesis is hexagonal close-packed (hcp) Co, which shows a unique preferential magnetization along [0001] (c axis) and whose magnetization orientation dependence can be expressed as:

$$\begin{aligned}\mathcal{H}_K &= \sum_{i=1}^{N}\left(K_1\left(1-\left(\vec{S}_i\cdot\hat{e}\right)^2\right)+K_2\left(1-\left(\vec{S}_i\cdot\hat{e}\right)^2\right)^2+K_3\left(1-\left(\vec{S}_i\cdot\hat{e}\right)^2\right)^3\right)\\ &= \sum_{i=1}^{N}\left(K_1\sin^2(\varphi_0-\varphi_m)+K_2\sin^4(\varphi_0-\varphi_m)+K_3\sin^6(\varphi_0-\varphi_m)\right),\end{aligned} \tag{2.6}$$

where $\hat{e}$ is the unit vector of the uniaxial anisotropy axis, φ_0 and φ_m are the angles of $\hat{e}$ and $\vec{S}_i$ with respect to the applied field direction. In Fig 2.2(a) these angles are defined for a thin films with in-plane anisotropy; K_1, K_2 and K_3 are the first-, second- and third-order anisotropy constants [5,8], with units of energy. Only even terms are present in the expression because odd terms vanish due to time-inversion symmetry.

(iii) Zeeman interaction, which describes the interaction of magnetic moments with external magnetic fields. Its associated Hamiltonian is

$$\mathcal{H}_{\mathrm{Z}} = -\mu_0\sum_i \vec{\mu}_i\cdot\vec{H}_i, \tag{2.7}$$

Even though exchange interaction is the main energy contributor in ferromagnetic materials, the dipolar, magneto-crystalline anisotropy and Zeeman energy terms do also contribute to the magnetization direction, domain structure, and dynamic response to external stimuli. The interplay between all these contributions governs phenomena such as hysteresis, coercivity, and magnetization reversal, all of which will be mentioned in subsequent sections.

2.2 Magnetization reversal and macro-spin model

Considering the energy contributions discussed earlier, the full Hamiltonian for a ferromagnetic thin film can be expressed as the sum of exchange $\mathcal{H}_{ex}$, dipolar $\mathcal{H}_{dip}$, anisotropy $\mathcal{H}_K$ and Zeeman contributions $\mathcal{H}_Z$,

$$\mathcal{H} = \mathcal{H}_{ex} + \mathcal{H}_{dip} + \mathcal{H}_K + \mathcal{H}_Z + \dots \tag{2.8}$$

Further interactions can affect the magnetic state of a material, but are not considered for the purpose of this thesis. The equilibrium configuration of the system corresponds to a (local) minimum of the energy. Due to the presence of various competing energy contributions, the magnetic energy landscape is highly complex, often featuring many local minima.

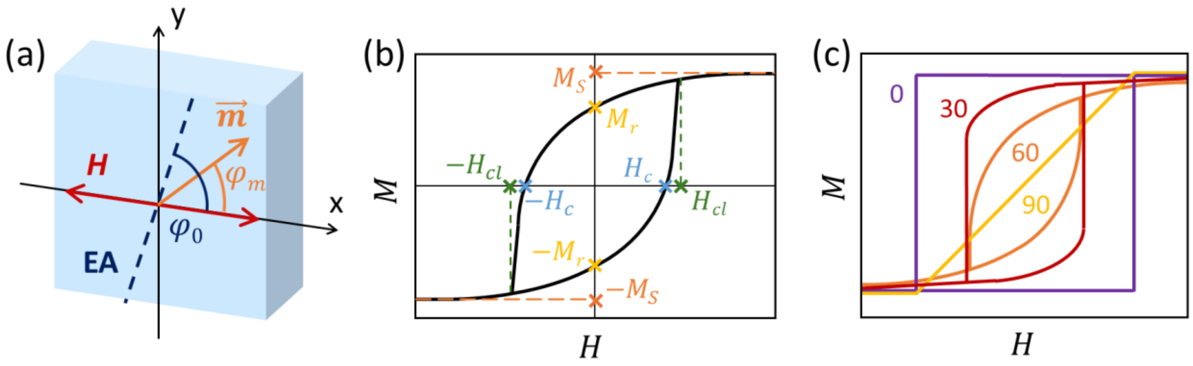

Figure 2.2 (a) Schematic of a FM thin film with in-plane EA (blue dashed line). The applied field H and the magnetization vector $\vec{m} = \vec{M}/M_s$ are indicated, as well as the angles φ_0 and φ_m of the EA and magnetization direction with respect to the applied field. (b) Representation of the projection of the magnetization on the applied field direction, a typical M(H) hysteresis loop, of a FM material with the relevant quantities indicated: the saturation magnetization M_s, the remanent magnetization M_r, the coercive field H_c and the closure field H_{cl}. (c) Exemplary hysteresis loops within the Stoner-Wohlfarth model for different orientations of the EA with respect to H, namely $\varphi_0 = 0, 30, 60,$ and 90 deg.

A typical magnetization characterization technique of a ferromagnetic material is the measurement of its field response to a cyclical magnetic field, which generally leads to the acquisition of M vs. H curves that exhibit hysteresis due to the existence of multiple energy minima, especially in the field range close to $H = 0$, where a ferromagnetic system undergoes a first order phase transition [1,4,5]. Figure 2.2(b) includes a hysteresis loop, representing the projection of M along the direction of an applied field H as a function of the field strength. When H is sufficiently large, the system reaches the saturation magnetization M_s, with all magnetic moments aligned with the field. Reducing the field to zero, a finite remanent magnetization M_r persists, reflecting the system's intrinsic magnetic order. Further increasing the field in the opposite direction, the magnetization undergoes a first order phase transition to the opposite orientation. This occurs at the coercive field H_c, and ultimately, the hysteresis loop closes at the closure field H_{cl} before reaching saturation again at negative large H values.

The hysteresis loop is fundamentally a manifestation of energy dissipation and the system's transition from metastable to stable states. Time-reversal symmetry of a FM requires that $M_{inc}(H) = -M_{dec}(-H)$, which implies that the hysteresis loop must be antisymmetric with respect to H and centered at zero field. Multiple microscopic mechanisms are commonly involved in the non-equilibrium process that is called magnetization reversal. They include domain nucleation, domain wall motion, domain annihilation and coherent rotation [9–11]. The dominant mechanism depends on the relative strength and geometry of the energy terms, sample dimensions, temperature and external applied fields. Ultimately, all these processes determine the shape of the hysteresis loop.

A simplified framework often used to describe the magnetization dynamics of ferromagnetic systems is the macrospin model, also known as the Stoner-Wohlfarth model [12]. Simplifications are made for the total Hamiltonian of Eq. (2.8) and a free energy $\mathcal{F}$ expression is proposed. This model assumes that the exchange interaction is sufficiently strong to maintain a uniform magnetization throughout the entire magnetic volume. Exchange interaction is thus a constant that does not modify the magnetization orientation dependence of $\mathcal{F}$ and is ignored in the model. As a result, the system can be modeled as a single, collective magnetic moment—called macrospin—with fixed magnitude $|\vec{M}|$, whose orientation varies coherently under the influence of anisotropy and external fields. Therefore, it is only valid for samples with negligible magnetostatic energy, as the thin film samples fabricated and studied in this thesis. Therefore, for thin films with in-plane anisotropy (characterized by an in-plane easy axis, EA), and under the assumption that both $\vec{H}$ and $\vec{M}$ lie in the film plane, the free energy density $\mathcal{F}/\mathrm{V}$ of a macrospin is given by

$$\frac{\mathcal{F}}{\mathrm{V}} = -\mu_0 M_s H\, cos(\varphi_m) + k_1 \sin^2(\varphi_0 - \varphi_m) + k_2 \sin^4(\varphi_0 - \varphi_m), \tag{2.9}$$

where φ_m is the angle between $\vec{M}$ and $\vec{H}$, and φ_0 is the angle between the EA and $\vec{H}$. Here, M_s is the saturation magnetization, and k_1 and k_2 are the anisotropy energy densities.

Minimization of $\mathcal{F}$ with respect to φ_m determines the equilibrium orientation of the magnetization $\vec{M}$. In order to better understand the mechanism of the SW model, Fig 2.2(c) shows four angles ($\varphi_0 = 0$, 30, 60 and 90 deg) that represent three different reversal behaviors, which are now being reviewed in more detail one by one:

Easy axis alignment with the field direction ($\varphi_0 = 0$ deg). In this configuration, the anisotropy and Zeeman energies compete in such a way that the magnetization is energetically confined to lie along the EA: only two stable or meta-stable magnetization orientations exist (parallel and antiparallel to the field). Reversal occurs abruptly via switching when the energy barrier vanishes, and the system can transition from the local metastable energy minimum (which vanishes at this point) into the global energy minimum yielding a rectangular hysteresis loop with coercivity set by the anisotropy field.

Easy axis perpendicular to field direction ($\varphi_0 = 90$ deg). The magnetization lies along the EA at zero field, with no net projection along the field direction. As the field increases, the Zeeman energy gradually forces $\vec{M}$ to rotate continuously toward the field direction, leading to a gradual increase in the projection of $\vec{M}$ along H, until at a sufficiently high field, where the magnetization becomes parallel to H. The process is smooth and reversible, with the critical field at which full alignment occurs known as the anisotropy field H_K.

Intermediate orientation ($\varphi_0 \neq 0, 90$ deg). In these cases, the magnetization reversal combines continuous rotation and abrupt switching. The exact nature of the reversal depends on the interplay between the Zeeman and anisotropy energies, which leads to more complex hysteresis behavior.

Despite its simplicity, the macrospin model provides valuable insights into the fundamental principles governing ferromagnetic reversal processes and serves as a starting point for more complex, multi-domain analyses. In general, this model and its extensions to multiple grains are useful, if a large part of the magnetic hysteresis loop is determined by a uniform magnetization state, so that large parts of associated data sets can be understood using these simple macrospin or macrospin array models.

2.3 Light-matter interaction: principles of magneto-optics

Magneto-optics describes how light interacts with magnetized materials, leading to a change in its intensity or polarization state [13,14]. In ferromagnetic systems, spin–orbit coupling causes the dielectric tensor to become magnetization dependent, as we will see later in this section. This magnetization sensitivity is exploited in MO based techniques, which provide a non-invasive means of probing magnetic states, phenomena and dynamics at the nanoscale.

The first observation of a MO effect dates back to 1845, when Michael Faraday found that linearly polarized light passing through a magnetized glass rod experienced a rotation in its polarization state [15,16]. This phenomenon, known as Faraday effect, constituted the first experimental confirmation of the electromagnetic nature of light and had a large influence in the subsequent development of the electromagnetic theory. About 30 years later, John Kerr observed the corresponding effect in reflection: when a polarized beam reflects off a magnetized surface, its polarization state changes [17–19]. This phenomenon was termed as the MO Kerr effect (MOKE). The origin of both effects is the same, and will be addressed in the following subsections, although I will focus on the reflection geometry (MOKE), as it will be the one used in this thesis.

As illustrated in Fig 2.3, when an incident linearly polarized light beam is reflected from a medium, the resulting reflected light has a modified polarization state, being generally elliptically polarized [2]. This change in the polarization of light in any medium (even when the sample is not magnetized) is due to pure optical effects [13]. This is represented in Fig 2.3 by E_i as a blue arrow and by E_r as a blue ellipse. Now, if the sample is magnetized, there is an additional small modification in the polarization state of the light reflected, that is dependent on the magnetization of the sample itself. The yellow solid ellipse represents this additional change in the polarization due to the sample having a magnetization M (yellow solid arrow); as the modification of the polarization state depends on the magnetization state, when it inverts to $-M$ (yellow dashed arrow), the additional change in the polarization of the reflected light is modified, as represented by the yellow dashed ellipse. Even though this change is very small [3], the M dependence allows to clearly differentiate it from the pure optical polarization change. The changes in polarization due to MOKE are typically quantified through the Kerr rotation angle (θ_{Kerr}) and ellipticity (ε_{Kerr}).

---

[2] If the light is not s- or p-polarized, and if the Fresnell coefficients have a phase difference.

[3] For ultrathin films, the rotation of the polarization is typically of the order of tens of millidegrees only. Yet, they have been proven to provide a versatile and very sensitive measure of the magnetization using a variety of experimental schemes.

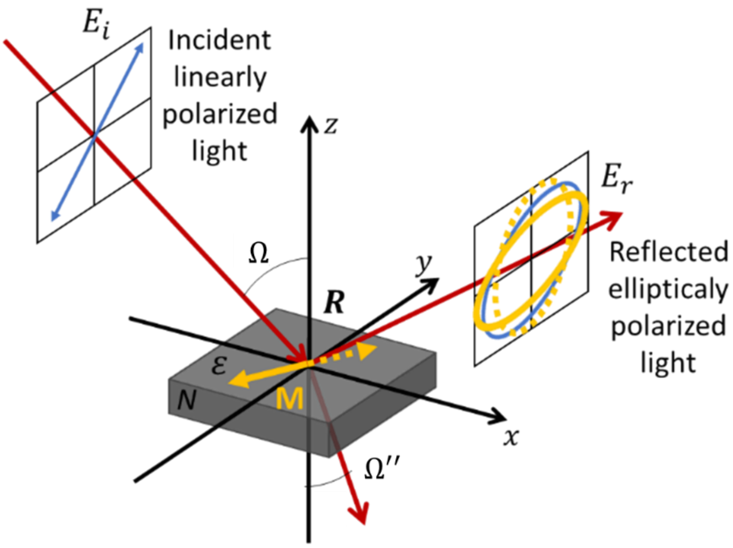

Figure 2.3 Scheme of the MOKE with the beam of light represented by the red arrows and the important concepts illustrated.

Besides the change in polarization, MOKE can also affect the intensity of the reflected light, under certain geometries. By analyzing how polarization and intensity change with the magnetization state of the sample [4] , detailed insights into its magnetic and magneto-optical properties can be extracted. Indeed, today, MOKE is a widely used tool for investigating the magnetic properties in FM and ferrimagnetic samples. It offers several advantages compared to other techniques [20]:

- High sensitivity: MOKE is extremely sensitive, making it competitive with the best magnetometries, particularly for studying the magnetism of ultrathin films. It can detect the magnetization of a fraction of an atomic layer of the FM material [21].

- Fast measurements: MOKE allows for rapid measurements, and because of the short duration of light-matter interaction, it enables time-resolved assessments of magnetization. Using a femtosecond pulsed laser, time resolutions as short as 100 femtoseconds have been achieved [22,23].

- Good lateral resolution: MOKE provides a lateral resolution of up to 0.2 µm, making it possible to observe magnetic domains and study the spatial distribution of magnetization in wedge samples or nanostructures, such as FM wires, patterned magnetic arrays, and self-organized magnetic structures [24].

- Depth sensitivity: MOKE can provide independent information on the magnetic states of several FM layers in a multilayer structure [25,26]. It probes samples at a depth equal

---

[4] How it changes with the applied magnetic field H, which is the quantity one can externally control and considering the linear relationship between H and M.

to the penetration depth of light, which is approximately 20 nm for metallic multilayer structures. Compared to integral techniques like superconducting quantum interference devices (SQUID) or vibrating sample magnetometry (VSM), MOKE is considered a surface-sensitive technique, often referred to as surface MOKE (SMOKE) [27,28]. However, in contrast to electron-based methods (e.g., spin-polarized LEED, STM, or photoemission), which are sensitive only to a few atomic layers at the surface, MOKE has to be considered as a magnetic in-depth sensitive technique allowing to study buried FM layers.

- Ease of use and cost-effectiveness: MOKE measurements are relatively easy and cheap to do. Furthermore, it is possible to investigate samples located at a "long distance" from the light source and the detector. This explains why MOKE is so popular to study thin film magnetism inside vacuum chambers or under extreme conditions (field, temperature, etc.).

2.3.1 Origin of MOKE and the dielectric tensor

The fundamental mechanism behind light–matter interaction upon reflection in solids is photon absorption (and subsequent photon emission) by electrons via electric dipole transitions. In FM materials, the initial electronic states are modified by magnetization: exchange interactions and spin–orbit coupling (SOC) cause a splitting of electronic energy levels [13,15]:

- The exchange interaction splits the energy levels of the electronic d-states having up or down spins (exchange is neglected for p-states). Assuming a FM material magnetized along the "up" direction, the up-spins electrons have lower energy than the down-spins electrons. In the example presented in Fig. 2.4(a), one can see the energy difference of d-state electrons having "up" (↑) and "down" (↓) spin orientation. In the notation $|l\ m\rangle$, l is the orbital number ($l = 1$ for p-states and $l = 2$ for d-states) and m stands for the magnetic number which takes integer values in the interval $(-l, l)$.
- The SOC breaks the degeneracy of both p or d states. Note that for up-spins, the energy increases with m, although the situation is reversed for down-spins (see Fig. 2.4(a)).

The combination of both splitting leads to different optical absorptions for left and right circularly polarized light (CPL), as illustrated in Fig. 2.4(b). Since linearly polarized light can be decomposed into equal components of left and right CPL, when it is reflected by a system with exchange and SOC splitting, the difference in absorption for right and left CPL and the associated phase shift results in the rotated elliptically polarized reflected light. This basic principle is depicted in Fig. 2.4(c).

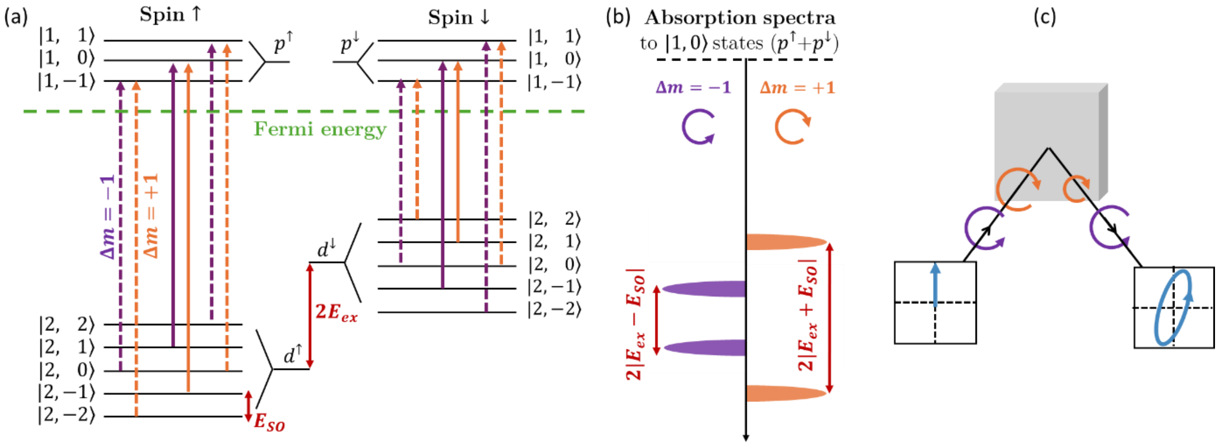

Figure 2.4 (a) Electronic states and electric dipole transitions (arrows) induced by left (purple) and right (orange) circularly polarized light. (b) indicates the absorption spectra to |1,0> states (continuous arrows in (a)), for opposite circular polarizations. (c) Basic principle of MOKE: in a magnetized material, left- and right-handed circularly polarized light have a different index of refraction, this causes that linearly polarized light experiences a rotation and becomes elliptic after reflection from a magnetized sample. Images adapted from [20,29,30].

Macroscopically, MOKE is generally described by the reflection matrix, but to calculate the reflection matrix, one needs first the description of the electromagnetic wave inside a ferromagnetic material, for which the dielectric tensor is needed. In optically isotropic materials, for non-magnetic materials, the dielectric tensor $\boldsymbol{\varepsilon}$ has the following description

$$\boldsymbol{\varepsilon} = N^2 \begin{pmatrix} 1 & 0 & 0 \\ 0 & 1 & 0 \\ 0 & 0 & 1 \end{pmatrix}, N = n - i\kappa, \tag{2.10}$$

with N being the refractive index of the medium, and n and κ the corresponding real and imaginary parts.

However, for a magnetized material, the interaction of light with magnetization modifies the optical properties of the material, as already explained. This is captured by a modified dielectric tensor, which describes how the material responds to the electric field of the incident light. For an optically and magneto-optically isotropic material and under linear optics approximation, the dielectric tensor is

$$\boldsymbol{\varepsilon} = N^2 \begin{pmatrix} 1 & iQm_z & -iQm_y \\ -iQm_z & 1 & iQm_x \\ iQm_y & -iQm_x & 1 \end{pmatrix}, \tag{2.11}$$

with Q being the MO coupling constant and (m_x, m_y, m_z) the cartesian components of the magnetization vector. Both N and Q are wavelength dependent complex quantities and the modifications of the dielectric tensor are limited to terms linear in the magnetization components.

For multilayer structures, the bulk N and Q parameters are considered valid for thin films [32]. Thus, a multilayer can be considered as a stack of homogeneous layers separated by sharp interfaces, such that the depth profile of the optical properties is step-like. Within this framework, the reflection matrix $\boldsymbol{R}$ of the entire multilayer structure can be calculated via the "4×4 transfer matrix" formalism [31], and it is indeed this reflection matrix $\boldsymbol{R}$ of a sample the experimentally accessible information by means of optical measurements.

2.3.2 Reflection matrix

While optical and magneto-optical characterization can allow one to determine the dielectric tensor, experimental observations typically provide direct access to the reflection matrix only. The reflection matrix is a mathematical representation that describes how the polarization state of light changes upon reflection [13]. For an optically isotropic sample, one can express it as

$$\boldsymbol{R} = \begin{pmatrix} r_s & 0 \\ 0 & r_p \end{pmatrix}, \tag{2.12}$$

with r_p and r_s being the Fresnell coefficients, $r_p = \frac{N cos\,\Omega - cos\,\Omega''}{N cos\,\Omega + cos\,\Omega''}$ and $r_s = \frac{cos\;\Omega - N cos\,\Omega''}{cos\,\Omega + N cos\,\Omega''}$, with Ω and Ω'' being the incident and refracted light angles. The subindexes p and s are associated to p- and s-polarization states of light, as defined in Fig 2.5 (a). For a magneto-optically active sample, limited to linear MO effects and under the assumption that $Q << N$, the reflection includes additional terms [14,32–34]:

$$\boldsymbol{R} = \begin{pmatrix} r_{ss} & r_{sp} \\ r_{ps} & r_{pp} \end{pmatrix}, \tag{2.13}$$

with

$$r_{ss} = \left(\frac{E_{r,s}}{E_{i,s}}\right) = \frac{\cos\Omega - N\cos\Omega''}{\cos\Omega + N\cos\Omega''}, \tag{2.14}$$

$$r_{sp} = \left(\frac{E_{r,s}}{E_{i,p}}\right) = -\frac{iNQ\cos\Omega\,(\cos\Omega'' m_z + \sin\Omega'' m_x)}{\cos\Omega''(N\cos\Omega + \cos\Omega'')(\cos\Omega + N\cos\Omega'')}, \tag{2.15}$$

$$r_{ps} = \left(\frac{E_{r,p}}{E_{i,s}}\right) = -\frac{iNQ\cos\Omega\,(\cos\Omega'' m_z - \sin\Omega'' m_x)}{\cos\Omega''(N\cos\Omega + \cos\Omega'')(\cos\Omega + N\cos\Omega'')}, \tag{2.16}$$

$$r_{pp} = \left(\frac{E_{r,p}}{E_{i,p}}\right) = \frac{N\cos\Omega - \cos\Omega''}{N\cos\Omega + \cos\Omega''} + \frac{2iNQ\cos\Omega\sin\Omega''}{N\cos\Omega + \cos\Omega''}m_y. \tag{2.17}$$

And the reflection matrix can be written as

$$\begin{aligned}\boldsymbol{R} = \begin{pmatrix} r_{ss} & r_{sp} \\ r_{ps} & r_{pp} \end{pmatrix} = \begin{pmatrix} r_s & \alpha + \gamma \\ -\alpha + \gamma & r_p + \beta \end{pmatrix} = r_p \begin{pmatrix} \tilde{r}_s & \tilde{\alpha} + \tilde{\gamma} \\ -\tilde{\alpha} + \tilde{\gamma} & 1 + \tilde{\beta} \end{pmatrix} = \\ = r_p \begin{pmatrix} \tilde{r}_s & \tilde{\alpha}_0 \cdot m_x + \tilde{\gamma}_0 \cdot m_z \\ -\tilde{\alpha}_0 \cdot m_x + \tilde{\gamma}_0 \cdot m_z & 1 + \tilde{\beta}_0 \cdot m_y \end{pmatrix},\end{aligned} \tag{2.18}$$

with α, β and γ being the MO coefficients related with each cartesian magnetization component m_x, m_y and m_z. These coefficients correspond to the three different Kerr geometries: longitudinal (L-MOKE), transverse (T-MOKE) and polar (P-MOKE). These three different configurations are defined by the orientation of the magnetization vector relative to the sample surface and the light plane of incidence, as illustrated in Fig 2.5.

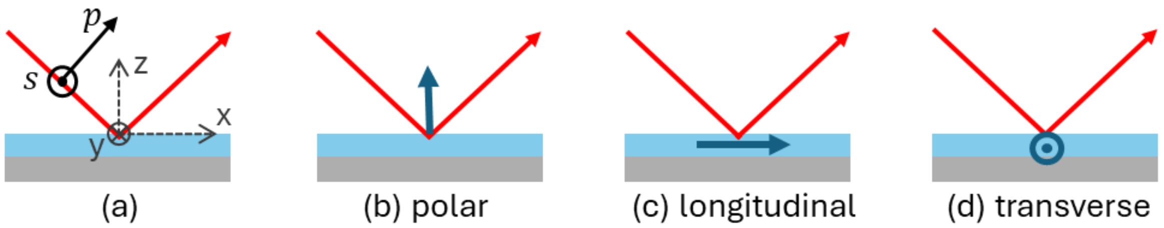

Figure 2.5 (a) Definition of s- and p-polarization. (b-d) three configurations of MOKE; (b) polar, (c) longitudinal and (d) transverse configuration. The red arrow represents the light path and the blue arrow the magnetization vector.

The relation between the experimentally determined quantities $\tilde{\alpha}$, $\tilde{\beta}$, $\tilde{\gamma}$ and $\tilde{r}_s$ of the sample and the material quantities N and Q for each layer of a multilayer sample can be determined utilizing the transfer matrix method [35]. This method focuses on the adequate description of the evolution of an electromagnetic wave in a multilayer stack, where boundary conditions in addition to Maxwell equations need to be fulfilled. A stack of layers can then be represented as a matrix system, which is defined altogether as a product of matrices belonging to each of the distinct layers composing the multilayer stack [31,35,36]. The knowledge of the system's "transfer matrix" allows recovering the reflection and transmission matrices that are accessible in an experimental setting. In this thesis I will focus on the parameters of the reflection matrix. Given that my primary focus is on magnetization vector characterization by means of MOKE, it is not necessary to extend the analysis to the actual dielectric tensor. Already the reflection matrix, Eq. 2.18., has sufficient vector component dependency and information, so that an analysis on the level of the dielectric tensor does not provide additional information as far as magnetization vector information is concerned.

Chapter references

[1] S. Blundell, *Magnetism in Condensed Matter* (Oxford University Press, UK, 2001).

[2] J. M. D. Coey, *Magnetism and Magnetic Materials* (Cambridge University Press, Cambridge 2010).

[3] N. W. Ashcroft and N. D. Mermin, *Solid State Physics* (Saunders College, Philadelphia, 1976).

[4] N. Spaldin, *Magnetic Materials: Fundamentals and Applications* (Cambridge University Press, Cambridge, 2010)

[5] R. Skomski, *Simple Models of Magnetism* (Oxford University Press, UK, 2008).

[6] I. Dzyaloshinsky, A Thermodynamic Theory of “weak” ferromagnetism of antiferromagnetics, J. Phys. Chem. Solids **4**, 241 (1958).

[7] T. Moriya, Anisotropic superexchange interaction and weak ferromagnetism, Phys. Rev. **120**, 91 (1960).

[8] M. T. Johnson, P. J. H. Bloemen, F. J. A. Den Broeder, and J. J. De Vries, Magnetic anisotropy in metallic multilayers, Reports Prog. Phys. **59**, 1409 (1996).

[9] A. Hubert and R. Schäfer, *Magnetic Domains. The Analysis of Magnetic Microstructures* (Springer-Verlag Berlin Heidelberg New York, Germany, 1998).

[10] X. Zhou, N. Vernier, G. Agnus, S. Eimer, W. Lin, and Y. Zhai, Highly Anisotropic Magnetic Domain Wall Behavior in In-Plane Magnetic Films, Phys. Rev. Lett. **125**, 237203 (2020).

[11] J. E. Davies, O. Hellwig, E. E. Fullerton, G. Denbeaux, J. B. Kortright, and K. Liu, Magnetization reversal of Co/Pt multilayers: Microscopic origin of high-field magnetic irreversibility, Phys. Rev. B - Condens. Matter Mater. Phys. **70**, 1 (2004).

[12] E. C. Stoner, F. R. S. Wohlfarth, and E. P. Wohlfarth, A mechanism of magnetic hysteresis in heterogeneous alloys, **240**, 826 (1948).

[13] G. R. Fowles, *Introduction to Modern Optics* (Dover, New York, 1989)

[14] J. Zak, E. R. Moog, C. Liu, and S. D. Bader, Universal approach to magneto-optics, **89**, 107 (1990).

[15] P. N. Argyres, Theory of the Faraday and Kerr effects in ferromagnetics, Phys. Rev. **97**, 334 (1955).

[16] M. J. Freiser, A Survey of Magnetooptic Effects, IEEE Trans. Magn. **MAG-4**, 152 (1968).

[17] J. Kerr, A new relation between electricity and light: Dielectrified media birefringent, Phil. Mag. **50**, 337 (1875).

[18] J. Kerr, On rotation of the plane of polarization by reflection from the pole of a magnet, Phil. Mag. **3**, 321 (1877).

[19] J. Kerr, On reflection of polarized light from the equatorial surface of a magnet, Phil. Mag. **5**, 161 (1878).

[20] J. Hamrle, *Magneto-optical determination of the in-depth magnetization profile in magnetic multilayers* (Ph.D. Thesis, University of Paris Sud, 2003).

[21] G. Pénissard, P. Meyer, J. Ferré, and D. Renard, Magneto-optic depth sensitivity to local magnetization in a simple ultrathin film structure, J. Magn. Magn. Mater. **146**, 55 (1995).

[22] A. Laraoui, M. Albrecht, and J.-Y. Bigot, Femtosecond magneto-optical Kerr microscopy, Opt. Lett. **32**, 936 (2007).

[23] G. P. Zhang, W. Hübner, G. Lefkidis, Y. Bai, and T. F. George, Paradigm of the time-resolved magneto-optical Kerr effect for femtosecond magnetism, Nat. Phys. **5**, 499 (2009).

[24] T. Uchimura et al., Observation of domain structure in non-collinear antiferromagnetic Mn3Sn thin films by magneto-optical Kerr effect, Appl. Phys. Lett. **120**, 172405 (2022).

[25] J. Hamrle, J. Ferré, and M. Nývlt, In-depth resolution of the magneto-optical Kerr effect in ferromagnetic multilayers, Phys. Rev. B - Condens. Matter Mater. Phys. **66**, 1 (2002).

[26] C. Martín Valderrama, M. Quintana, A. Martínez-De-Guerenu, T. Yamauchi, Y. Hamada, Y.

Kurokawa, H. Yuasa, and A. Berger, Insertion layer magnetism detection and analysis using transverse magneto-optical Kerr effect (T-MOKE) ellipsometry, J. Phys. D. Appl. Phys. **54**, 435002 (2021).

[27] Z. Q. Qiu, and S. D. Bader, "Surface magneto-optic Kerr effect (SMOKE)", J. Magn. Magn. Mater. **200**, 664 (1999)

[28] Z. Q. Qiu and S. D. Bader, Surface magneto-optic Kerr effect, Rev. Sci. Instrum. **71**, 1243 (2000).

[29] P. Bruno, Y. Suzuki, and C. Chappert, Magneto-optical Kerr effect in a paramagnetic overlayer on a ferromagnetic substrate: A spin-polarized quantum size effect, Phys. Rev. B - Condens. Matter Mater. Phys. **53**, 9214 (1996).

[30] J. A. Arregui, *Magneto-Optical Ellipsometry and Magnetometry of Thin Films and Multilayers* (Ph.D. Thesis, University of the Basque Country, 2020).

[31] P. Yeh, Optics of anisotropic layered media: A new 4 × 4 matrix algebra, Surf. Sci. **96**, 41 (1980).

[32] S. Višňovský, Magneto-optical ellipsometry, Czechoslov. J. Phys. **36**, 625 (1986).

[33] J. Zak, E. R. Moog, C. Liu, and S. D. Bader, Magneto-optics of multilayers with arbitrary magnetization directions, Phys. Rev. B - Condens. Matter Mater. Phys. **43**, 8 (1991).

[34] C.-Y. You and S.-C. Shin, Generalized analytic formulae for magneto-optical Kerr effects, J. Appl. Phys. **84**, 541 (1998).

[35] M. Schubert, T. E. Tiwald, and J. A. Woollam, Explicit solutions for the optical properties of arbitrary magneto-optic materials in generalized ellipsometry, Appl. Opt. **38**, 177 (1999).

[36] J. Zak, E. R. Moog, C. Liu, and S. D. Bader, Additivity of the Kerr effect in thin-film magnetic systems, J. Magn. Magn. Mater. **88**, 261 (1990).

Chapter 3
Experimental methods

This chapter provides a brief overview of the main experimental techniques employed in this thesis. It is divided into four sections, beginning with a description of the sample fabrication method used for thin films: the sputter deposition technique. The next two sections review structural characterization via x-ray techniques and magnetic characterization via vibrating sample magnetometry (VSM). The final section focuses on the magneto-optical (MO) characterization methodology central to this thesis, the generalized MO ellipsometry (GME).

3.1 Thin film fabrication

All the thin films and multilayers fabricated in this work have thicknesses on the nanometer scale. The design and fabrication of our epitaxial multilayer samples, with homogeneous and pre-designed inhomogeneous compositions layers, were devised and done for the purpose to have specific structural and magnetic properties. Due to its versatility and precision, sputter deposition is the technique used in this work to grow all the samples of this thesis.

3.1.1 Sputter deposition

Sputter deposition is a physical vapor deposition technique extensively used in nanotechnology and materials science due to its versatility, reproducibility, and ability to produce high-quality thin films with nanometric precision. Specifically, magnetron sputtering was selected as the method to fabricate metallic, insulating, and alloyed thin films, which will form multilayer structures with well-controlled thickness, composition, and magnetic properties [1–3].

The principle behind the sputter deposition process involves bombarding a solid target material with energetic ions generated in a plasma, resulting in the ejection of atoms from the target which are then deposited onto a substrate. A schematic representation of the mechanism can be observed in Fig. 3.1. This process is generally conducted in an ultra-high vacuum (UHV) chamber to prevent contamination and oxidation during film growth.

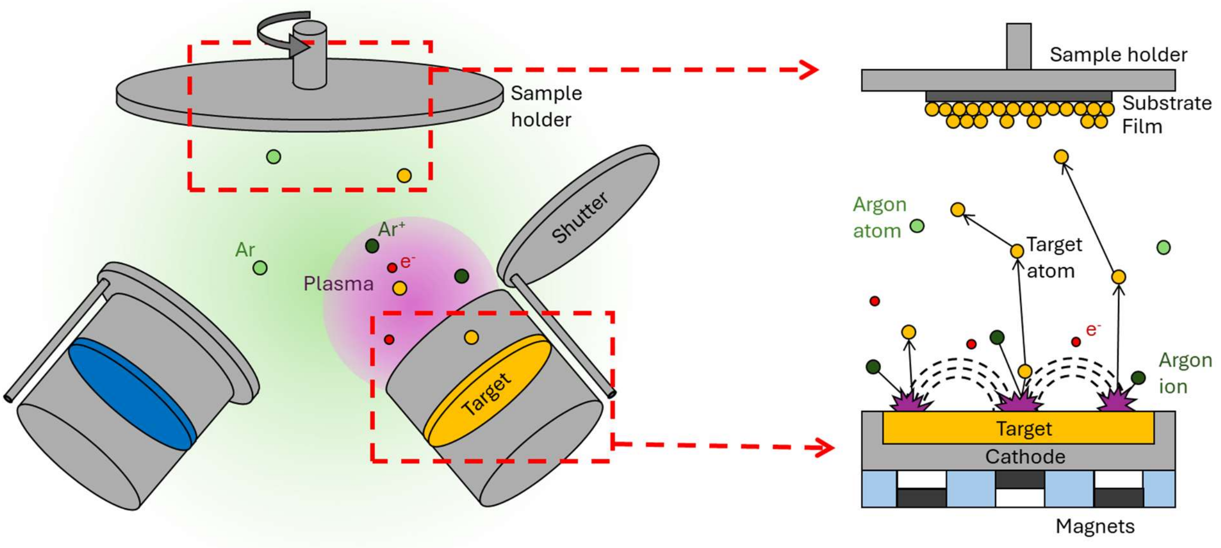

Figure 3.1 Schematic of the sputter deposition system and procedure, with the elements indicated. It shows the plasma composed of Ar+ ions and free electrons, the guns with material targets and shutters and the substrate in the rotating sample holder.

To initialize the process, a suitable pressure of an appropriate gas is introduced into the UHV chamber. In this work, the inert gas argon (Ar) is used in order to avoid unwanted chemical reactions with either the targets or the growing films. Once a suitable argon pressure is established in the UHV chamber (typically 3 mTorr in our experiments), a high voltage is applied between the cathode (material target) and anode (chamber wall), moving the ions to the target and the electrons away from the target. These movements then create a large and stable number of ions in a plasma, which maintains the process and makes the sputtering approach efficient.

Under these plasma conditions, the generated Ar+ ions are accelerated towards the negatively charged target, mechanically eroding it and causing atoms to be ejected from the target surface. These atoms travel away from the target and coat an appropriately positioned substrate. The deposition rates depend primarily on the number of ions colliding with the target, the cohesion energy of the target material, the atomic mass of the target atoms and the pressure (because the mean free path of the ejected atoms depends strongly on it).

Additionally, a set of permanent magnets behind the target generates a magnetic field parallel to the target surface (see Fig. 3.1, right side). The crossed electric and magnetic fields trap electrons in closed helical paths, increasing their path length and collision probability, thereby sustaining the high-density plasma and enhancing deposition efficiency [4].

Depending on the electrical conductivity of the target, sputtering can be performed using either direct current (DC) or radio-frequency (RF) power supplies. DC sputtering is effective for conductive targets. For insulating materials, DC power would result in charge accumulation and plasma extinction. Instead, RF sputtering is required, as it prevents charge buildup on the target surface by periodically reversing the field direction. Under RF conditions, Ar+ ions impact the target surface during the negative half-cycle of the RF signal, resulting in generally lower deposition rates. For this reason, RF power is also used for metals when precise, low-rate deposition is needed, as for ultrathin layers. All thin films presented in this work were deposited using an ATC Series UHV sputtering system from AJA International, Inc. In Fig. 3.2 we can see an image of the sputtering tool as well as an image from the inside of the main chamber. The system features:

- A load-lock chamber for substrate introduction, and a main deposition chamber, separated by a gate valve to maintain base pressure below 10^{-8} Torr, where the sputtering process is performed.
- Seven sputtering guns (with four DC and two RF power supplies), allowing the deposition of multiple materials without breaking the vacuum. Moreover, simultaneous co-sputtering of up to six materials is possible, a feature particularly useful for the fabrication of alloys. All guns have adjustable tilt angles, to optimize deposition geometry and enabling the creation of complex multilayer structures, and motorized shutters, enabling plasma ignition without deposition. Pre-sputtering with the shutters closed is routinely performed to remove surface oxides from targets.
- A rotating substrate holder to ensure uniform film thickness across the sample and avoid lateral non-uniformities.
- Heating system up to 850°C prior, during or after the sample is grown, although this key feature is not used for the work presented in this thesis.

- Complete electronic control via PHASE II software, enabling programmable recipes with precise timing, power modulation, shutters and gas flow control.

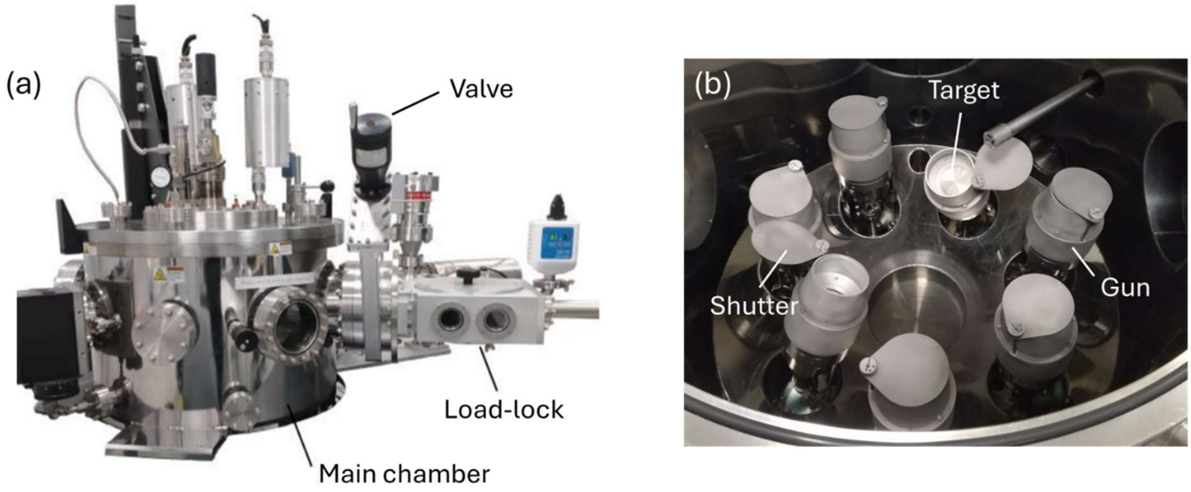

Figure 3.2 Images of the sputtering tool (a) and the inside of the main chamber (b). The main components are included: the main chamber, the load-lock, and the separation valve between them in (a), and the guns with the material targets and shutters in (b).

3.1.2 Thickness calibration

Accurate determination of the deposition rate for each material is essential to ensure precise control over the thickness and composition of thin films and multilayer structures. In this work, deposition rate calibrations were performed systematically for all target materials used in the fabrication process after every system modification, such as target change and maintenance.

The calibration procedure that we perform consists of preparing single-layer films with varying deposition times while keeping all other sputtering conditions constant. The film thickness is then measured with high accuracy via x-ray reflectivity (see Section 3.2.), which allows one to obtain the deposition rate at a certain sputtering power.

Figure 3.3 illustrates the overall target calibration. The thickness is plotted as a function of deposition time in Fig. 3.3(a), with the Ag being deposited using a DC power of 40 W and Cr at 80 W. The data points for each material fall on a straight line, indicating a constant deposition rate and confirming the high temporal stability of the sputtering process. The slope of the linear fit (red dashed lines in Fig. 3.3(a)) corresponds directly to the deposition rate in nm/s.

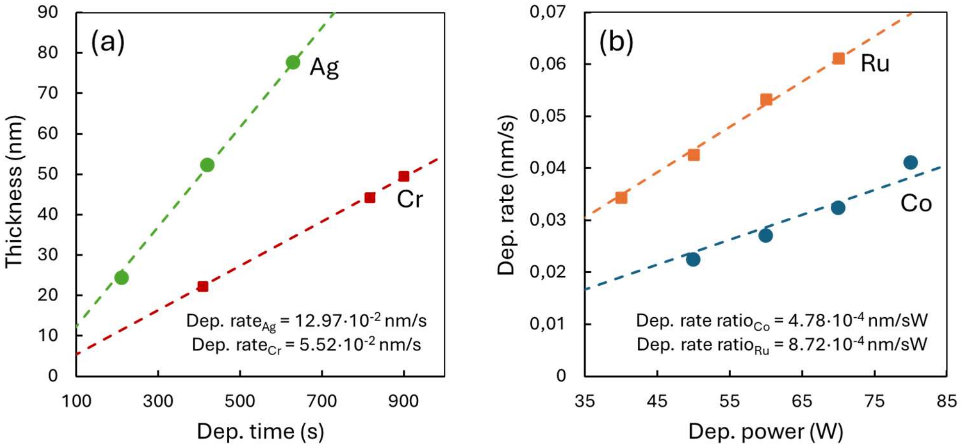

Figure 3.3 (a) Ag and Cr thicknesses as a function of the deposition time, for several thin films grown on naturally oxidized Si wafers with a DC power of 40 W and 80 W, respectively. (b) Calculated deposition rate of Co and Ru as a function of the DC deposition power.

An important consideration in this analysis is the influence of the shutter opening/closing. Since each deposition begins and ends by opening and closing the gun shutter, any delay could introduce a systematic error in the effective deposition time. However, the motorized shutters used in our system open and close in far less than one second, which is negligible compared to typical deposition durations (ranging from several tens of seconds to minutes). The observed linearity of the calibration curves validates that this timing uncertainty does not significantly affect the results.

This procedure is repeated for different DC power supply values. Figure 3.3(b) shows the deposition rates of Co and Ru as a function of power. A linear dependence is observed over an extended range, allowing for the extrapolation or interpolation of deposition conditions. Such a calibration scheme enables the accurate design of thin films, multilayer structures and alloys with well-defined thicknesses and dopant concentrations.

Indeed, to fabricate alloy thin films with controlled stoichiometry a co-sputter procedure is performed. In this process, distinct material targets are sputtered simultaneously, and their respective deposition rates are adjusted to achieve a precise target composition. For alloys with the form $A_{1-x}B_x$, with x being the concentration of B, the deposition rates are calculated taking into account the following relation,

$$\frac{dep.\ rate_B}{dep.\ rate_A} = \frac{x}{1-x}\frac{\rho_A}{\rho_B}\frac{m_B}{m_A}\,, \tag{3.1}$$

where, $\rho_{A,B}$ and $m_{A,B}$ are the room temperature densities and standard atomic masses of the materials A and B, respectively. In this way, the deposition rates of the two materials are obtained, with the total deposition rate of the alloy being the sum of the two deposition rates, which are experimentally verified, and thus the sputter guns do not impact each other. Also, co-sputter deposition is done considering the positions of the guns, as neighboring sputter guns are not used for alloy fabrication to limit any possible source of interference.

3.1.3 Epitaxial growth

In general, sputtering is used to grow thin films exhibiting either polycrystalline or amorphous microstructures. However, precise control over the crystallographic orientation of films and multilayers is possible with sputtering techniques. This requires epitaxial growth, which can be achieved with appropriate substrates and/or intermediate layers [5-8].

Epitaxial growth consists of depositing a material so that the new layers have a crystal structure with a well-defined orientation with respect to that of the substrate at the interface [5-8]. Both crystalline lattices need to be compatible, in terms of the crystallographic symmetry and lattice dimensions. For this reason, epitaxy is generally performed on single-crystal substrates. Another factor to take into consideration for epitaxy to occur is that the materials involved must be chemically stable with respect to one another, to prevent interfacial reactions, and limit diffusion or alloy formation during growth.

In the case that the film of the material of interest and the substrate show incompatible lattice structures or dimensions, one can utilize an epitaxial growth sequence in which intermediate layers are employed between the substrate and the targeted film structure [5-8]. This is the strategy that was followed here in order to grow epitaxial hexagonal close-packed (hcp) Co $(10\bar{1}0)$ films (and related alloy films and multilayers) onto (110) single-crystal Si substrates. The specific sequential epitaxial strategy was previously devised in the group [5–8] and it consists of Ag (110) and Cr (211) films. The corresponding lattice planes and crystal dimensions can be observed in Fig. 3.4 and consist of:

- First Ag (110) is deposited onto the clean Si (110) substrate. Ag has a face-centered cubic (fcc) structure with good lattice match to Si (110).
- Then Cr (211) is deposited, having a body-centered cubic (bcc) structure it aligns well with Ag (110).
- Finally, Co or Co alloys $(10\bar{1}0)$ are deposited on the Cr (211) layer.

An intermediate layer of CrRu (211) is included between the Cr and Co alloy layers if the material of interest is a CoRu $(10\bar{1}0)$ alloy film. The interest of the specific $(10\bar{1}0)$ surface orientation of Co and Co alloys is the c-axis of hcp Co for this surface orientation. It lies within the film plane, and as it represents the easy axis of magnetization, it enables the design of samples with strong in-plane uniaxial magnetic anisotropy.

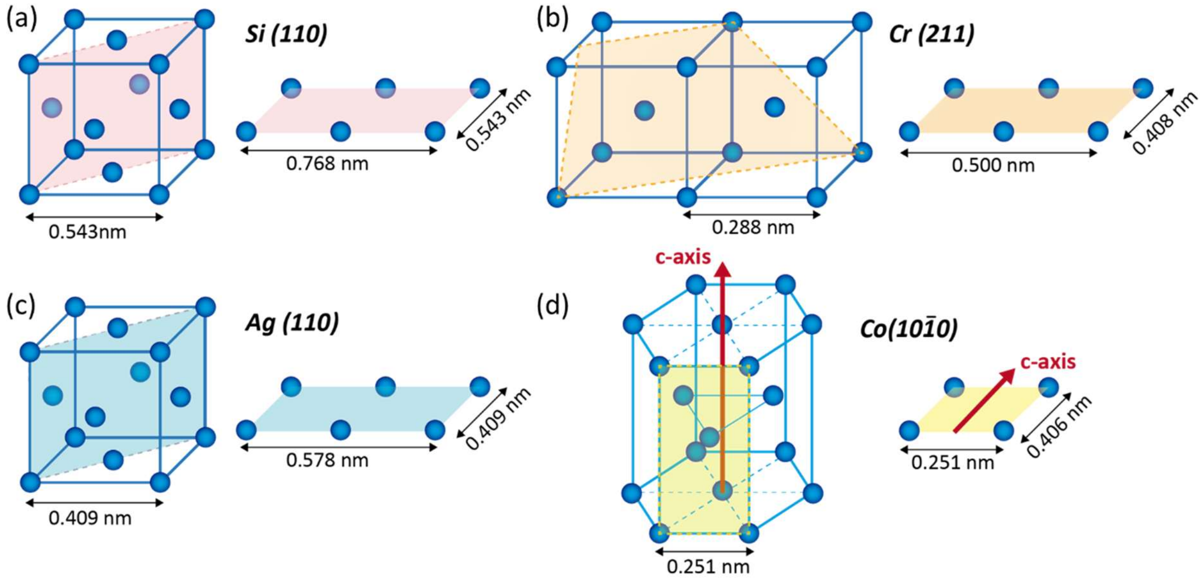

Figure 3.4 Unit cells, crystal orientations and planes corresponding to (a) the Si substrate, (b-c) the intermediate materials and (d) the Co film of interest. The crystal planes induced during the growth process with respect to the corresponding unit cells are marked. The lattice dimensions indicated refer to bulk parameters. Figure adapted from [8].

It is extremely important to have clean and smooth surfaces starting from the very substrate. Thus, before the growth, the substrates are cleaned with agents such as acetone and isopropyl alcohol (isopropanol). Then, the surface oxide of the wafers is removed by chemical etching via hydrofluoric acid (HF). In addition, it is also relevant working in clean chambers where ultra-high vacuum conditions are available prior to deposition. In this way, undesired coatings or presence of contaminants that would impact or deteriorate the epitaxy or create instabilities during growth are avoided.

3.2 Structural characterization

To assess the structural properties of the fabricated thin films and multilayers, x-ray-based characterization techniques are used. These x-ray techniques are widely used in material science because the photon wavelength λ is of the same order of magnitude as the interatomic distances in matter [9,10], they are nondestructive techniques and can be performed under standard conditions. In these techniques, the x-ray intensity reflected at the surface of a sample is measured while varying the grazing incidence angle ω and the reflected angle θ, and/or the azimuthal angle φ. All the x-ray characterization techniques employed in this work are performed under symmetric diffraction condition $\omega = \theta$. The intensity patterns obtained will give different structural information of the sample measured.

In the x-ray tools, the x-ray generation is achieved by accelerated electrons that impact inelastically an anode, causing the emission of a certain x-ray spectrum. Such spectrum is composed of a continuous background superimposed to several characteristic lines of the anode material, that correspond to the electronic transitions from higher energy levels to the lowest energy vacancies [9]. A usual anode material is copper, whose most relevant characteristic lines are the Cu-K_α (λ = 1.54 Å) and Cu-K_β (λ = 1.40 Å). Given the narrow bandwidth and high intensity of the Cu-K_α line, this particular wavelength is the most commonly employed in x-ray analysis.

In this work, two different x-ray tools have been utilized: a X'Pert PRO PANalytical (Fig. 3.5(a)) and a PANalytical EMPIREAN (Fig. 3.5(b)). Both tools have a similar set of optics, composed of an incident beam arm with an x-ray tube and incident optics, and a detection arm with the corresponding diffracted optics and detector, both of which can move independently. Furthermore, the sample holder allows for polar and azimuthal rotations of the sample. The components can be observed in the picture included in Fig. 3.5(c).

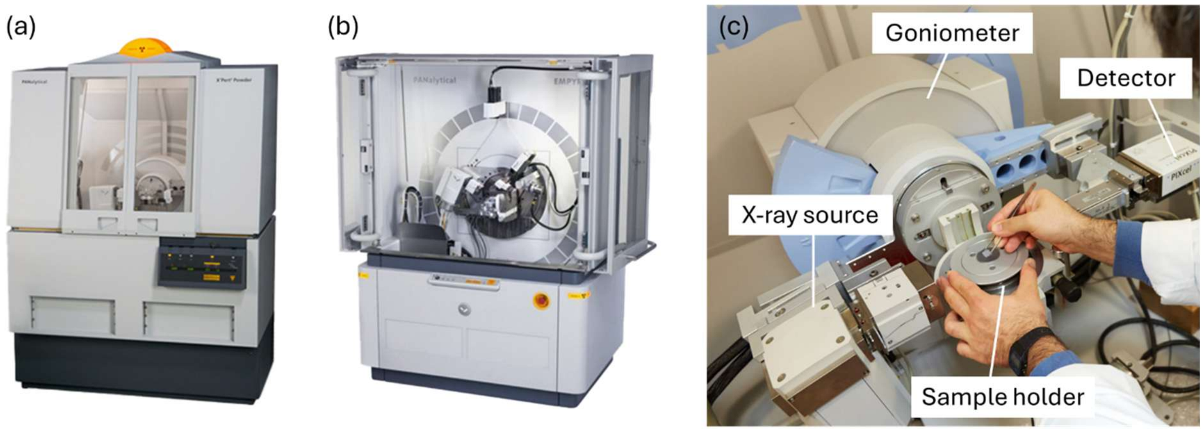

Figure 3.5 (a) X'Pert PRO PANalytical and (b) PANalytical EMPIREAN X-ray tools. (c) Picture of the components of the x-ray tool. Figures from [10,11].

3.2.1 X-ray diffraction

X-ray diffraction (XRD) is a structural characterization technique used to study the crystal planes of multilayers. Optical interferences of the reflected x-rays can lead to diffraction patterns that, at the same time, can provide relevant information about the crystal structure of the materials [9,12,13].

In a periodic atomic lattice, assuming elastic scattering, constructive interference occurs when the total momentum transfer $\vec{Q_i} = \vec{k_f} - \vec{k_i}$ is a vector of the reciprocal lattice and $|\vec{Q_i}| = 2\pi/d_i$. Here, d_i is the distance between atomic planes, and $\vec{k_f}$ and $\vec{k_i}$ are the diffracted and incident wave-vectors. Such condition, known as the Laue condition, leads to Bragg's law, which states that constructive interference will occur if

$$n\lambda = 2d\, sin\theta \tag{3.2}$$

where n is an integer denoting the diffraction order. In this regard, by measuring the intensity of the diffracted x-rays while varying the reflected angle with respect to the sample plane θ, a diffraction pattern with the constructive interferences is obtained.

The XRD measurements in this work were conducted with the two previously mentioned tools, both using a high-resolution diffractometer equipped with a Cu-K_α x-ray source ($\lambda = 1.5406$ Å), a monochromator, and a 2D detector. XRD measurements were performed for epitaxial samples, in order to verify and confirm the stacking sequence and crystallographic relation between the layers.

Two geometry types of XRD measurements are utilized in this work: the gonio $\theta - 2\theta$ scans and the azimuthal φ-scans.

(i) In the gonio $\theta - 2\theta$ geometry, the reflected intensity is measured while both the x-ray source and the detector are rotated symmetrically about the sample surface. The pattern obtained reveals the identity of the crystallographic planes present in the sample parallel to the film surface. A schematic of a XRD experiment for $\theta - 2\theta$ scans and of the periodic atomic planes parallel to the sample surface are included in Fig. 3.6(a) and Fig. 3.6(b). An exemplary diffraction pattern of an epitaxially grown sample consisting of Si (220)/ Ag (220)/ Cr (211)/ $Co_{0.95}Pt_{0.05}$ $(10\bar{1}0)$ is represented in Fig. 3.6(c). The precise matching of peak positions with the crystallographic planes confirms the high degree of crystalline alignment that one would expect for an epitaxial sample to exhibit [5,7,14]. Examples of XRD measurements are included in Chapters 4, 5 and 6.

(ii) The azimuthal φ-scans [5,15] provide information about crystal planes that are not parallel to the film surface. One has to tilt the sample an angle χ with respect to the x-rays plane of incidence, to an angle corresponding to a particular interplanar angle. Then, move ω and θ to a certain Bragg reflection and scan the reflected intensity while rotating the sample, $\varphi = 0 - 360$ deg. The process is illustrated in Fig. 3.7(a) and the corresponding wave interference in Fig. 3.7(b). The number of maxima observed during a φ scan will depend on the Bragg reflection, out-of-plane orientation, and number of preferential in-plane orientations of the grains in the film. One example of four scans for the different layers of the same sample as in Fig.

3.6(c) is included in Fig. 3.7(c). These measurements prove the epitaxial growth of the multilayer structure.

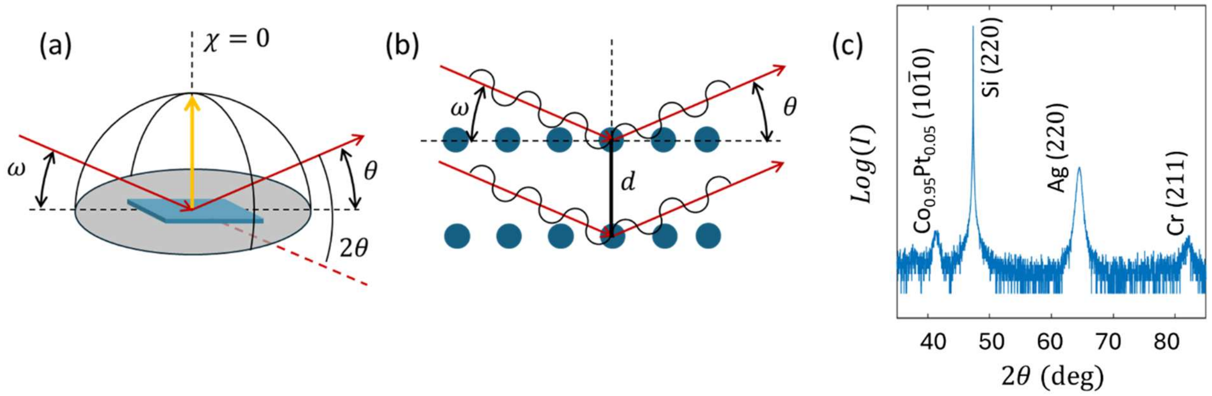

Figure 3.6 (a) Schematic of x-ray diffraction with a $\theta - 2\theta$ *geometry with the different angles of the experiment indicated, (b) schematic illustration of wave interference in crystallographic structures, (c) example of a XRD measurement of a Si* (220)*/ Ag* (220)*/ Cr* (211)*/* $Co_{0.95}Pt_{0.05}$ $(10\bar{1}0)$ *sample.*

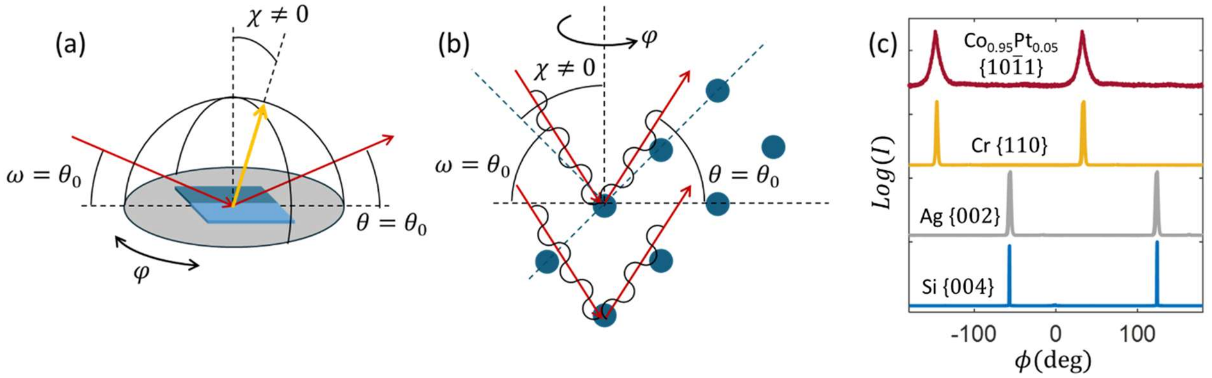

Figure 3.7 (a) Schematic of the azimuthal scan geometry, (b) schematic illustration of wave interference in crystal planes that are not parallel to the sample surface, (c) example of a φ *scan measurement of the same sample as in Fig. 3.6(c) with the crystallographic planes being Si* $\{004\}$*, Ag* $\{002\}$*, Cr* $\{110\}$ *and* $Co_{0.95}Pt_{0.05}$ $\{10\bar{1}1\}$*.*

3.2.2 X-ray reflectivity

X-ray reflectivity (XRR) is a powerful technique for determining the thickness, density, and interface roughness of thin films and multilayer structures (crystalline and amorphous films) [16]. Unlike XRD, which probes crystallographic order, XRR is sensitive to variations in electron densities in the different layers, which is equivalent to different refractive index in the different layers along the depth of the film.

The XRR technique consists of measuring the intensity of a reflected x-ray beam upon varying the angle of reflection θ, in a similar way as for XRD gonio scans but for smaller θ angles. X-rays will be refracted and reflected at the interfaces, where the refractive index changes. At the frequency of x-rays, the refractive index of most materials is slightly smaller than 1, and thus, total external reflection can occur for sufficiently low incident angles, as illustrated in Fig. 3.8(a), up to a critical value of the angle of incidence θ_c (Fig. 3.8(b)). This critical angle θ_c depends on the refractive index of the material under study and is independent of its thickness. For larger incidence angles, x-rays penetrate the material and are refracted and reflected from internal interfaces within the film or multilayer stack, as illustrated in Fig. 3.8(c). The optical path difference leads to an interference pattern, whose constructive and destructive interferences can be calculated as $2d\ sin\theta$, being now d a single layer thickness.

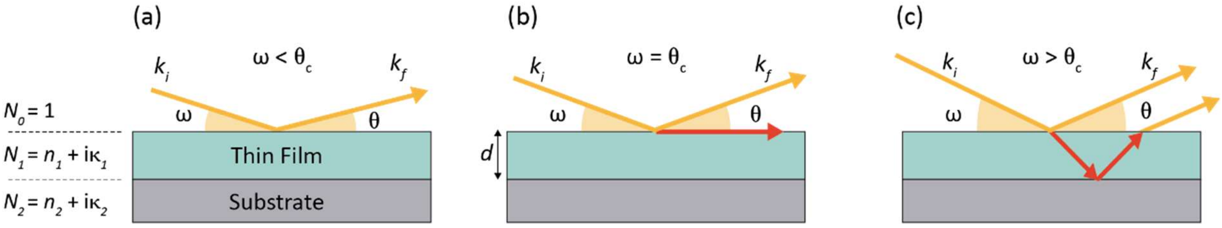

Figure 3.8 Schematics of XRR in a thin film of thickness d*. The x-ray trajectory is represented by the arrows, and the incident and reflected wavevectors* k_i *and* k_f *are indicated. Each subfigure shows the reflection of the x-rays for incident beam angle* ω *being smaller (a), equal (b) or larger (c) than the critical angle* θ_c*.*

Therefore, XRR measurements involve scanning the incident angle ω and the reflected angle θ symmetrically (i.e., $\omega = \theta$) and measuring the intensity of the specularly reflected x-rays as a function of the incident angle. The multiple reflections at interfaces interfere, resulting in an oscillatory intensity pattern profile known as Kiessig fringes. The position and periodicity of the Kiessig fringes are directly related to the layer thickness, and the contrast and decay of the fringe amplitude are affected by electron density differences and interface roughness, respectively.

To extract quantitative parameters from XRR data, the reflected-intensity curve is fitted to a theoretical model, and the thicknesses and interface roughness can be determined [17]. Some examples of XRR data and the corresponding fittings are included in Fig. 3.9 for a series of Co layers deposited on oxidized Si substrates. For different film thicknesses of the Co layer, the periodicity of the fringes varies such that larger thicknesses lead to smaller periodicities due to the distinct optical path differences.

In the context of this study, XRR was employed for calibrating deposition rates (see Section 2.1) and evaluating total and individual layer thicknesses in multilayer stacks (see Chapter 6).

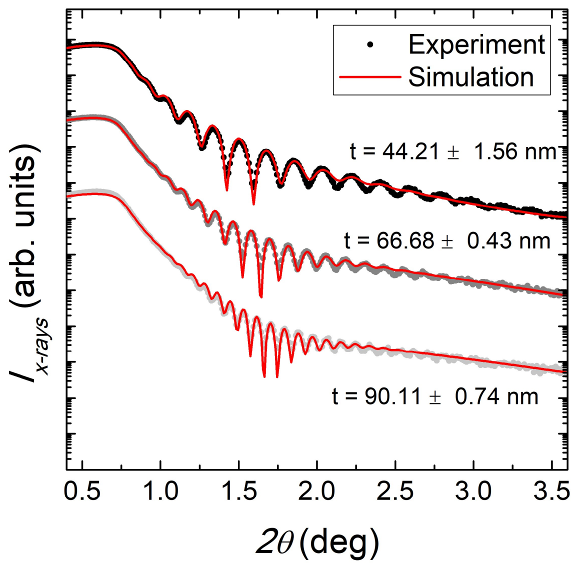

Figure 3.9 XRR intensity patterns of several Co thin films deposited on top of naturally oxidized Si wafers, with the corresponding thicknesses indicated. The red lines represent least-squares fittings that allow to extract the actual thicknesses of the films.

3.3 Conventional magnetic characterization

In this work two magnetometry techniques have been employed to quantify the macroscopic magnetization behavior as a function of different variables, such as external field, and sample orientation. The first technique is VSM, which measures the total moment of the sample. The second technique is GME, which enables vector-resolved magnetometry. As GME constitutes a key part of this thesis, the Section 3.4 will be fully dedicated to it, and here I will focus only on the conventional magnetic characterization technique of VSM.

3.3.1 Vibrating sample magnetometry

Magnetometry techniques aim to determine how a material responds to an applied magnetic field, and to extract its intrinsic magnetic properties. A commonly used magnetometry technique to characterize magnetic materials is VSM. It is based on Faraday's law of induction, which states that a changing magnetic field will produce an electric field. By measuring this electric field one can obtain information about the changing magnetic field [18,19].

In a VSM setup, the sample is placed between the coils of an electromagnet, which applies a uniform magnetic field. The sample is mounted on a non-magnetic rod and it is mechanically vibrated at a defined and constant frequency. This motion of the magnetized sample induces a time-varying magnetic flux through a set of suitably placed pick-up coils, which due to the Faraday-Lenz law of induction generates an electric signal that is directly proportional to the magnetic moment of the sample. By measuring the current generated at the coils, and thanks to a calibration procedure, the projection of the magnetic moment along the applied field axis can be detected.

In this work, the VSM system used is a MicroMag Model 3900 VSM system (Princeton Measurements Corporation), shown in Fig. 3.10(a), which provides excellent sensitivity (better than 10^{-6} emu). Schematics of the VSM system are presented in Fig. 3.10(b) to illustrate the experimental procedure and better identify the main elements involved in the measurement process, which include:

- An electromagnet to generate a well-controlled and homogeneous external magnetic field. The distance between the electromagnet poles is adjustable, allowing for the application of magnetic fields up to 2 T.
- Pick-up coils to measure the induced voltage.
- A Kel-F (Plychlorotrifluoroethylene) sample holder, a carbon rod and a vibration mechanism that oscillates the sample at a constant and known frequency. In this work, the samples are fixed to the sample holder with silicone grease, and sample holders for in-plane and out-of-plane measurements are available, although only in-plane measurements are conducted here.

- A lock-in amplifier and data acquisition system to extract the signal at the vibration frequency, enhancing sensitivity by suppressing noise contributions at other frequencies.
- A three-axis motorized translation stage, which enables precise positioning of samples at the center of the detection coils, ensuring optimal and calibrated signal detection.
- An automated rotation stage that allows for the rotation of the sample about the axis perpendicular to the applied magnetic field, with a precision better than 1º. This feature enables angular-dependent magnetometry, which has been employed in this thesis to extract angular variations of magnetic parameters such as the anisotropy constants and saturation magnetization values of Co and Co-alloy thin films.
- Additionally, the system allows for temperature dependent magnetic measurements, although this feature was not employed in the present work.

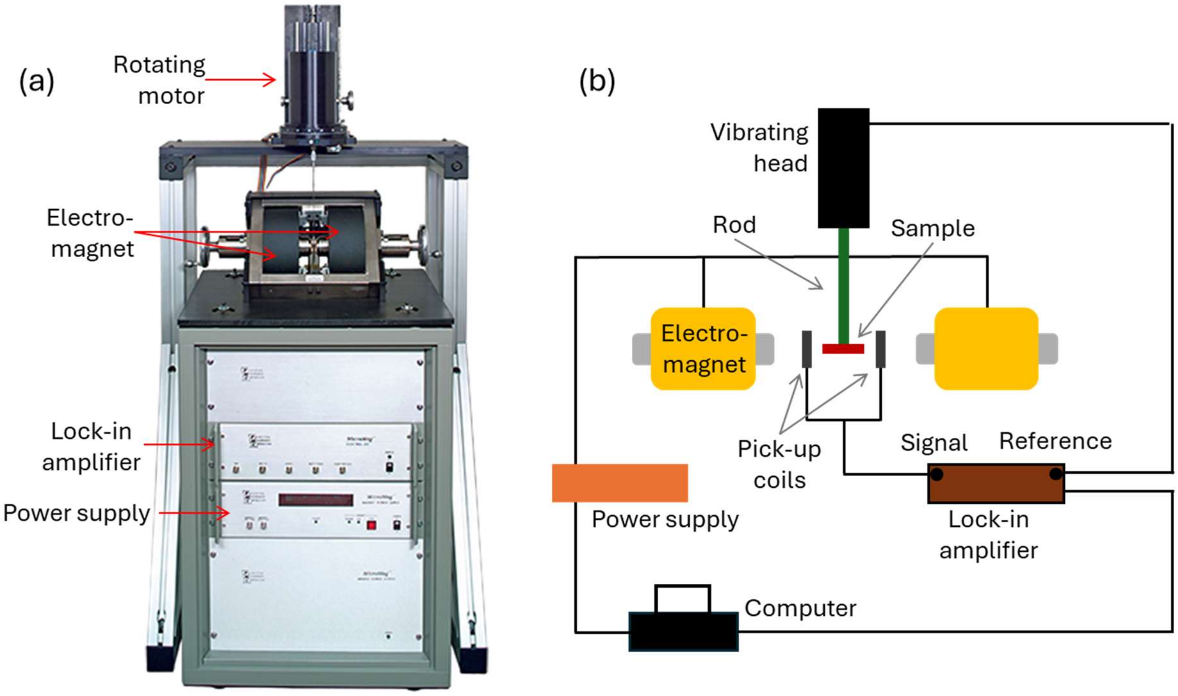

Figure 3.10 (a) Picture and (b) scheme of the core components of a VSM system, including an electromagnet to generate the external magnetic field, detection coils to measure the induced voltage, and a vibration mechanism that oscillates the sample at a constant frequency.

3.4 Generalized magneto-optical ellipsometry

The main method that I use throughout this thesis is GME. It allows one to obtain all information accessible by a reflection measurement of a sample under investigation, by quantitatively measuring the full complex reflection matrix [1] [20–22]. Correspondingly, it allows full vector magnetometry using a single reflection experiment and measurement sequence [21,23]. In this part I will describe the set-up, the data acquisition scheme, the mathematical description and the specific implementations of the technique that I utilized.

3.4.1 Main experimental setup

The experimental setup is schematically represented in Fig. 3.11(a) and a picture of the actual setup is included in Fig. 3.11(b). A linearly polarized and intensity stabilized low-noise solid-state laser emits light at a wavelength of 635 nm, which passes through a first rotatable linear polarizer P_1 and reaches the sample under investigation to be measured. Upon reflection from the sample, the light goes through a second rotatable linear polarizer P_2, after which the transmitted light intensity is measured by a Si photodiode detector. The sample itself is placed inside the gap of an electromagnet, which produces an external field along the x-direction as defined in Fig. 3.11(a) [19,22,23].

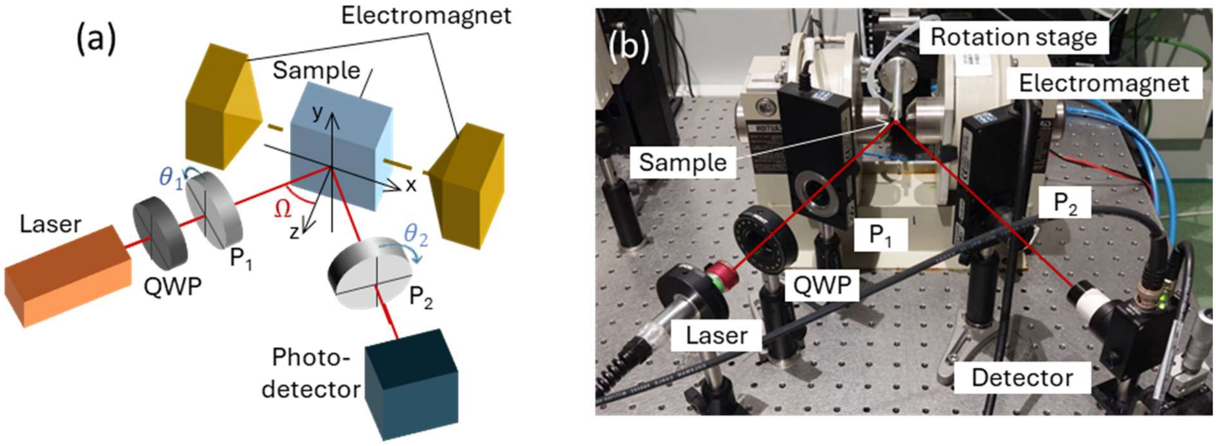

Figure 3.11 GME set up (a) schematic and (b) picture, with the elements indicated.

The first linear polarizer P_1, located in the incident beam path, defines the linear polarization axis of the incident light by means of angle θ_1, in reference to the s-polarization direction, which is perpendicular to the plane of incidence. Similarly, the linear polarization axis of the second linear polarizer P_2 is defined by angle θ_2, also in reference to the s-polarization direction. Positive values of the linear polarizer angles θ_1 and θ_2 are associated with the counterclockwise rotation sense along the propagation direction of the light, as indicated in Fig. 3.11(a) by the blue arrows. The two linear polarizers are set onto motorized rotation stages,

---

[1] Except for its absolute size and phase.

which allows one to set the orientations of the polarizers reproducibly with high angular precision. Rotating or translating sample holders can also be included for investigating orientation or position dependent properties.Additionally, in order for the light intensity arriving at the sample to be nearly constant regardless of the angle of P_1, a quarter waveplate (QWP) is mounted right after the laser, placed so that the light that enters P_1 is circularly polarized.

The specifics of the elements of the real set up (picture included in Fig. 3.11(b)) are the following:

- An ultra-low noise diode laser module operating at $\lambda = 635$ nm with 5 mW output power (Coherent Corp.) as the light source.
- An achromatic QWP (Thorlabs, Inc.) fixed in its orientation with respect to the laser light polarization state, so the light after passing through it is circularly polarized.
- Two Glan-Taylor calcite, achromatic linear polarizers with an extinction ratio of 100000:1 (Thorlabs, Inc.).
- Two motorized rotation stages (PR50CC by Newport Corp.) where the polarizers are mounted, whose movement is adjusted by single-axis stepper motor controllers (SMC100 by Newport Corp.).
- An additional (and identical) motorized rotation stage for the sample holder; the sample is attached to the holder via a vacuum chuck.
- A low-noise low-offset Si-photodiode with tunable gain (Thorlabs, Inc.) for the light detection, in which a band-pass red filter (635 ± 2 nm) is placed in front of its window to suppress the majority of ambient light.
- An electromagnet, run by a power supply delivering up to 50 V at a maximum current of 8 A (Kepco BOP 50-8M), that can yield a maximum of 1 T at the sample position.

The measurement and data acquisition process are fully automated and controlled by a computer using the LabVIEW software (National Instruments Corp.). This includes the motion of all mechanical parts such as rotators, as well as the power generation for sweeping the applied magnetic field. This automation and control of the polarizers and sample rotation and of the applied magnetic field is especially advantageous given the large number of measurements that are typically performed in a GME measurement. It is worth pointing out that no lock-in or light modulation techniques are employed for detection in the GME technique.

3.4.2 Data acquisition scheme

GME measurements are conducted by recording the photodetector voltage, which is proportional to the reflected light intensity, for various polarizer angle pairs (θ_1,θ_2) as a function of external magnetic field H. For each (θ_1,θ_2) pair, a complete hysteresis loop is obtained, representing the magnetization behavior of a sample under different measurement conditions, resulting in different $I(H)$ loop shapes and amplitudes as illustrated in the different subfigures of Fig. 3.12.

While the magnetization switching at the coercive field always remains consistent independent from the specific (θ_1, θ_2) pair setting (since the sample itself undergoes the same magnetization reversal process), in each case, the hysteresis loop shape and amplitude vary considerably. Furthermore, the sign of the MO Kerr effect (MOKE)-induced light intensity change can invert with modified (θ_1, θ_2) polarizer configurations, a phenomenon clearly visible when comparing the subfigures of Fig. 3.12. Also, the total detected light intensity I exhibits significant variations as the (θ_1, θ_2) pair settings are modified, due to the different ellipsometric detection conditions associated with each setting. The collection of all these distinct data that represent the same magnetic behavior constitute the fundamental principle by which GME facilitates the complete determination of the full reflection matrix $\boldsymbol{R}$.

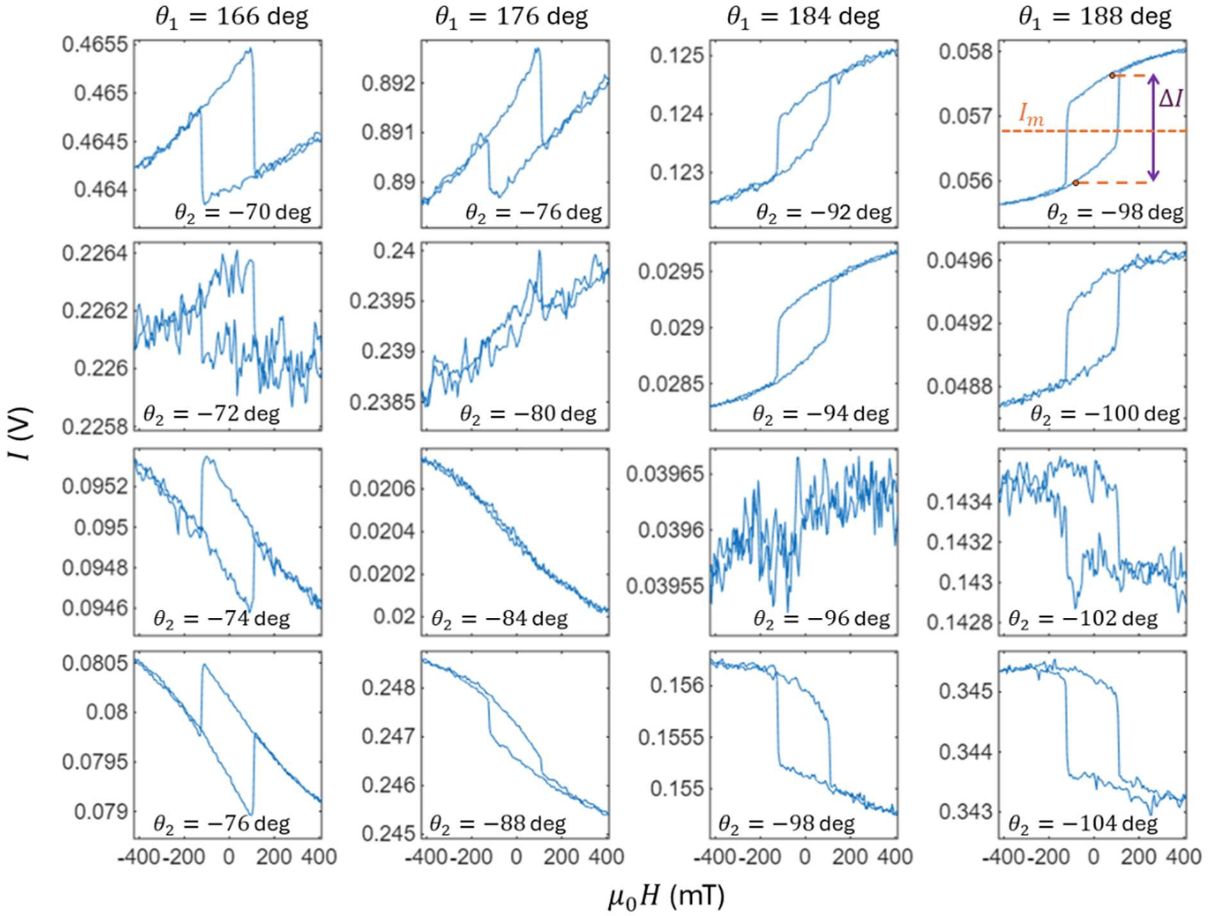

Figure 3.12 Exemplary GME-type light intensity I vs H hysteresis loops for different (θ_1, θ_2) settings. The columns correspond to the same θ_1 values, with the different subfigures in each column having different θ_2 angles. The intensity difference ΔI corresponding to a fixed H and $-H$ value pair and the mean intensity for those two points I_m are illustrated in the top right subfigure.

To quantitatively determine the reflection matrix $\boldsymbol{R}$, as will be detailed in the subsequent section, it is necessary to determine the normalized intensity change from the initially measured data sets. This involves comparing the intensity between applied field H during the decreasing field branch and field $-H$ for the increasing field branch of the hysteresis. The intensity change $\Delta I = I(H_{decreasing}) - I(-H_{increasing})$ as well as the mean intensity I_m for a specific H value is exemplary indicated in the top right subfigure of Fig. 3.12. One can express this $\Delta I/I_m$ quantity as

$$\frac{\Delta I}{I}(H) = 2\frac{I(H) - I(-H)}{I(H) + I(-H)}. \tag{3.3}$$

Such measurements are repeated for a grid of orientations of the polarizer settings (θ_1, θ_2), which is specifically chosen to obtain the best sensitivity for the small MO effects [24], creating a diagonal shaped $\Delta I/I$ map for every magnetic field value as represented in Fig. 3.13. Exemplary color-coded maps are represented in Fig. 3.13(a-d), with the horizontal axis given by θ_2 values and the vertical axis accordingly defined by θ_1. Figures 3.13(a)–(d) correspond to different magnetic field strength values H as indicated at the top of each subfigure. One can observe that the pattern changes as the magnetic field strength varies. For $\mu_0 H = 800$ mT in Fig. 3.13(a), one can see two well-defined peaks of opposite sign, symmetrically placed around the diagonal of the grid and with the positive peak having slightly bigger absolute values. For $\mu_0 H = 400$ mT in Fig. 3.13(b), the peak intensities decrease, and for $\mu_0 H = 0$ mT (Fig 3.13(c)) the intensity of the $\Delta I/I$ signal of the peaks is reduced, and the symmetry of the peaks has changed from a dominant diagonal symmetry axis to a signal pattern that is more aligned with the vertical axis. For $\mu_0 H = -800$ mT in Fig. 3.13(d), the signal increases again, hereby exhibiting very similar intensities as for the $\mu_0 H = 800$ mT case but with inverted peaks as the magnetization itself is inverted.

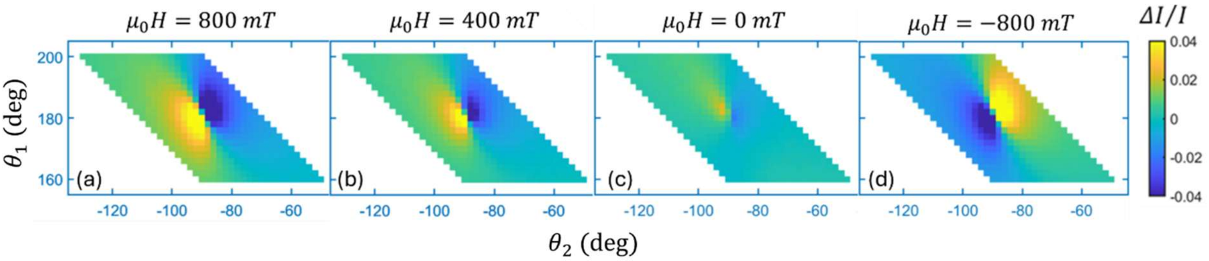

Figure 3.13 (a)–(d) Sequence of experimentally measured $\Delta I/I(\theta_1,\theta_2)$ color-coded maps obtained for four different fields, namely, $\mu_0 H$ = 800, 400, 0 and -800 mT.

3.4.3 Mathematical description

The utility of determining $\frac{\Delta I}{I}(H)$ comes from the existence of a mathematical closed-form expression, derived by using the Jones matrices of all the elements in the set-up, that describes the functional dependency of $\frac{\Delta I}{I}(\theta_1,\theta_2)$ and is used to fit the experimental data and obtain the reflection matrix components as fitting parameters [21,25].

To obtain this expression, the electric field at the detector E_D is calculated by subsequently multiplying the 2×2 operator matrices of the optical elements in the setup to the incident electric field E_I, such that

$$E_D(M) = P_2 \cdot R(M) \cdot P_1 \cdot E_I\ , \tag{3.4}$$

where $R(M)$ is the reflection matrix of the sample as defined by Eq(2.18), reproduced here, and P_1 and P_2 are the Jones matrices of the polarizers at angles θ_1 and θ_1, respectively:

$$\boldsymbol{R} = \begin{pmatrix} r_s & \alpha + \gamma \\ -\alpha + \gamma & r_p + \beta \end{pmatrix} = r_p \begin{pmatrix} \tilde{r}_s & \tilde{\alpha} + \tilde{\gamma} \\ -\tilde{\alpha} + \tilde{\gamma} & 1 + \tilde{\beta} \end{pmatrix}, \tag{3.5}$$

$$P_i = \begin{pmatrix} \cos^2 \theta_i & cos\, \theta_i \sin \theta_i \\ cos\, \theta_i \sin \theta_i & \sin^2 \theta_i \end{pmatrix}, i = 1{,}2 \tag{3.6}$$

The corresponding intensity function for an arbitrary magnetization orientation is then

$$I(M) \;\; = E_D(M)^* \cdot E_D(M) \tag{3.7}$$

and by recalling the time reversal symmetry for ferromagnetic materials $M(H) \; = -M(-H)$, we assume that the magnetically induced reflection matrix elements $\tilde{\alpha}$, $\tilde{\beta}$ and $\tilde{\gamma}$ change the sign upon inverse applied magnetic field values corresponding to a different field cycling history:

$$\tilde{\alpha}(-M) = -\tilde{\alpha}(M), \tag{3.8}$$

$$\tilde{\beta}(-M) = -\tilde{\beta}(M), \tag{3.9}$$

$$\tilde{\gamma}(-M) = -\tilde{\gamma}(M) \tag{3.10}$$

Finally, the mathematical expression for $\Delta I/I \; = 2\frac{I(M)-I(-M)}{I(M)+I(-M)}$ is obtained, resulting in

$$\frac{\Delta I}{I}(H, \theta_1, \theta_2) = 4\frac{B_1 f_1 + B_2 f_2 + B_3 f_3 + B_4 f_4 + B_5 f_5 + B_6 f_6}{f_3 + B_7 f_7 + 2B_8 f_4 + I_0}, \tag{3.11}$$

in which $f_i(\theta_1, \theta_2)$ are known trigonometric functions

$$f_{1,5} = \sin^2 \theta_1 \sin \theta_2 \cos \theta_2 \mp \sin^2 \theta_2 \sin \theta_1 \cos \theta_1, \tag{3.12}$$

$$f_{2,6} = \cos^2 \theta_2 \sin \theta_1 \cos \theta_1 \mp \cos^2 \theta_1 \sin \theta_2 \cos \theta_2, \tag{3.13}$$

$$f_3 = \sin^2 \theta_1 \sin^2 \theta_2, \tag{3.14}$$

$$f_4 = \sin \theta_1 \cos \theta_1 \sin \theta_2 \cos \theta_2, \tag{3.15}$$

$$f_7 = \cos^2 \theta_1 \cos^2 \theta_2 \tag{3.16}$$

and the $B_i(H)$ are parameters related to the components of the reflection matrix, specifically

$$B_1 = Re(\tilde{\alpha}), \tag{3.17}$$

$$B_2 = Re(\tilde{r_s}\, \tilde{\alpha}^*), \tag{3.18}$$

$$B_3 = Re(\tilde{\beta}), \tag{3.19}$$

$$B_4 = Re(\tilde{r_s}\, \tilde{\beta}^*), \tag{3.20}$$

$$B_5 = Re(\tilde{\gamma}), \tag{3.21}$$

$$B_6 = Re(\tilde{r_s}\, \tilde{\gamma}^*), \tag{3.22}$$

$$B_7 = |\tilde{r_s}|^2, \tag{3.23}$$

$$B_8 = Re(\tilde{r_s}). \tag{3.24}$$

The additional term I_0 in Eq. (3.11) is a small experimental correction term that accounts for a background intensity due to imperfections of the optical elements and/or detector offset. Moreover, using this expression as a function of the two linear polarized angles, the B_i, I_0 and the angular offsets of the polarizers $\Delta\theta_i$ are obtained as fitting parameters for all $\Delta I/I(H)$ measured maps. The least-squares fit results to Eq. (3.11) are represented in the second row of Fig. 3.14, each subfigure being the corresponding simultaneous fit result of the above measured color-coded maps. The R^2 values of the corresponding fits are shown in the top-right corner of the individual subfigures, and in all cases, their values are > 0.998, which confirms the visual impression of the fit results replicating the experimental data extremely well, which in turn ensures that the obtained fit parameters are very reliably determined.

Moreover, each subfigure in Fig. 3.14 contains two color-coded maps. The reason behind this is that these two grids, ideally placed in the vicinity of the extinction points defined by the s-p and p-s configurations of the two polarizers, are needed to achieve an unambiguous separation of longitudinal and polar MOKE signals, as will be explained in the next subsection. In this regard, the angular offsets of the polarizers $\Delta\theta_i$ just mentioned are four additional parameters (for θ_1 and θ_2 for the s-p and p-s configurations) added to account for slight deviations between the nominal polarizer angles and the real polarizer angles in the s-p and p-s frame.

An important aspect about GME is that, given that the analyzed quantity is a difference between states with inverted M, contributions to the detected light intensity from terms that are quadratic, bilinear or of higher even order in M are eliminated in this methodology. This is very relevant because, even though quadratic or bilinear effects are generally smaller than linear ones, they are not negligible in some cases and are sometimes used in measurements. Thus, if GME did not intrinsically cancel out their contribution, the precision of the measurements would be impacted, as the measured $\Delta I/I$ is compared to an equation that assumes only linear MOKE terms. One could have a contribution of higher order odd powers of M, but those are typically much smaller than the linear contribution of M and thus such terms are not included in the analysis.

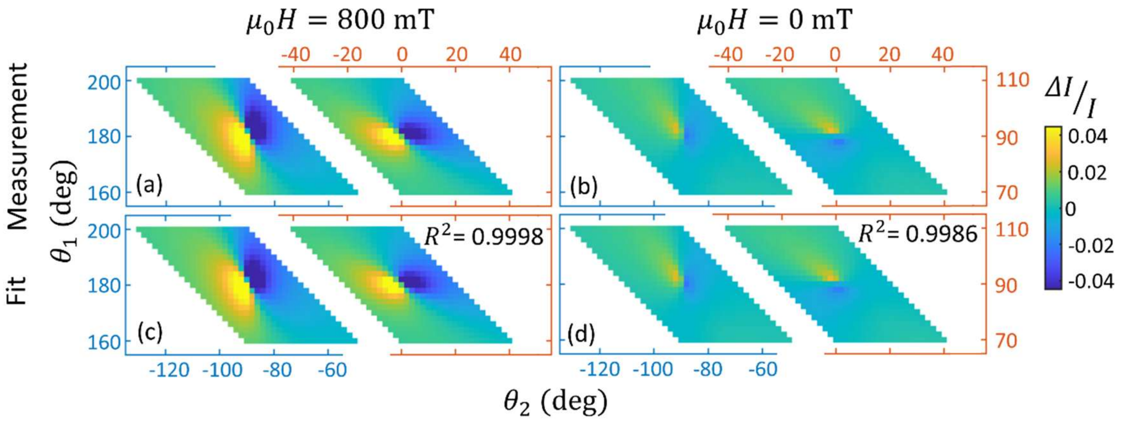

Figure 3.14 (a)–(b) Sequence of experimentally measured $\Delta I/I(\theta_1,\theta_2)$ color-coded maps obtained for two different fields, namely, $\mu_0 H$ = 800, and 0 mT, and (c)–(d) the corresponding fits to Eq. (3.11), with the R^2 value displayed in the right top corner of every subfigure. The two color-coded maps contained in each subfigure show data around the s–p (left map, blue axis) and p–s (right map, orange axis) crossing-point configurations of the polarizers. The color-scale on the right side of the figure applies to all subfigures.

3.4.4 Symmetries of GME Maps and Separation of Magnetization Components

A fundamental strength of the GME methodology is its ability to distinguish between the longitudinal, transverse, and polar MOKE components of the magnetization vector $\vec{M}$, by exploiting the distinct symmetry properties of each component's contribution to the measured $\Delta I/I$ maps.

We can see the different symmetries in Fig. 3.15, where Fig. 3.15(a) shows the total measured signal as already represented in Fig. 3.14(a), and Figs. 3.15(b)-(d) the associated extracted longitudinal, transverse, and polar signals, respectively, as indicated in the top-right corner of each subfigure. The transverse signal shows symmetric behavior with respect to the extinction points, while longitudinal and polar signals are antisymmetric at those points. To distinguish polar and longitudinal effects accurately, it is necessary to have the two maps representing the vicinity of both the s–p and p–s crossing points as the differences between those segments are distinct: in Fig. 3.15(b), the longitudinal signal has the positive peak on the upper area of the (θ_1,θ_2) grid and the negative peak on the lower area, while in Fig. 3.15(d), for the polar, the positive and negative peaks are distributed in a left-right manner [22]. Theoretical data that shows very clearly the different symmetries in larger angular ranges are included in Fig. 3.15(e-g).

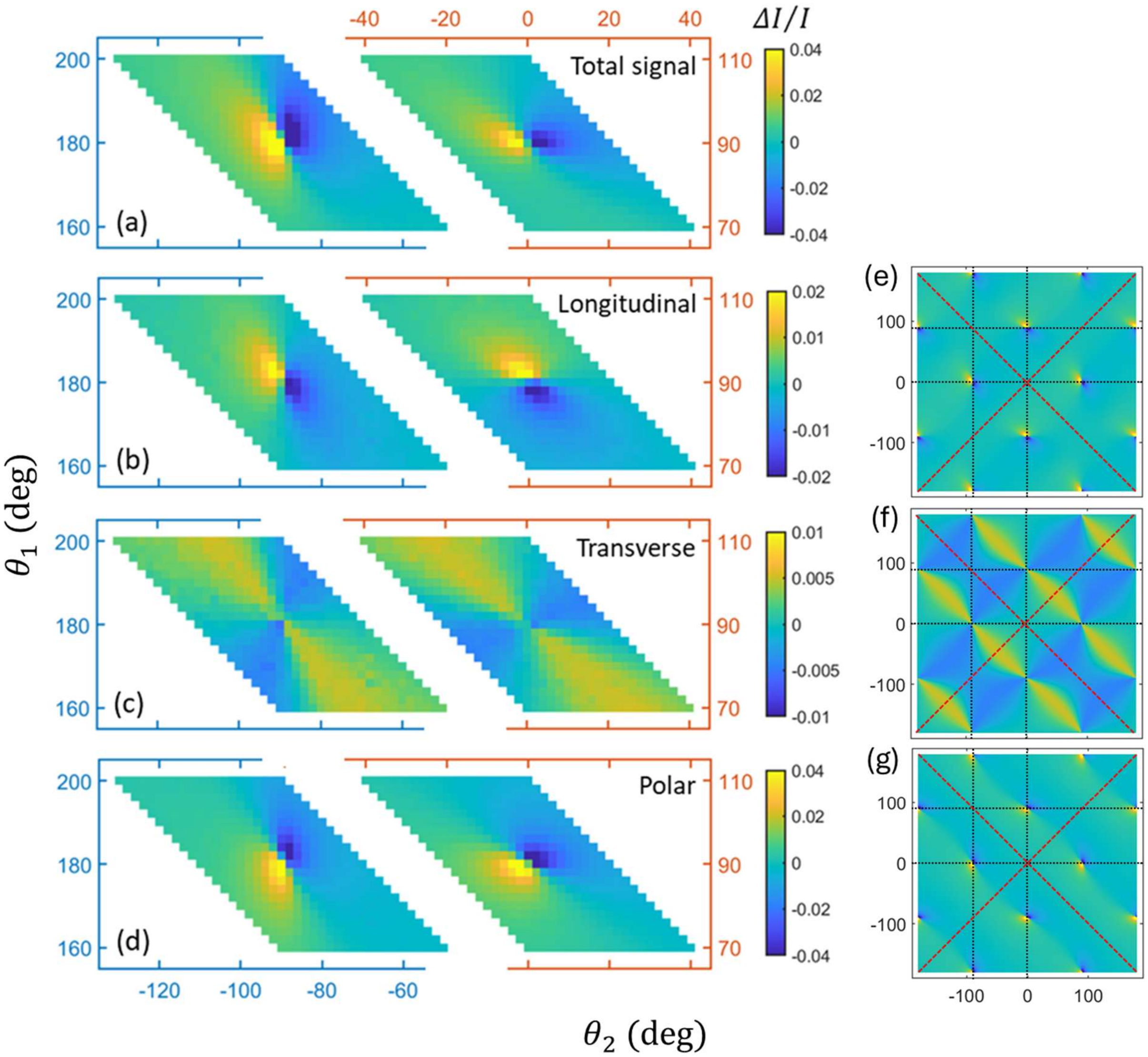

Figure 3.15 Experimental $\Delta I/I$ color-coded maps, displaying the (a) total signal as well as the correspondingly extracted (b) longitudinal, (c) transverse, and (d) polar signals, as indicated in the top right corner of each subfigure. The color code for each subfigure is shown on its right-hand side and is adapted to the size of each signal component. (e-g) theoretical data that shows very clearly the different symmetries in larger angular ranges.

3.4.5 Conventional MOKE measurements

While GME offers comprehensive vector-resolved magnetometry, conventional MOKE magnetometry remains a widely used and versatile tool. It can be useful for rapid screening of coercive fields and saturation behavior. It can also be extremely precise, because one can select the specific setting where the $\Delta I/I$ signal to noise ratio is especially large and thus, it can deliver very high quality data for hysteresis loop measurements, in which a full $\boldsymbol{R}$-analysis is not needed.

3.4.6 Implementations

The versatility of GME is improved through the following specific implementations:

- Focusing optics have been implemented when spatial resolution is needed, enabling small magnetic features and localized phenomena to be studied. The lenses are included right after the light source and right before the detector, as represented in Fig. 3.16, in order to reduce any possible modification of the polarization state of light between P_1 and the sample, and the sample and P_2.

- The light source can be modified to perform measurements at different wavelengths, allowing for multiple and different datasets that provide more detailed information about the sample studied. These wavelength dependent measurements have been done with a Fianium (now NKT photonics, Hamamatsu Comp.) tunable wavelength laser in combination with a computer-controlled acousto-optically tunable filter (AOTF). An optical fiber was utilized to direct the light exiting the AOTF onto the sample. A monochromatic light beam in the wavelength range between 450 and 850 nm can be generated and selected with this implemented GME set-up. This modification is also included in Fig. 3.16.

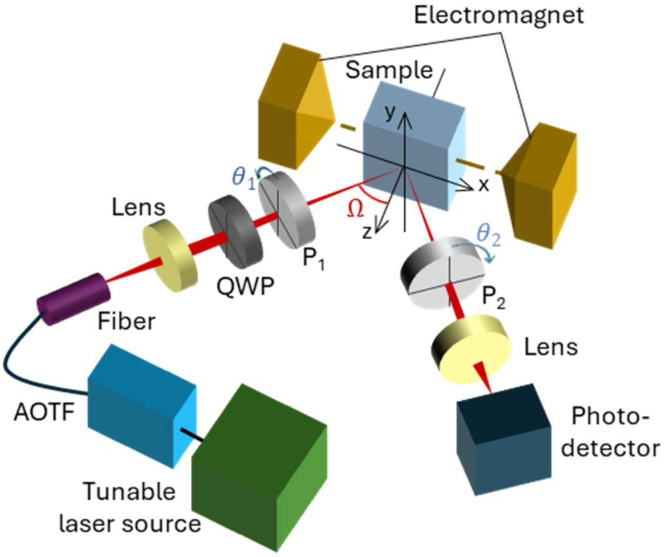

Figure 3.16. Schematic of the implemented GME set-up, with focusing optics and tunable wavelength laser.

Chapter references

[1] K. Wasa and S. Haykawa, *Handbook of Sputter Deposition Technology: Principles, Technology and Applications* (Noyes Publication, New Jersey, 1992).

[2] D. L. Smith, *Thin-Film Deposition: Principles and Practice* (McGraw-Hill Inc., New York, 1995).

[3] K. Seshan, *Handbook of Thin-Film Deposition Processes and Techniques* (Noyes Publications/William Andrew Publishing, Norwich, New York, 2002).

[4] J. A. Thornton, Magnetron sputtering: basic physics and application to cylindrical magnetrons, J. Vac. Sci. Technol **15**, 2 (1978).

[5] O. Idigoras, U. Palomares, A. K. Suszka, L. Fallarino, and A. Berger, Magnetic properties of room temperature grown epitaxial Co 1-xRux-alloy films, Appl. Phys. Lett. **103**, 102410 (2013).

[6] J. A. Arregi, J. B. González-Díaz, O. Idigoras, and A. Berger, Strain-induced magneto-optical anisotropy in epitaxial hcp Co films, Phys. Rev. B **92**, (2015).

[7] L. Fallarino, B. J. Kirby, M. Pancaldi, P. Riego, A. L. Balk, C. W. Miller, P. Vavassori, and A. Berger, Magnetic properties of epitaxial CoCr films with depth-dependent exchange-coupling profiles, Phys. Rev. B **95**, 134445 (2017).

[8] L. Fallarino, *Fabrication and Characterization of Magnetic Thin Films and Multilayer*s, (Ph.D. Thesis, University of the Basque Country, 2017).

[9] B. D. Cullity and S. R. Stock, *Elements of X-Ray Diffraction* (Prentice Hall, New Jersey, 2001).

[10] Webpage from the Massachusetts Institute of Technology, retrieved in 2025, https://nanousers.mit.edu/characterizenano/focus-facilities/xray-diffraction

[11] Webpage from CIC nanoGUNE, retrieved in 2025, https://www.nanogune.eu/en/nanogune-at-a-glance/facilities-equipment/equipment/x-ray-reflectivitydiffractometry-xpert-pro-panalytical

[12] E. Zolotoyabko, *Basic Concepts of X-Ray Diffraction* (Wiley-VCH, Weinheim, Germany, 2004).

[13] I. Robinson, *Elements of Modern X-Ray PhysicsElements of Modern X-Ray Physics , Jens Als-Nielsen and Des McMorrow Wiley, New York, 2001. $99.95, $29.95 Paper (318 Pp.). ISBN 0-471-49857-2, ISBN 0-471-49858-0 Paper* , Vol. 55 (2002).

[14] O. Idigoras, A. K. Suszka, P. Vavassori, B. Obry, B. Hillebrands, P. Landeros, and A. Berger, Magnetization reversal of in-plane uniaxial Co films and its dependence on epitaxial alignment, J. Appl. Phys. **115**, (2014).

[15] W. Yand, D. N. Lamberth, and D. E. Laughlin, Unicrystal Co – alloy media on Si (110), J. Appl. Phys. **85**, 110 (1999).

[16] M. Birkholz, *Thin Film Analysis by X-ray Scattering* (Wiley-VCH, Weinheim, Germany,2006).

[17] E. Chason and T. M. Mayer, Thin film and surface characterization by specular X-ray reflectivity, Crit. Rev. Solid State Mater. Sci. **22**, 1 (1997).

[18] S. Foner, Versatile and sensitive vibrating-sample magnetometer, Rev. Sci. Instrum **30**, 548 (1959).

[19] F. Fiorillo, Measurements of magnetic materials, Metrologia **47**, S114 (2010).

[20] A. Berger and M. R. Pufall, Generalized magneto-optical ellipsometry, Appl. Phys. Lett. **71**, 965 (1997).

[21] A. Berger and M. R. Pufall, Quantitative vector magnetometry using generalized magneto-optical ellipsometry, J. Appl. Phys. **85**, 4583 (1999).

[22] P. Riego, *Magneto-Optical characterization of magnetic thin films and interface structures* (Ph.D. Thesis, University of the Basque Country, 2019).

[23] O. Idigoras, *Magnetization reversal behavior of ferromagnetic thin films and nano-structures* (Ph.D. Thesis, University of the Basque Country, 2013).

[24] J. A. Arregi, J. B. Gonzalez-Diaz, E. Bergaretxe, O. Idigoras, T. Unsal, and A. Berger, Study of generalized magneto-optical ellipsometry measurement reliability, J. Appl. Phys. **111**, 103912 (2012).

[25] J. A. Arregi, *Magneto-Optical Ellipsometry and Magnetometry of Thin Films and Multilayers* (Ph.D. Thesis, University of the Basque Country, 2020).

Chapter 4

Reflection matrix verification

Before addressing the main goal of separating the magnetic contributions of all the involved ultrathin magnetic layers in multilayer structures via the generalized magneto-optical (MO) ellipsometry (GME) technique and achieve layer resolved vector magnetometry, it is crucial to first experimentally validate the reflection matrix $\boldsymbol{R}$ model described by Eq. (2.18). Moreover, the accurate and precise verification of Eq. (2.18) for single magnetic films is crucially necessary to facilitate the utilization of experimental deviations from the reflection matrix description $\boldsymbol{R}$ in more complex magnetic sample structures for the purpose of developing and advancing MO Kerr effect (MOKE) characterization techniques.

This chapter presents the experimental verification of the reflection matrix, starting with an introduction and motivation in Section 3.1. The selected sample design for my experiments and the subsequent sample fabrication are detailed in Section 3.2. Next, Section 3.3 discusses the experimental results, upon which conclusions are drawn in Section 3.4.

4.1 Introduction and motivation

The GME methodology and subsequent interpretation of the results rely on the expression of the reflection matrix $\boldsymbol{R}$ given in Eq. (2.18) [1,2]. Any small experimental deviation could lead to misinterpretations if it is not quantitatively verified beforehand. For clarity, I restate Eq. (2.18) here, as it will be referenced throughout this chapter:

$$\boldsymbol{R} = r_p \begin{pmatrix} \tilde{r}_s & \tilde{\alpha} + \tilde{\gamma} \\ -\tilde{\alpha} + \tilde{\gamma} & 1 + \tilde{\beta} \end{pmatrix} = r_p \begin{pmatrix} \tilde{r}_s & \tilde{\alpha}_0 \cdot m_x + \tilde{\gamma}_0 \cdot m_z \\ -\tilde{\alpha}_0 \cdot m_x + \tilde{\gamma}_0 \cdot m_z & 1 + \tilde{\beta}_0 \cdot m_y \end{pmatrix}, \tag{4.1}$$

The reflection matrix expression as it is in Eq. (4.1) is the end result of rigorous, although approximate, theoretical derivations for numerous sample geometries, and has traditionally been considered highly accurate [3–7]. For the longest time, no deviations from it have been reported. Nevertheless, recent reports of linear MOKE effects that are partially independent from the magnetization of the sample highlight the necessity of a detailed verification [8–10]. Additionally, we observed deviations from the $\boldsymbol{R}$ expression of Eq. (4.1), which are associated with depth modulated magnetic states [11].

Therefore, this chapter does not simply fill an overlooked experimental gap, but it also opens broad possibilities because a verification that $\boldsymbol{R}$ indeed describes MO effects of a film in a quantitatively accurate manner enables the experimental utilization of deviations from it to extract additional and relevant sample information. In other words, to be able to utilize deviations from Eq. (4.1) to identify physical scenarios that are not consistent with the underlying assumptions of the derivation of Eq. (4.1), I have to first prove that Eq. (4.1) is quantitatively correct for systems that are consistent with these assumptions. For instance, we demonstrated recently that a magnetic-state-induced phase change of the transverse MOKE (T-MOKE) coefficient $\tilde{\beta}$ in a bilayer magnetic system is associated with the nonsynchronous magnetic response of the constituting magnetic layers [11]. However, this interpretation is only correct and meaningful if the conventional reflection matrix $\boldsymbol{R}$ description for a single magnetic film in Eq. (4.1) is confirmed by comprehensive and precise experiments. Moreover, no one so far was able to experimentally do this work, because only GME gives sufficient access to all the terms of the reflection matrix [2,12,13].

To properly test Eq. (4.1), a key requirement is to have precise control over the magnetization vector $\vec{m}$. Since the cartesian components of $\vec{m}$ define individual elements of $\boldsymbol{R}$ according to Eq (4.1), one can test its validity if $\vec{m}$ can be oriented over a wide angular range yet maintain a constant magnitude. A uniform, macrospin-like sample accomplishes that behavior: the normalized magnetization vector $\vec{m} = \vec{M}/M_s$, with M_s being the saturation magnetization, maintains a constant magnitude $|\vec{m}| = 1$ under magnetization rotation, and the cartesian components are correlated by the angles ϑ_m and φ_m, which are the polar coordinates of the magnetization vector (as defined in Fig 4.1(a)),

$$m_x = sin(\vartheta_m) \cdot cos(\varphi_m), \qquad m_y = sin(\vartheta_m) \cdot sin(\varphi_m), \qquad m_z = cos(\vartheta_m) \tag{4.2}$$

These relationship between m_x, m_y and m_z lead directly to correlations among the MOKE parameters:

$$m_x^2 + m_y^2 + m_z^2 = 1, \tag{4.3}$$

$$\left(\frac{\tilde{\alpha}}{\tilde{\alpha}_0}\right)^2 + \left(\frac{\tilde{\beta}}{\tilde{\beta}_0}\right)^2 + \left(\frac{\tilde{\gamma}}{\tilde{\gamma}_0}\right)^2 = 1, \tag{4.4}$$

because $\tilde{\alpha} = \tilde{\alpha}_0 \cdot m_x$, $\tilde{\beta} = \tilde{\beta}_0 \cdot m_y$ and $\tilde{\gamma} = \tilde{\gamma}_0 \cdot m_z$. Remember that $\tilde{\alpha}$, $\tilde{\beta}$ and $\tilde{\gamma}$ (as well as $\tilde{\alpha}_0$, $\tilde{\beta}_0$ and $\tilde{\gamma}_0$) are complex numbers and they can be written as $\tilde{\alpha} = |\tilde{\alpha}|e^{i\phi_{\tilde{\alpha}}}$, $\tilde{\beta} = |\tilde{\beta}|e^{i\phi_{\tilde{\beta}}}$ and $\tilde{\gamma} = |\tilde{\gamma}|e^{i\phi_{\tilde{\gamma}}}$. Given this MOKE correlation, one can derive relevant test conditions that should be satisfied if Eq. (4.1) is indeed correct:

1. An ellipsoidal relation among $|\tilde{\alpha}|$, $|\tilde{\beta}|$, and $|\tilde{\gamma}|$, that turns to an ellipse relation when the magnetization vector is confined to in-plane orientations only ($\tilde{\gamma} = 0$):

$$\left(\frac{|\tilde{\alpha}|}{|\tilde{\alpha}_0|}\right)^2 + \left(\frac{|\tilde{\beta}|}{|\tilde{\beta}_0|}\right)^2 + \left(\frac{|\tilde{\gamma}|}{|\tilde{\gamma}_0|}\right)^2 = 1, \tag{4.5a}$$

$$\text{with } \tilde{\gamma} = 0,\ \left(\frac{|\tilde{\alpha}|}{|\tilde{\alpha}_0|}\right)^2 + \left(\frac{|\tilde{\beta}|}{|\tilde{\beta}_0|}\right)^2 = 1, \tag{4.5b}$$

2. The corresponding phases of the complex MOKE parameters are expected to remain constant, independent of the magnetization orientation:

$$\phi_{\tilde{\alpha}} = \phi_{\tilde{\alpha}_0}; \phi_{\tilde{\beta}} = \phi_{\tilde{\beta}_0}\ ; \phi_{\tilde{\gamma}} = \phi_{\tilde{\gamma}_0}, \tag{4.6a}$$

$$\text{with } \tilde{\gamma} = 0,\ \phi_{\tilde{\alpha}} = \phi_{\tilde{\alpha}_0}; \phi_{\tilde{\beta}} = \phi_{\tilde{\beta}_0} \tag{4.6b}$$

Additionally, the matrix elements that are not explicitly magnetization dependent, are purely optical and thus, $Re(\tilde{r}_s)$ and $Im(\tilde{r}_s)$ should remain constant for any magnetization state if Eq. (4.1) holds true.

In this chapter, a rigorous experimental study designed to prove Eqs. (4.5) and (4.6) is presented. Those Eqs. (4.5) and (4.6) are necessary conditions for Eq. (4.1) to be correct, given that they were derived from it. As such, I show that all single film results are experimentally fully consistent with Eq. (4.1), as long as the assumptions for it are fulfilled by the samples. Single magnetic films with macro-spin like behavior and without relevant levels of (magneto) optical anisotropy fulfill those assumptions. For that, one needs to:

(i) fabricate a sample type that enables the access to a broad range of magnetization orientations in the same MO measurement geometry while keeping the absolute magnetization value constant and

(ii) utilize an experimental methodology that allows to measure the full reflection matrix for all magnetization orientations.

To achieve (i) I conceived and fabricated a specific sample design, and for our MOKE measurements, the GME technique allowed to fulfill condition (ii).

4.2 Sample design and fabrication

To design a sample suitable for testing the validity of the reflection matrix model (Eq. (4.1)), one needs a material system that is well described by a fixed-length magnetization vector that can rotate in response to an applied external magnetic field, i.e., a so-called macrospin-type sample. Such behavior is best achieved with a thin film exhibiting strong uniaxial anisotropy, with an in-plane easy axis (EA) that suppresses domain formation and associated deviations from macrospin behavior. Additionally, lateral homogeneity of magnetic properties is crucial to enable a quantitatively accurate vector rotation interpretation of both macroscopic magnetization and MO properties [14,15].

I selected a Co-Pt alloy as the material system for this study. This choice is based on its high and uniform uniaxial anisotropy [16], which allows precise field control of the magnetization vector orientation over a wide range of rotation states without multi-domain formation. Specifically, I targeted the fabrication of a $Co_{0.95}Pt_{0.05}$ layer with hexagonal close-packed (hcp) crystal structure and $(10\bar{1}0)$ surface orientation, since this orientation includes the $[0001]$ direction within the surface plane, naturally aligning the EA of magnetization in-plane.

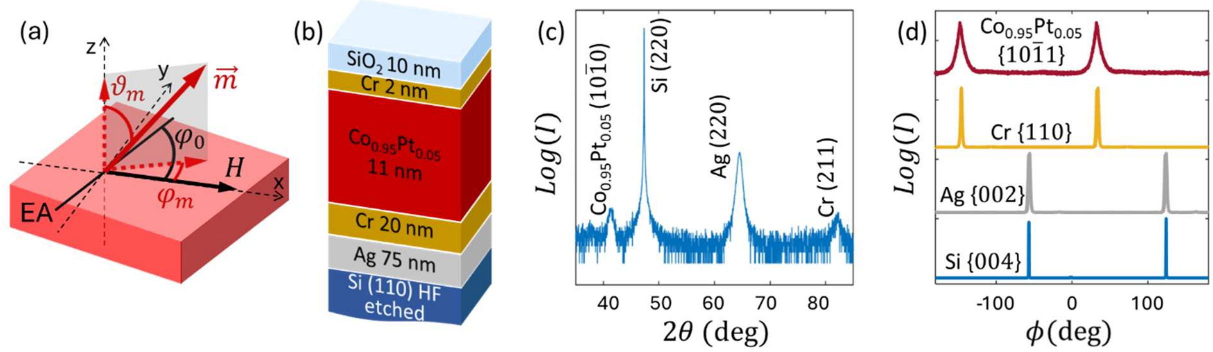

Figure 4.1 (a) Definition of the magnetization vector and EA angles; (b) schematic of the fabricated sample, indicating the thickness of the layers (not to scale), consisting of the epitaxial film sequence Ag (110)/*Cr* (211)/$Co_{0.95}Pt_{0.05}$ $(10\bar{1}0)$/*Cr* (211)*, grown onto a Si* (110) *substrate, whose oxide has been removed by hydrofluoric acid etching. The sample is covered by a 10-nm-thick SiO2 layer to avoid oxidation. (c) XRD and (d) phi-scans*

The fabrication of such a layer is done following a specific epitaxial growth sequence, represented in Fig. 4.1(b). Single-crystal Si (110) substrates are cleaned in an ultrasonic bath with acetone, isopropanol, and water. Afterwards, the native SiO_2 layer is removed by means of hydrofluoric (HF) etching in a bath for 20 minutes and immediately introduced into the vacuum chamber in the sputter deposition tool, avoiding relevant levels of oxidation of the Si surface. The layer sequence that forms the sample has been grown by sputter deposition at room temperature in a 3-mTorr pure Ar atmosphere and consists of the hydrofluoric-acid-etched Si (110) substrate, followed by 75 nm of Ag (110) and 20 nm of Cr (211) template layers that allow for the high-quality epitaxial growth of Co and Co-alloy $(10\bar{1}0)$ films, as has been demonstrated in several previous studies [14,17–21]. Here, the main specific magnetic layer is a 11-nm-thick $Co_{0.95}Pt_{0.05}$ $(10\bar{1}0)$ film, on top of which 2 nm of Cr and a 10-nm SiO_2 overcoat are deposited to have the same interface materials on both surfaces of the Co-Pt magnetic layer and to avoid surface oxidation and contaminations of the layers underneath.

The structural properties have been initially characterized by x-ray diffraction (XRD) $\theta - 2\theta$ measurements (Fig. 4.1(c)). This measurement shows the diffraction peaks exclusively associated with the crystallographic planes of the targeted layers. No extraneous peaks appear, indicating the absence of secondary phases or misoriented grains. This is consistent with previous reports on similar Co-alloy systems, where similar growth procedures yielded epitaxial structures [14,17–21]. The labeling in Fig. 4.1(c) identifies the peaks corresponding to each layer.

Azimuthal ϕ-scans were employed to verify the epitaxial growth of the entire multilayer structure. These scans target crystal planes that are not perpendicular to the film surface, thereby providing insight into the in-plane crystal structure and the relative orientation between different layers. Figure 4.1(d) displays the ϕ-scan results, where the x-ray intensities are normalized to the maximum value in each corresponding measurement. Two defined peaks are visible, which are 180 deg apart, at positions that match the stereographic projections of their nominal structure [17,19]. The Si $\{004\}$ and Ag $\{002\}$ scans indicate a parallel alignment of the Si and Ag $[001]$ directions. Likewise, the 90 deg angular shift between the Ag and the Cr peaks indicates that the Cr $[110]$ direction is parallel to the Ag $[001]$ direction, as intended. Finally, the CoPt $\{10\bar{1}0\}$ peaks appear at the same ϕ-values as those for Cr $\{110\}$, confirming the in-plane alignment of the CoPt $[0001]$ direction, parallel to the Cr $[1\bar{1}0]$ direction, as intended. Thus, this structural analysis in homogeneous CoPt thin films confirms that the whole structure grows epitaxially in the single-crystal manner intended [14,19].

Beyond structural characterization, it is essential to verify that the epitaxially grown sample exhibits the desired uniaxial magneto-crystalline anisotropy and macrospin behavior. For this purpose, in-plane magnetic hysteresis loops have been measured by means of a vibrating sample magnetometer (VSM) system. This VSM tool allows the sample to be rotated, with the rotation axis being the surface normal, so that the field is always in the surface plane, and correspondingly, the magnetization vector is always within the surface plane for a system with in-plane EA. The specific orientations of the EA and the magnetization with respect to the applied field direction are defined by angles φ_0 and φ_m, as represented in Fig. 2.2(a) and Fig. 4.1(a).

Experimentally, I have measured complete VSM hysteresis loops for different φ_0 values, such as the ones represented in Fig. 4.2(a) and compiled the corresponding data. The results shown in Fig. 4.2(a) exhibit hereby the nearly perfect textbook behavior for a uniaxial magnetic material showing a square-like hysteresis loop along the EA ($\varphi_0 = 0$ deg) and a hysteresis-free gradual reversal along the magnetic hard axis (HA; $\varphi_0 = 90$ deg).

For an unambiguous visualization and demonstration of the macrospin behavior of the sample type, hysteresis loops like those in Fig. 4.2(a) were measured for a full 360 deg range of φ_0. Figure 4.2(b) shows, as a color-coded map, the results of these measurements by displaying the normalized in-plane magnetization M/M_s along the field direction that was measured from saturation to remanence as a function of the applied magnetic field strength H and angle φ_0. For high field values, the magnetization is saturated for all angles, and $M/M_s = 1$. For low fields, M/M_s approaches zero if $\varphi_0 = 90$ or 270 deg but remains equal to ~ 1 for $\varphi_0 = 0$ or 180 deg. Moreover, for 0 and 180 deg, the M/M_s variation with H is negligible, given that M is saturated along those directions even at remanence. The observed 180 deg periodicity of the data pattern confirms that the sample shows marked uniaxial magnetic anisotropy, which I wanted to verify. Also, centered around $\varphi_0 = 90$ and 270 deg, a cone-shaped structure of reduced magnetization is visible. This cone structure is defined by an angular-dependent saturation field for any orientation that is not the EA. Specifically, along $\varphi_0 = 90$ and 270 deg, larger fields are required to induce a magnetization rotation toward the field direction, which is the behavior expected along the HA orientation of the magnetic field. Therefore, with the designed sample, the magnetization will rotate from being parallel to the external field at high field values to an EA orientation when no external field is applied.

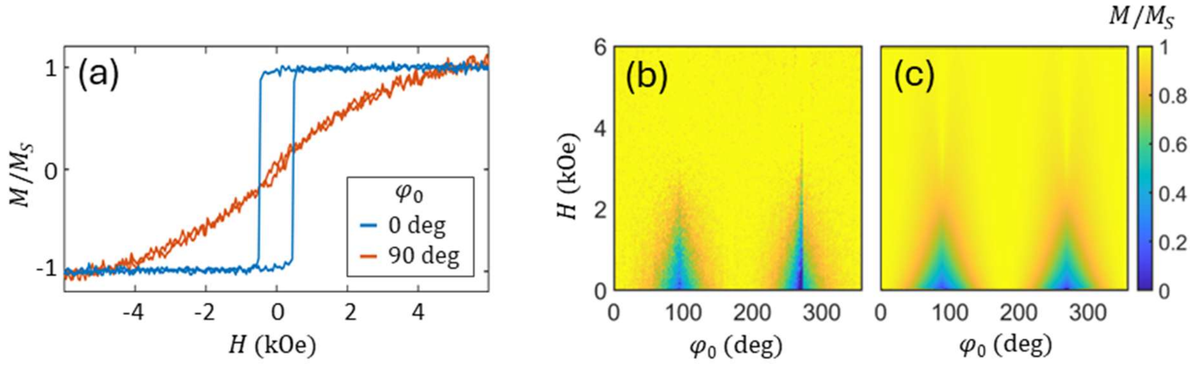

Figure 4.2 (a) Normalized magnetization M/M_S vs applied field H VSM hysteresis loops for two φ_0 values, namely, $\varphi_0 = 0$ and 90 deg, showing the EA and HA behavior of the sample. (b) Color-coded map of the normalized magnetization M/M_S along the applied field direction, measured by means of VSM, as a function of φ_0 and the field strength H, for the sample displayed in (a). (c) Corresponding least-squares fit of the data based upon the minimization of the total energy according to Eq. (4.7). The color-code legend at the right side of (c) applies to both (b) and (c).

Least-squares fits of the $M/M_s(H, \varphi_0)$ data to a macrospin model have been done to establish that a single macrospin describes the complete field dependence of the sample magnetization for any in-plane magnetic field orientation. The corresponding magnetization orientation dependent part of the free energy density expression of in-plane uniaxial magnetic films has been used (see Chapter 2) [22,23]:

$$\frac{\mathcal{F}}{\mathrm{V}} = -\mu_0 M_s H\, cos(\varphi_m) \; + \; k_1 \sin^2(\varphi_0 - \varphi_m) \; + k_2 \sin^4(\varphi_0 - \varphi_m), \tag{4.7}$$

in which the first- and second-order magneto-crystalline anisotropy energy densities are given by k_1 and k_2, respectively. These two constants k_1 and k_2 and the saturation magnetization M_s are the only fit parameters used for the map, and the values obtained for the sample are $k_1 = 0.913 \cdot 10^6$ erg/cm^3, $k_2 = 0.632 \cdot 10^6$ erg/cm^3, and $M_s = 901$ emu/cm^3, which are consistent with those obtained from other Co-alloy thin films fabricated using the same type of deposition process and underlayer structure [18]. The second-order anisotropy constant has been included here since it is well known that its value is sufficiently large in Co and Co-alloy material systems [23]. Figure 4.2(c) shows the fit result of our $M/M_s(H, \varphi_0)$ data to Eq. (4.7), which exhibits excellent agreement with the corresponding experimental data in Fig. 4.2(b). Thus, it confirms the uniaxial and macrospin behavior of my epitaxial film sample, demonstrating that, in my sample, a wide range of magnetization orientation states is easily accessible, all exhibiting a magnetization vector of constant length, i.e. exactly the type of behavior that is needed to verify Eq. (4.1), which is the purpose of this sample and work.

4.3 Results and discussion

To test the validity of the reflection matrix model, I initially focused on the simpler case first, that is the in-plane magnetization case, as it only includes two magnetization components m_x and m_y. Afterwards, the experimental verification for arbitrary magnetization orientations, with all the three cartesian magnetization components, was done.

In the in-plane magnetization case, the electromagnet of the GME set up produces an external magnetic field along the longitudinal orientation, as represented in Fig. 4.3(a) and as it was already shown in Section 3.4. The laser is positioned in our setup so that the angle of incidence is $\Omega = 26$ deg, which represents a compromise between obtaining good sensitivity and the ability to achieve a reasonably high magnetic field in the longitudinal direction.

The GME set up geometry that enables the access to a predominant out-of-plane orientation of the external magnetic field direction and therefore allow for a 3-dimensional magnetization vector, is represented in Fig. 4.3(b). The experimental setup in this case contains the same elements, and the light path and angle definitions are also identical. The key difference is the electromagnet orientation, as it has been rotated to obtain a very large out-of-plane magnetic field component for the purpose of facilitating substantial levels of out-of-plane magnetization values in combination with simultaneously varying in-plane components. Specifically, the angle of rotation of the electromagnet with respect to the sample surface is $\Psi = 87$ deg, and the angle of incidence of the laser light with respect to the surface normal is $\Omega = 70$ deg. These angles were chosen as the most convenient for obtaining the best sensitivity while also giving the ability to achieve a magnetic field contained in the optical plane-of-incidence but with a high out-of-plane component.

Before focusing on the specific cases, I will show here the general experimental procedure performed. GME measurements are done as explained in Section 3.4, obtaining color-coded maps as the ones represented in Fig. 4.4 [1]. They represent experimentally measured $\Delta I/I$ data, with the horizontal axis given by θ_2 values and the vertical axis accordingly defined by θ_1. These exemplary maps correspond to measurements on the Co-Pt alloy film sample with the GME setup displayed in the out-of-plane configuration, shown in Fig. 4.3(b). The sample is oriented with $\Psi = 87$ deg and $\varphi_0 = 45$ deg so that all magnetization components are present. Figures 4.4(a)–4(h) correspond to different magnetic field strength values H as indicated at the right top corner of each subfigure. Moreover, each subfigure contains two

---

[1] Some of these maps were already included in Chapter 3 to explain data acquisition, mathematical description and the symmetries of the maps.

color-coded maps for the two measurement grids around the s—p and p—s crossing points of the polarizers.

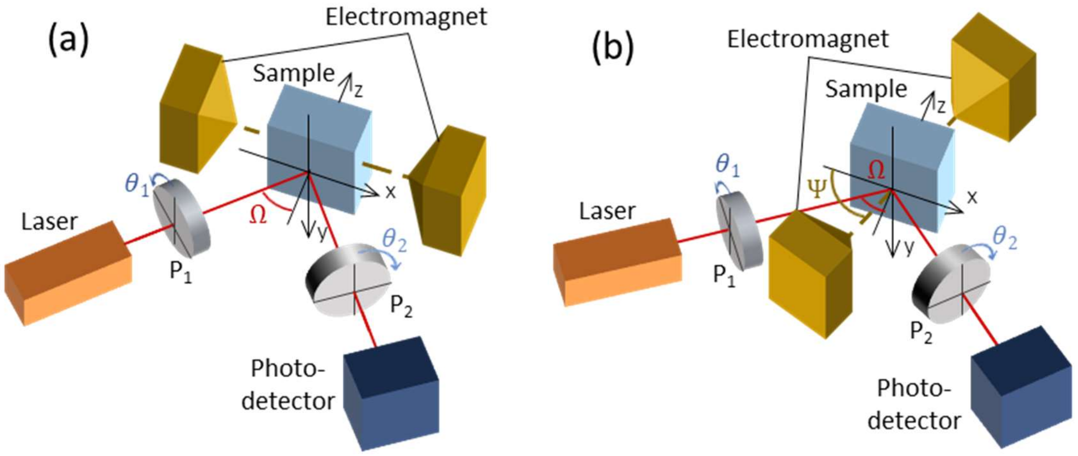

Figure 4.3 Schematic of the GME experimental setup in the (a) in-plane and (b) out-of-plane geometries, consisting of a laser light source, a first polarizer P_1, a second polarizer P_2, and a photodetector. The polarization angles θ_1 for P_1 and θ_2 for P_2 are given as the angular distance between the axis of each optical element and the s-polarization direction, utilizing the displayed sign convention (blue arrows) indicating the positive rotation sense. The sample under investigation is located inside the gap of an electromagnet that produces a magnetic field contained in the optical plane of incidence, which is also aligned with the sample (b). The path of the light beam is represented by the red line, having plane in (a), while it has an angle of $\Psi = 87$ deg with the sample plane in an angle of incidence of $\Omega = 26$ deg for the in-plane geometry and $\Omega = 70$ deg for the out-of-plane geometry.

One can observe that the pattern changes as the magnetic field strength increases, and the magnetization vector rotates accordingly. This change is not only caused by a difference in the signal intensity but also by a change of the shape of our signal pattern. For $\mu_0 H = 800$ mT in Fig. 4.4(a), one can see two well-defined peaks of opposite sign, symmetrically placed around the diagonal of the grid and with the positive peak having slightly bigger absolute values. For $\mu_0 H = 0$ mT in Fig. 4.4(d), the intensity of the $\Delta I/I$ signal of the peaks is reduced, and the symmetry of the peaks has changed from a dominant diagonal symmetry axis to a signal pattern that is more aligned with the vertical and horizontal axes for the s—p and p—s maps, respectively. For $\mu_0 H = -400$ mT in Fig. 4.4(f), the peak intensities increase again and continue increasing for $\mu_0 H = -800$ mT in Fig. 4.4(h), hereby exhibiting very similar intensities as for the $\mu_0 H = 800$ mT case but with inverted peaks as the magnetization itself is inverted.

The least-squares fit results to Eq. (3.11) are represented in the right column of Fig 4.5 in comparison with the experimentally measured $\Delta I/I$ data on its left. The R^2 values of the corresponding fits are shown in the top-right corner of the individual subfigures, and in all cases, their values are > 0.998, which confirms the visual impression of the fit results replicating the experimental data extremely well, which in turn ensures that the obtained fit parameters are very reliably determined.

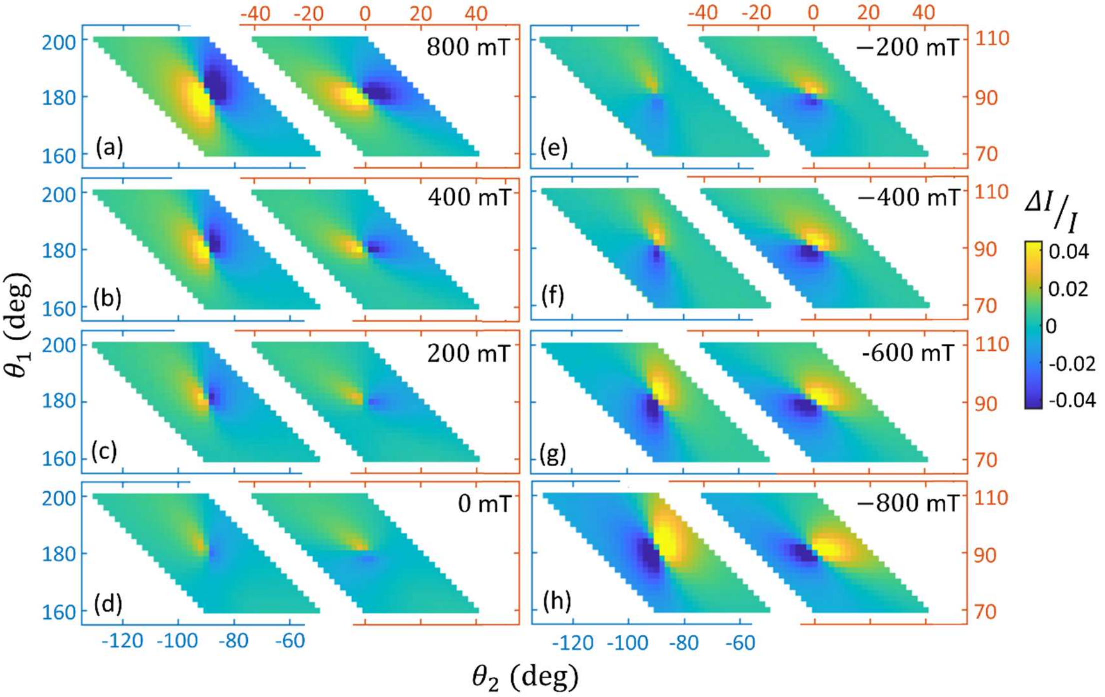

Figure 4.4 Sequence of experimentally measured $\Delta I/I$ (θ_1,θ_2) color-coded maps obtained for four different fields, namely, $\mu_0 H = 800, 400, 200, 0, -200, -400, -600$ and -800 mT, The data correspond to measurements on the sample represented in Fig. 4.1(b) with the GME setup shown in Fig. 4.3(b). The two color-coded maps contained in each subfigure show data around the s−p (left map, blue axis) and p−s (right map, orange axis) crossing-point configurations of the polarizers. The color-scale on the right side of the figure applies to all subfigures.

The data acquisition method and the data analysis explained in Chapter 3, Section 3.4, and that I show in an exemplary fashion in Figs. 4.4 and 4.5, is repeated for every applied field value of a hysteresis cycle, and thus, one can extract the full reflection matrix according to Eq. (4.1) for every field value. In this way, the field evolution of the MO parameters can be followed, as represented in Fig. 4.6.

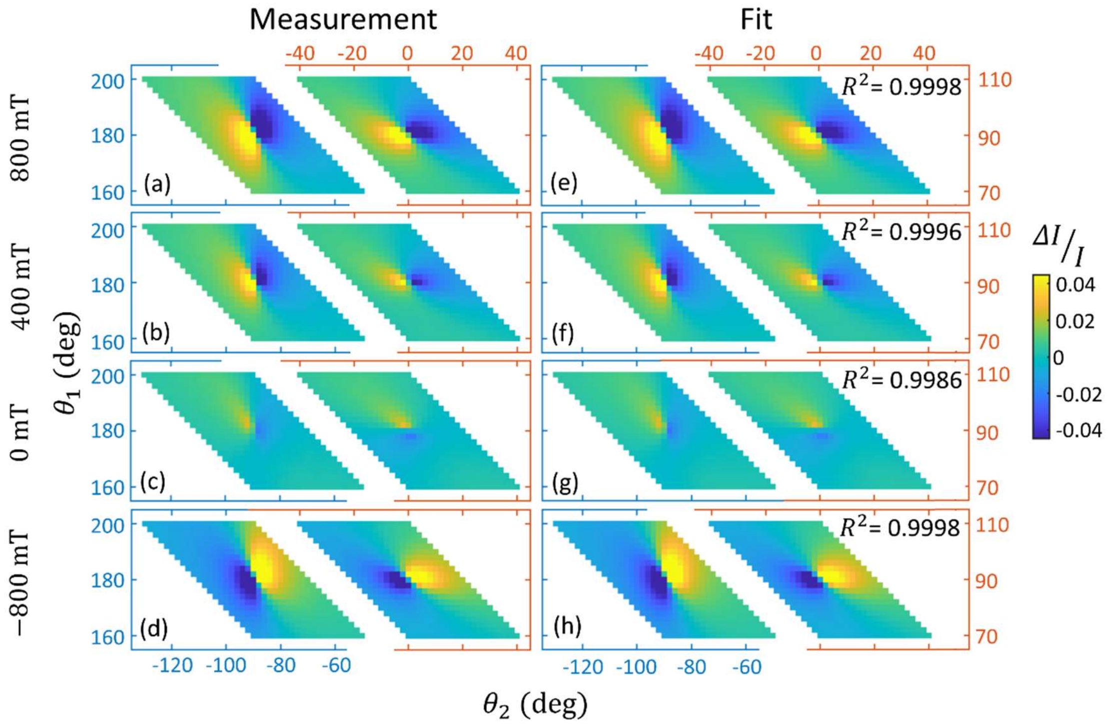

Figure 4.5 Selected experimentally measured $\Delta I/I$ (θ_1, θ_2) color-coded maps, already represented in Fig. 4.4, but here in comparison with the corresponding fits to Eq. (3.11), with the R^2 value displayed in the right top corner of every fit subfigure.

Specifically, in Fig. 4.6(a) and Fig. 4.6(b), one can see the behavior of the real and imaginary parts, respectively, of $\tilde{\alpha}$, $\tilde{\beta}$ and $\tilde{\gamma}$ vs the applied magnetic field for the same sample and conditions as in Fig. 4.4. The polar component $\tilde{\gamma}$ changes linearly with the field strength for sufficiently low field values while beginning to show a transition into sublinear behavior for higher field values. On the other hand, the in-plane magnetization components $\tilde{\alpha}$ and $\tilde{\beta}$ change only slightly except for the magnetization inversion at the coercive field, for which one can observe the abrupt change characteristic of a sharp hysteresis loop. The small variation of the in-plane magnetization-related components $\tilde{\alpha}$ and $\tilde{\beta}$ with field, best observed in Fig. 4.6(b) for the imaginary part of $\tilde{\beta}$ but present in the real and imaginary parts of both in-plane components, is associated with a decrease of the in-plane projection of the magnetization vector as the out-of-plane component increases. Moreover, there is a small rotation of the in-plane magnetization projection, which I wanted to generate as well. In the case of the MOKE-parameter field evolution for the in-plane magnetization setup geometry, shown in Fig. 4.3(a), all the magnetization rotation happens within the film plane, as no polar effect is present. The in-plane field component is much larger in this case, and thus, there are far larger in-plane magnetization rotations against the in-plane anisotropy, covering a broader angular range of φ_m, which means that both the real and imaginary parts of $\tilde{\alpha}$ and $\tilde{\beta}$ exhibit bigger variations in addition to magnetization inversion effects.

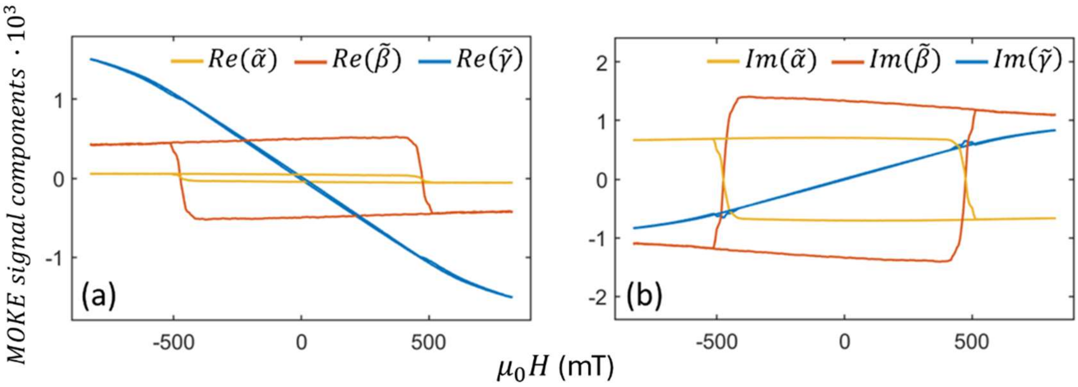

Figure 4.6 Applied field H *evolution of (a) the real part and (b) the imaginary part of the MOKE parameters* $\tilde{\alpha}$, $\tilde{\beta}$ *and* $\tilde{\gamma}$. *Data were measured on the sample displayed in Fig. 4.2(a) for an out-of-plane configuration of the GME of* $\Psi = 87$ *deg and an in-plane orientation of the sample of* $\varphi_0 = 45$ *deg.*

4.3.1 Experimental verification for in-plane magnetization cases

As already introduced, I first determined the reflection matrices for cases of in-plane magnetization states, including longitudinal (L-) and T-MOKE signal components but no polar effect, as a function of H, using the set up described in Fig 4.3(a). Here, I want to obtain a wide angular range of magnetization vector orientations to obtain a truly rigorous test for the correlation between the two in-plane MO components, $\tilde{\alpha}$ and $\tilde{\beta}$, as defined by Eqs. (4.5b) and (4.6b). Therefore, measurements near the HA orientation of the sample were performed. In addition, a certain number of slightly different orientations were used to acquire multiple separate and independent datasets [2]. In these measurements, the magnetization vector naturally aligns with the EA when no field is applied, and as the external field strength increases, the magnetization rotates towards the field orientation, applied along the longitudinal direction. In this way, the magnetization vector rotates covering a broad angular range, going from an almost purely transverse signal to a predominantly longitudinal case.

For four different sample orientation φ_0 angles, namely, $\varphi_0 = 96.25$, 91.25, 88.75, and 86.25 deg, GME measurements were performed and analyzed for many field values. Although GME measurements were made and analyzed for all field values and covered the entirety of hysteresis loops, for the following quantitative discussion of our measured data, I utilized only the experimental results where the magnetization remains in a stable macrospin state. In other words, to ensure that the macrospin conditions are fulfilled, I will perform the data interpretation for the experimental results obtained from the maximum applied magnetic field strength down to remanence. This condition ensures that the sample's magnetic state is

---

[2] Given that Eq. (4.1) is only dependent on the magnetization orientation, but it should not be affected in a direct and independent manner by the specific sample orientation or field strength utilized.

laterally uniform and free of domain formation (which usually happen at magnetization reversal), so that the magnetization vector can be described by a single, well defined and uniform magnetization vector. Therefore, interpreting the data through the reflection matrix formalism of Eq. (4.1) becomes quantitatively reliable.

Figure 4.7(a) displays the experimental results for the absolute values of the two in-plane MO coefficients, $|\tilde{\alpha}|$ and $|\tilde{\beta}|$. If Eq. (4.5b) is correct—as it must for the reflection matrix description in Eq. (4.1) to be valid— all data should fall onto a single ellipse, and indeed, one can see that they do. The data furthermore demonstrates that all four measurement sets for different sample orientations φ_0 follow the same ellipse relation, which is exactly the expected result given that the MOKE reflection matrix elements should not explicitly depend on the EA orientation φ_0. Error bars are not shown in Fig. 4.7(a), given that all error values are smaller than the individual dot sizes, illustrating that the GME measurements are highly accurate.

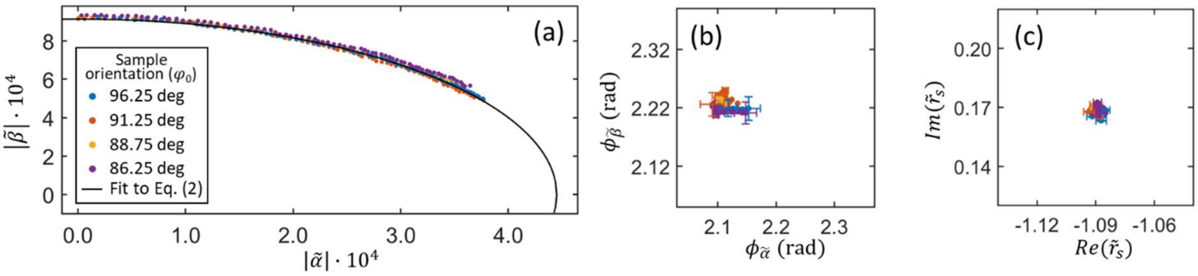

Figure 4.7 (a) Experimental data for $|\tilde{\beta}|$ vs $|\tilde{\alpha}|$ measured by using the in-plane GME geometry according to Fig. 4.3(a) for four different sample orientations φ_0, in comparison with the expected functional behavior, Eq. (4.5b); (b) $\phi_{\tilde{\beta}}$ vs $\phi_{\tilde{\alpha}}$ and (c) $Im(\tilde{r}_s)$ vs $Re(\tilde{r}_s)$ for the same datasets shown in (a). In subfigures (b) and (c), not all error bars are displayed for the purpose of clarity.

To prove the second test condition, the phases of $\tilde{\alpha}$ and $\tilde{\beta}$ are represented in Fig. 4.7(b), which within the error bars, all collapse onto one point, as predicted by Eq. (4.6), which is another necessary confirmation for the verification of Eq. (4.1). Finally, the analyzed data for the purely optical parameter $\tilde{r}_s$ are displayed in Fig. 4.7(c), with the vertical axis being the imaginary component and the horizontal axis its real component. Also in this plot, the resulting data points overlap, confirming that the pure optical parameter $\tilde{r}_s$ that I can also retrieve by means of GME measurements is independent from the magnetization orientation. This result reaffirms the description of $\boldsymbol{R}$ according to Eq. (4.1), which has clearly separated MOKE and purely optical elements. Thus, my entire set of in-plane magnetization data is not only fully consistent with Eq. (4.1) but confirms the derived relations for the in-plane MOKE effect given by Eqs. (4.5b) and (4.6b) to a very high degree of precision, with average deviations being $< 0.7\ \%$ of the respective full transverse or longitudinal effects.

4.3.2 Experimental verification for arbitrary magnetization orientations

To test the validity of the reflection matrix model under the most general magnetization conditions, I extended the study to configurations where the magnetization vector includes an out-of-plane component. These cases involve the polar magneto-optical Kerr effect (P-MOKE), in addition to the in-plane components. This three-dimensional magnetization state is captured by Eqs. (4.5a) and (4.6a), which are both directly derived from the fundamental expression of the reflection matrix in Eq. (4.1). As in the in-plane study, the GME methodology was utilized to generate several datasets, such as the one shown in Fig. 4.4, and determined the reflection matrix parameters for each applied magnetic field value as represented in Fig 4.6.

To introduce an out-of-plane component to the magnetization vector, I utilized the GME setup represented in Fig. 4.3(b). In all our measurements, Ψ and Ω were kept fixed at the values described above, and several datasets were taken for different in-plane orientations φ_0 to enable a relevant variation of the magnetization vector orientation and thus rigorous testing of Eq. (4.1). Specifically, four different in-plane sample orientations were measured, namely, $\varphi_0 = 60$, 45, 30, and 15 deg.

The results for the obtained absolute values of $\tilde{\alpha}$ and $\tilde{\beta}$ for these four sample orientations are presented in Fig. 4.8. In contrast to the in-plane case, where the elliptical relation governed by Eq. (4.5b) holds, here the data deviate from that form. In this three-dimensional (3D) magnetization case, $|\tilde{\alpha}|$ and $|\tilde{\beta}|$ are no longer correlated by means of the ellipse equation, Eq. (4.5b). However, the four datasets exhibit a tangential relationship to the ellipse equation, as shown comparatively in black in Fig. 4.8. This is due to the reduction of the in-plane projection of the magnetization as it rotates out of plane.

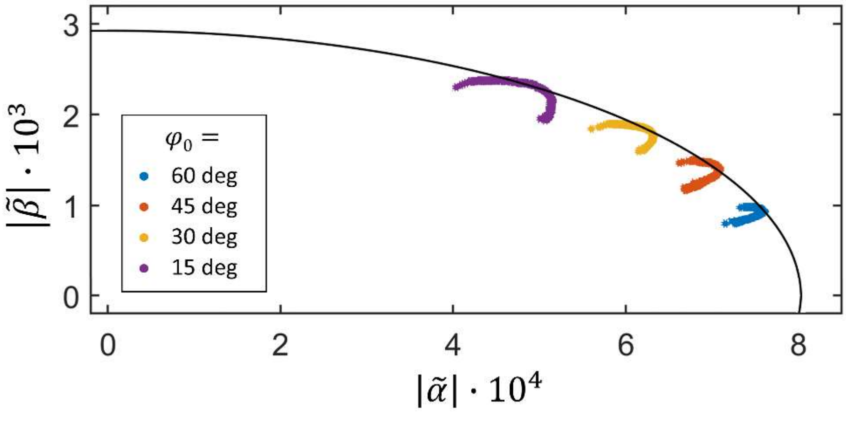

Figure 4.8. Experimental data for $|\tilde{\beta}|$ *vs* $|\tilde{\alpha}|$ *measured by using the out-of-plane GME geometry according to Fig. 4.3(b) for four different sample orientations* φ_0*, in comparison with the expected in-plane functional behavior; the line represents the ellipse equation boundary, which is tangential to the data.*

Instead, for the most general magnetization orientation scenario, $|\tilde{\alpha}|$, $|\tilde{\beta}|$, and $|\tilde{\gamma}|$ must be related by the ellipsoid equation, Eq. (4.5a), to be consistent with the form of $\boldsymbol{R}$ in Eq. (4.1). Indeed, our experimental data follow Eq. (4.5a) very precisely, as one can see in the 3D projection plot in Fig. 4.9(a), where the four lines represent the measured data for the four different in-plane orientations φ_0, and the surface represents the ellipsoid fit result. The mean relative error between the data and the ellipsoid fit result is $< 2.5\ \%$ for all four datasets. The ellipse equation that encircles the data in Fig. 4.8 corresponds hereby to the equatorial ellipse of the ellipsoid.

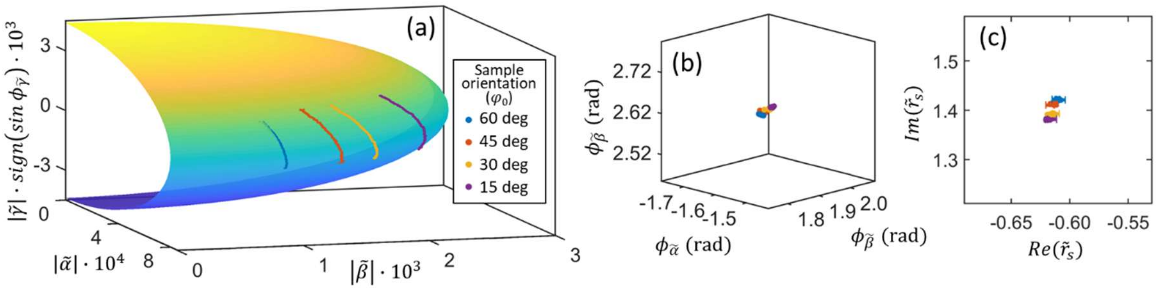

Figure 4.9 (a) Projection of the three-dimensional (3D) behavior of the relation between $|\tilde{\alpha}|$, $|\tilde{\beta}|$, and $|\tilde{\gamma}|$ for out-of-plane GME measurements made for four different φ_0 angles; the ellipsoid surface is obtained from a least squares fit of the experimental data to Eq. (4.5a); (b) quasi-3D plot of $\phi_{\tilde{\alpha}}$, $\phi_{\tilde{\beta}}$, and $\phi_{\tilde{\gamma}}$ for all measured data points; (c) $Im(\tilde{r}_s)$ vs $Re(\tilde{r}_s)$ data obtained for the entire measurement set.

The relations between the phases $\phi_{\tilde{\alpha}}$, $\phi_{\tilde{\beta}}$, and $\phi_{\tilde{\gamma}}$ are shown in Fig. 4.9(b). As one can see, all the data points collapse onto one point, in agreement with the derived condition, Eq. (4.6a). Finally, the resulting purely optical parameters are analyzed and displayed in Fig. 4.9(c), being all in close proximity to one another. This leads us to the same conclusion that was obtained in conjunction with Fig. 4.7(c), namely, the optical parameter $\tilde{r}_s$ remains independent from the applied magnetic field and sample magnetization state. However, the collapse is not quite as good as in the case of the pure in-plane magnetization data in Fig. 4.7(c). This difference likely arises from the wider range of in-plane orientation angles φ_0 here, in conjunction with optical anisotropy that can occur in oxide overcoats on top of epitaxial metal films [24]. This interpretation is supported by the fact that the variation within each set of data for fixed φ_0 is far smaller than between the datasets.

It is important to mention that for the derivation of Eq. (4.1) and accordingly Eqs. (4.5) and (4.6), no optical anisotropy is considered, and thus the existing deviations in Fig 4.9(c) are representative of the idealized dielectric tensor description and not of the lack of precision of the derivation of the reflection matrix by means of electromagnetic theory. Therefore, despite this modest deviation from the ideal case, the observed behavior still supports the general conclusion that the optical properties are decoupled from the magnetization direction and all the findings here are fully consistent in a quantitatively precise manner with Eqs. (4.5a) and (4.6a) and thus Eq. (4.1).

It is worth noting that the numerical values of the MOKE coefficients in Figs. 4.8 and 4.9 differ substantially from those reported for the in-plane configuration shown in Fig. 4.7. For example, the maximum value of $\tilde{\beta}$ is $\sim 3 \cdot 10^{-3}$ in Figs. 4.8 and 4.9(a), while it is only $\sim 9 \cdot 10^{-4}$ for the in-plane case in Fig. 4.7(a). There are also numerical differences if one compares the phase values and the pure optical parameter $\tilde{r}_s$ between Figs. 4.7 and 4.9. These differences are due to the two very different angles of incidence that were used for the corresponding measurements, being $\Omega = 70$ deg for the general magnetization case (Figs. 4.8 and 4.9) and $\Omega = 26$ deg for the in-plane magnetization case (Fig. 4.7).

4.3.3 Deviations due to MO anisotropy

Previous studies have reported deviations from the reflection matrix model given by Eq. (4.1) which were associated with a lack of isotropy in the MO coupling constant in anisotropic single-crystal samples [8–10,25]. Since my sample is a uniaxial single crystal, it is important to explore whether such deviations can also occur under specific measurement conditions and, more importantly, whether they can be detected using the GME methodology. In this subsection, I explore and verify that I can detect those deviations, which also confirms the precision and general viability of my experimental approach.

Let me remind you of the expression of the dielectric tensor for an optically and magneto-optically isotropic material and under linear MO approximation:

$$\varepsilon = N^2 \begin{pmatrix} 1 & iQm_z & -iQm_y \\ -iQm_z & 1 & iQm_x \\ iQm_y & -iQm_x & 1 \end{pmatrix}, \tag{4.8}$$

with N being the refractive index of the medium, Q the MO coupling constant and (m_x, m_y, m_z) the cartesian components of the magnetization vector. Both N and Q are wavelength dependent complex quantities. Now, for crystals with uniaxial symmetry, two different MO coupling factors can occur, namely $Q_{\parallel}$ and $Q_{\perp}$, for magnetizations along and perpendicular to the symmetry axis (c-axis), respectively, so that in the absence of optical anisotropy, the dielectric tensor now is

$$\varepsilon = N^2 \begin{pmatrix} 1 & iQ_{\perp}m_z & -iQ_{\perp}m_y \\ -iQ_{\perp}m_z & 1 & iQ_{\parallel}\, m_x \\ iQ_{\perp}m_y & -iQ_{\parallel}m_x & 1 \end{pmatrix}, \tag{4.9}$$

for the specific case in which the c-axis is oriented along the x-axis [25]. In a more general case yet, where the crystalline c-axis is in the xy plane but rotated an angle φ_0 with respect to the x-axis, some of the dielectric tensor elements are further modified:

$$\varepsilon'_{13} = -\varepsilon'_{31} = -iN^2 Q_{\parallel}\left[(1+\tau\cos^2\varphi_0)m_y - \tau\cos\varphi_0\sin\varphi_0\, m_x\right] \tag{4.10}$$

$$\varepsilon'_{23} = -\varepsilon'_{32} = iN^2 Q_{\parallel}\left[(1+\tau\sin^2\varphi_0)m_x - \tau\cos\varphi_0\sin\varphi_0\, m_y\right] \tag{4.11}$$

for which we have utilized the MO anisotropy coefficient $\tau = (Q_{\perp} - Q_{\parallel})/Q_{\parallel}$. From Eqs. (4.10) and (4.11), one can see that these particular off-diagonal tensor elements most generally depend on both in-plane magnetization components m_x and m_y instead of only one each.

To prove the presence of MO anisotropy-induced deviations in the reflection matrix expression, I returned to the in-plane magnetization geometry but intentionally moved away from the HA condition. For those selected measurement conditions, relevant levels of the MO anisotropy effect are expected. Specifically, I use relevantly smaller φ_0 values, namely $\varphi_0 =$ 88.75, 83.75, 78.75, and 73.75 deg. In this case, the MOKE elements of $\boldsymbol{R}$ can exhibit the anomalous magnetization dependence described by Eqs. (4.10) and (4.11). Therefore, the longitudinal term $\tilde{\alpha}$ of Eq. (4.1) could be expressed as a linear combination of m_x and m_y, namely,

$$\tilde{\alpha} = \tilde{\alpha}_L \cdot m_x + \tilde{\alpha}_T \cdot m_y, \tag{4.12}$$

with $\tilde{\alpha}_L$ and $\tilde{\alpha}_T$ being the linear coefficients for the conventional longitudinal and the anomalous transverse magnetization signals, respectively [25].

After the analysis of our GME measurements, the reflection matrix parameters are extracted and the results for this far wider φ_0 orientation range are shown in Fig. 4.10. In Fig. 4.10(a), the absolute value relationship between $|\tilde{\beta}|$ and $|\tilde{\alpha}|$ continues to follow the elliptical curve defined by Eq. (4.5b). However, Fig. 4.10(b) reveals deviations from the expected phase behavior for some data points: specifically, the phase of $\tilde{\alpha}$ does not remain constant, thus not fulfilling the second test condition given by Eq. (4.6). On the other hand, Fig. 4.10(c) shows that the purely optical term $\tilde{r}_s$ remains stable and independent of the magnetization state, just as observed in earlier measurements (see Figs. 4.7(c) and 4.9(c)). This reinforces the conclusion that the observed deviation in $\phi_{\tilde{\alpha}}$ is of magnetic origin and not due to changes in the optical properties.

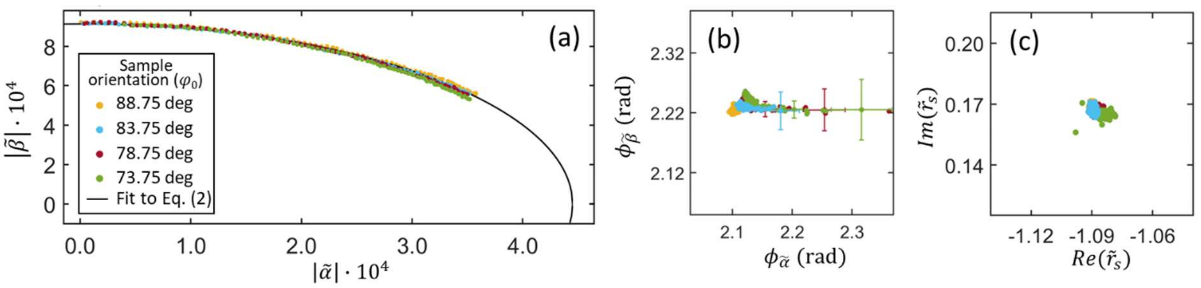

Figure 4.10 (a) Representation of the relation between $|\tilde{\beta}|$ and $|\tilde{\alpha}|$, for the in-plane GME geometry for a different set of φ_0 angles, plus the fit function of the data to Eq. (4.5b); (b) $\phi_{\tilde{\beta}}$ vs $\phi_{\tilde{\alpha}}$ and (c) $Re(\tilde{r}_s)$ vs $Im(\tilde{r}_s)$ for the same datasets shown in (a). In subfigures (b) and (c), not all the error bars are displayed for the purpose of clarity.

The anomalous magnetization state dependence of $\phi_{\tilde{\alpha}}$ would impact the accuracy of MOKE measurements, if data were not properly interpreted, given that it is associated with a deviation from Eq. (4.1). To analyze this deviation in a systematic way, I plotted the phase of $\tilde{\alpha}$ as a function of its absolute value, as shown in Fig. 4.11(a). The lines are the resulting fitted curves to Eq. (4.12), which match the data closely. The observed trends highlight that the deviation becomes most pronounced for small values of $|\tilde{\alpha}|$, which correspond to magnetization states with minimal m_x and dominant m_y for all sample orientations. An additional trend can be observed with the sample orientation angle, increasing the deviation for smaller φ_0 angles.

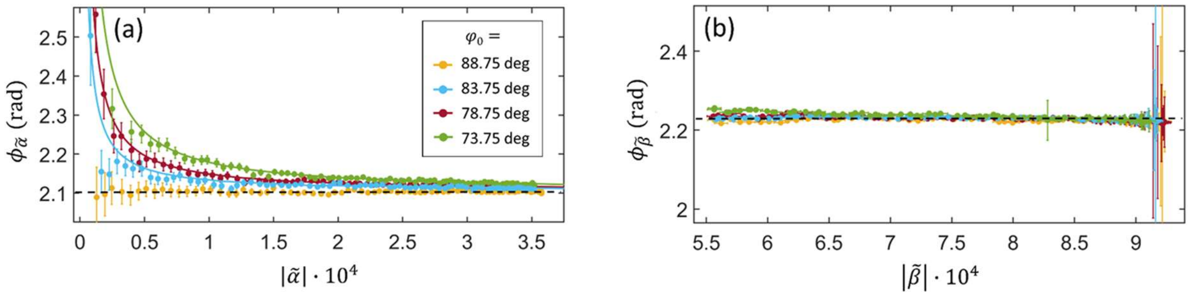

Figure 4.11 Experimental data, measured for the in-plane GME geometry, representing (a) $\phi_{\tilde{\alpha}}$ vs $|\tilde{\alpha}|$, with the lines corresponding to fitting the data to Eq. (4.12) and (b) $\phi_{\tilde{\beta}}$ vs $|\tilde{\beta}|$, for a set of sample orientations φ_0. The dashed black lines in (a) and (b) represent constant values of $\phi_{\tilde{\alpha}}$ and $\phi_{\tilde{\beta}}$, respectively, and act as guides to the eye.

The anomalous transverse contribution $\tilde{\alpha}_T$ is rather small in magnitude, but once m_x gets very small in comparison with m_y, the second term in Eq. (4.12) can contribute relevantly. Given that both $\tilde{\alpha}_T$ and $\tilde{\alpha}_L$ prefactors can have different phases, the overall $\phi_{\tilde{\alpha}}$ changes with the magnetization state, which is exactly what the data show, if one is sufficiently far away from the HA field orientation. Moreover, this $\phi_{\tilde{\alpha}}$ dependency from the magnetic state decreases as φ_0 approaches 90 deg, which leads to a full restoration of the exactness of Eq. (4.1) for $\varphi_0 = 0, \pm 90$, and 180 deg because, in this case, the independent and crystallographically defined MO constants apply exclusively to the L- and T-MOKE, respectively, without intermixing [25].

This explains why no deviation was observed in our earlier measurements shown in Fig. 4.7, given that all the selected sample orientations were close to $\varphi_0 = 90$ deg. Measurements for even smaller φ_0 angles are not shown in Fig. 4.7 because the rotation range of the magnetization vector is quite small in this case and furthermore does not allow for the generation of small $\tilde{\alpha}$ values due to hysteretic switching. This is presumably also the reason why we do not observe a similar effect for $\tilde{\beta}$ in Fig. 4.7(b). Fundamentally, the transverse component $\tilde{\beta}$ is expected to follow the relation:

$$\tilde{\beta} = \tilde{\beta}_L \cdot m_x + \tilde{\beta}_T \cdot m_y, \tag{4.13}$$

with the anomalous $\tilde{\beta}_L$ coefficient value being far smaller than the conventional $\tilde{\beta}_T$ coefficient. To show the influence of $\tilde{\beta}_L$, it would be therefore necessary to access magnetization states with very small m_y values or correspondingly very small $|\tilde{\beta}|$ values, which are, however, not accessible in our experiment. For the $|\tilde{\beta}|$ range that our experiments can cover, this anomalous dependence is not observed, and $\phi_{\tilde{\beta}}$ remains constant, as we see in Figs. 4.7(b), 4.9(b) and 4.10(b).

4.4 Conclusions and outlook

In this chapter, I studied the accuracy of the reflection matrix description in linear MO. To conduct a meaningful evaluation, I developed a suitable strategy for testing the $\boldsymbol{R}$ accuracy experimentally, obtaining two meaningful test conditions. Central to this approach was the design and fabrication of a suitable sample, which consisted of a uniaxial magnetic sample with in-plane EA and macrospin behavior. These sample characteristics enabled the systematic variation of the angle of the magnetization vector while preserving its absolute value constant, which is essential for the quantitative application of the reflection matrix model. Furthermore, I utilized GME as the characterization technique because it has the advantage of determining all the reflection matrix parameters in a single experiment with high precision.

It was found that, both for in-plane magnetization cases as well as for general magnetization cases that include an out-of-plane component, all test conditions derived were fulfilled to a very high degree of numerical precision. Thus, I was able to experimentally verify that the conventionally utilized reflection matrix description, given by Eq. (4.1), is indeed completely correct if the material under investigation fulfills the assumptions under which Eq. (4.1) was derived. Those include (i) that the pure optical response of the material is isotropic and (ii) that the MO coupling is isotropic as well. Furthermore, the derivation of Eq. (4.1) utilizes the fact that (iii) MO effects constitute a small perturbation of the optics so that considerations of linear MO terms are sufficient. Existing deviations found in $\tilde{r}_s$ are representative of the idealized dielectric tensor description, considered optically isotropic, and not of the lack of precision of the derivation of the reflection matrix by means of electromagnetic theory.

Moreover, as GME enables the acquisition of quantitatively very precise results, we were also able to detect small deviations in our measurements from Eq. (4.1). They occur under specifically chosen experimental conditions and are related to the fact that Eq. (4.1) is not exactly applicable in our experiment, given that our sample exhibits weak MO anisotropy, which can in principle occur for any anisotropic magnetic sample. Once MO anisotropy is explicitly considered in the derivation of a reflection matrix analogous to Eq. (4.1), complete agreement between the modified matrix terms and our experimental data is reestablished.

The use of phase changes to identify non-uniform magnetization states and separate them clearly by experimental means from MO anisotropy will be used as a starting point in the next chapter.

Chapter references

[1] A. Berger and M. R. Pufall, Generalized magneto-optical ellipsometry, Appl. Phys. Lett. **71**, 965 (1997).

[2] A. Berger and M. R. Pufall, Quantitative vector magnetometry using generalized magneto-optical ellipsometry, J. Appl. Phys. **85**, 4583 (1999).

[3] S. Višňovský, Magneto-optical ellipsometry, Czechoslov. J. Phys. **36**, 625 (1986).

[4] J. Zak, E. R. Moog, C. Liu, and S. D. Bader, Universal approach to magneto-optics, **89**, 107 (1990).

[5] M. Schubert, Polarization-dependent optical parameters of arbitrarily anisotropic homogeneous layered systems, Phys. Rev. B - Condens. Matter Mater. Phys. **53**, 4265 (1996).

[6] S. C. Shin and C. Y. You, Generalized analytic formulae for magneto-optical Kerr effects, J. Appl. Phys. **84**, 541 (1998).

[7] M. Schubert, T. E. Tiwald, and J. A. Woollam, Explicit solutions for the optical properties of arbitrary magneto-optic materials in generalized ellipsometry, Appl. Opt. **38**, 177 (1999).

[8] T. Higo et al., Large magneto-optical Kerr effect and imaging of magnetic octupole domains in an antiferromagnetic metal, Nat. Photonics **12**, 73 (2018).

[9] F. M. Bartram, S. Sorn, Z. Li, K. Hwangbo, S. Shen, F. Frontini, L. He, P. Yu, A. Paramekanti, and L. Yang, Anomalous Kerr effect in SrRuO3 thin films, Phys. Rev. B **102**, 140408 (2020).

[10] T. Uchimura et al., Observation of domain structure in non-collinear antiferromagnetic Mn3Sn thin films by magneto-optical Kerr effect, Appl. Phys. Lett. **120**, 172405 (2022).

[11] C. Martín Valderrama, M. Quintana, A. Martínez-De-Guerenu, T. Yamauchi, Y. Hamada, Y. Kurokawa, H. Yuasa, and A. Berger, Insertion layer magnetism detection and analysis using transverse magneto-optical Kerr effect (T-MOKE) ellipsometry, J. Phys. D. Appl. Phys. **54**, 435002 (2021).

[12] P. Riego, *Magneto-Optical characterization of magnetic thin films and interface structures* (Ph.D. Thesis, University of the Basque Country, 2019).

[13] J. A. Arregi, *Magneto-Optical Ellipsometry and Magnetometry of Thin Films and Multilayers* (Ph.D. Thesis, University of the Basque Country, 2020).

[14] O. Idigoras, A. K. Suszka, P. Vavassori, B. Obry, B. Hillebrands, P. Landeros, and A. Berger, Magnetization reversal of in-plane uniaxial Co films and its dependence on epitaxial alignment, J. Appl. Phys. **115**, 083912 (2014).

[15] P. Riego, L. Fallarino, C. Martínez-Oliver, and A. Berger, Magnetic anisotropy of uniaxial ferromagnets near the Curie temperature, Phys. Rev. B **102**, 174436 (2020).

[16] D. Weller, H. Brändle, G. Gorman, C. J. Lin, and H. Notarys, Magnetic and magneto-optical properties of cobalt-platinum alloys with perpendicular magnetic anisotropy, Appl. Phys. Lett. **61**, 2726 (1992).

[17] W. Yand, D. N. Lamberth, and D. E. Laughlin, Unicrystal Co – alloy media on Si (110), J. Appl. Phys. **85**, 110 (1999).

[18] O. Idigoras, U. Palomares, A. K. Suszka, L. Fallarino, and A. Berger, Magnetic properties of room temperature grown epitaxial Co 1-xRux-alloy films, Appl. Phys. Lett. **103**, 102410 (2013).

[19] L. Fallarino, B. J. Kirby, M. Pancaldi, P. Riego, A. L. Balk, C. W. Miller, P. Vavassori, and A. Berger, Magnetic properties of epitaxial CoCr films with depth-dependent exchange-coupling profiles, Phys. Rev. B **95**, 134445 (2017).

[20] L. Fallarino, P. Riego, B. J. Kirby, C. W. Miller, and A. Berger, Modulation of Magnetic Properties at the Nanometer Scale in Continuously Graded Ferromagnets, Materials (Basel). **11**, 251 (2018).

[21] M. Quintana, A. Melendez, C. Martín Valderrama, L. Fallarino, and A. Berger, Temperature-Independent Coercivity in Compositionally Graded Ferromagnetic Multilayers M., Phys. Rev.

Appl. **18**, 054024 (2022).
[22] E. C. Stoner, F. R. S. Wohlfarth, and E. P. Wohlfarth, A mechanism of magnetic hysteresis in heterogeneous alloys, **240**, 826 (1948).
[23] M. Grimsditch, E. E. Fullerton, and R. Stamps, Exchange and anisotropy effects on spin waves in epitaxial Co films, Phys. Rev. B - Condens. Matter Mater. Phys. **56**, 2617 (1997).
[24] J. B. González-Díaz, J. A. Arregi, E. Bergaretxe, M. J. Fertin, O. Idigoras, and A. Berger, Anomalous magneto-optical behavior of uniaxial Co/CoO bilayer films, J. Magn. Magn. Mater. **325**, 147 (2013).
[25] J. A. Arregi, P. Riego, and A. Berger, What is the longitudinal magneto-optical Kerr effect?, J. Phys. D. Appl. Phys. **50**, 03LT01 (2017).

Chapter 5

Layer-resolved vector magnetometry

This chapter introduces the experimental realization and theoretical modeling of layer-resolved vector magnetometry in epitaxial multilayers. The central goal is to establish a generalized magneto-optical ellipsometry (GME)-based methodology capable of tracking individual magnetization vectors within layered magnetic structures. To address this central goal, three major steps were devised, whose accomplishments are in each case an individual goal by themselves:

(i) GME-based detection of non-collinear magnetization states
(ii) Development of layer-resolved vector magnetometry in multilayer structures with two ferromagnetic (FM) layers
(iii) Initial attempts to extend the methodology to three FM layers, including the perspectives and limitations of the methodology.

Following this step-by-step approach, I first experimentally studied the relationship between non-collinear magnetization states in FM multilayers and their resulting magneto-optical (MO) properties. Hereby, it was observed that it is the phases of the complex-valued MO parameters that are especially sensitive towards non-collinear magnetization states and enable their unambiguous detection.

Secondly, I demonstrated the ability of a single MO reflection experiment to achieve layer-resolved vector magnetometry in multilayers with two FM layers. Specifically, the magnetization angles of two different FM layers were obtained independently as a function of the applied field, for a set of epitaxial FM/ non-magnetic (NM)/ FM heterostructure multilayer samples. Moreover, it was observed that the magnetization switching of one layer can trigger a discontinuous shift of the magnetization angle in the second layer if FM interlayer coupling is present. The obtained behavior was successfully reproduced using a model of two coupled macrospins, corroborating even the initially unexpected aspects of the experimental results and thus reinforcing the sensitivity and reliability of GME-based experimental layer-resolved vector magnetometry.

Finally, the GME set-up was implemented by incorporating a tunable-wavelength light source. This provided the possibility to collect independent sets of data for the same magnetization reversal process, which should then allow for the experimental determination of the magnetization vector angles of three separate FM layers.

This chapter is organized as follows. Section 5.1. presents the introduction and motivation. Section 5.2 describes the details and the fabrication procedures of the multilayer samples. Next, Section 5.3 presents the experimental results in four subsections: verification of the single layer superposition assumption, detection of non-collinear states in two FM layer systems, layer-resolved vector magnetometry in two FM layer systems, and initial results on layer-resolved vector magnetometry in multilayers containing three FM layers. Section 5.4 provides concluding remarks and outlines future directions for the development of depth-resolved vector magnetometry.

5.1 Introduction and motivation

To test the GME methodology and characterize individual layer magnetic responses, I designed and fabricated suitable multilayer samples that present layer-dependent non-collinear magnetization vector states. These multilayers have different FM layers with differing anisotropy strengths and whose coupling is controlled by tuning the thickness of a NM interlayer. In this way, I was able to access a continuum from strongly coupled collinear states to weakly coupled or frustrated non-collinear states by increasing the thickness of the NM interlayer. All magnetic layers were engineered to exhibit macrospin behavior with a shared in-plane easy axis (EA), allowing deterministic control over their magnetization vectors as a function of applied field magnitude and orientation.

Central to this methodology is the assumption that the overall MO response of the multilayer can be interpreted as a linear superposition of the individual layer contributions. While this assumption is valid under many conditions, its applicability in systems with strong interlayer coupling or optical interference effects must be carefully evaluated. Therefore, I verified the layer superposition assumption and identified the limits of its validity. Next, through GME, I determined the full reflection matrix of each multilayer sample as a function of external field and extracted the associated MO Kerr effect (MOKE) coefficients. From these, first, I identified non-collinear vector magnetization states, and second, I reconstructed the field evolution of each layer's magnetization vector. These results are further corroborated with a macrospin model that captures the interplay of Zeeman energy, anisotropy, and exchange coupling, providing a consistent theoretical framework for interpreting the experimental data.

5.2 Sample design and fabrication

To experimentally generate and characterize non-collinear magnetization states in multilayer systems, I designed a model system in which the magnetic configuration can be tuned from collinear to non-collinear by applying an external magnetic field. This is achieved by combining different FM layers separated by a NM material with the following characteristics:

- The FM layers share the same in-plane uniaxial anisotropy axes but have different magneto-crystalline anisotropy strengths. This condition ensures that the different FM layers will exhibit distinct magnetization responses under an applied field, especially when the field is oriented away from the EA. Different anisotropies can be achieved by utilizing different materials for each FM layer, which must have the same lattice type nonetheless, so that the multilayer structure grows epitaxially and an alignment of the EAs of both layers is achieved.
- The NM interlayer should enable a tunable level of FM interlayer exchange coupling, so that the samples can move from a scenario of strong field induced non-collinearity to one in which strong FM interlayer exchange coupling forces the magnetization of the two FM layers to align and suppress non-collinear magnetization states.

As already briefly mentioned in Chapter 2, when magnetic layers are separated by a non-magnetic layer, the magnetizations of the layers are coupled to each other by an exchange interaction through the electrons of the spacer layer. This is known as interlayer exchange coupling. A specific type of interlayer exchange coupling is the FM interlayer exchange coupling, which describes the effect of magnetic interactions in between FM layers that are physically separated by an interlayer, which should be either NM or weakly FM in order to mediate a weak FM interlayer exchange coupling [1–3].

One of the key impacts of FM interlayer exchange coupling is associated with the way adjacent FM films react to an applied magnetic field H. The existence of a large interlayer exchange coupling strength J leads to the synchronization of the magnetic field responses of the different FM layers for every applied field value and orientation. On the other hand, a weak or absent J will allow for primarily independent magnetization rotations or reversals, exhibiting a transition from collinear alignment to non-collinear alignment as the field is increased, since for no applied field the magnetizations will lie along the aligned EAs.

In Fig. 5.1(a), the case of a large J is illustrated for a two magnetic film system with the corresponding magnetizations $\vec{m}_1$ and $\vec{m}_2$ being strongly coupled and the corresponding angles of the magnetization vectors with respect to the applied field orientation being equal, i.e. $\varphi_{m_1} = \varphi_{m_2}$. The external field H is applied with an angle φ_0 away from the EA, which makes the magnetization vectors rotate for an extended field range.

On the other hand, in Fig. 5.1(b), J is small and, for the same conditions, so that the two magnetization vectors of the layers, $\vec{m}_1$ and $\vec{m}_2$, are sufficiently independent, resulting in a field strength induced transition from $\varphi_{m_1} = \varphi_{m_2}$ to $\varphi_{m_1} \neq \varphi_{m_2}$ assuming that the external field H is applied with an angle φ_0 away from the EA.

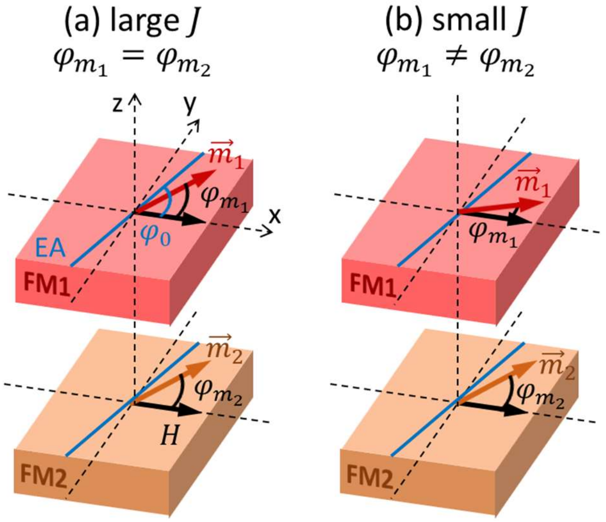

Figure 5.1 Schematic of the magnetization behavior of two coupled FM layers, FM1 and FM2, depending on whether they have (a) strong or (b) weak FM interlayer exchange coupling J. The cartesian axes with respect to the surface plane are defined, as well as the applied field direction (black arrow and label "H") and the EA orientation (blue line and label "EA"). The magnetization vectors are indicated with arrows and labels "$\vec{m}_1$" and "$\vec{m}_2$". In-plane magnetization angles φ_{m_1} and φ_{m_2} and the EA angle φ_0 are indicated and defined with respect to the applied field direction.

Given these two distinct cases, one would expect that the magnetic field dependent transition from collinear to non-collinear alignment of $\vec{m}_1$ and $\vec{m}_2$ with applied field is strongly dependent on the FM interlayer coupling strength J, being fully developed for small J values, while being suppressed for large J. In this regard, in the here exposed experimental approach I will tune the FM interlayer exchange coupling by changing the NM interlayer thickness, given that the magnetic coupling strength J is strongly dependent on it, and by choosing an external magnetic field angle far away from the EA of the films. Therefore, I will have a well-controlled and tunable system for generating non-collinear magnetization states. Tuning the level of FM interlayer exchange coupling in different samples between the FM layers in multilayers provides a good set for testing the robustness of the non-collinear magnetic detection and layer-resolved vector magnetometry methodology.

5.2.1 Multilayers with two FM layers

The simplest case of potentially non-collinear multilayers consists of two FM layers system, which are the samples I will describe in this subsection. The fabricated set of samples consists of single crystal magnetic multilayers, in which each of the magnetic layers is well represented in its magnetic state by a single magnetization angle, which in turn means that the magnetic film ought to exhibit a laterally uniform magnetic state (macrospin behavior) [4]. Accordingly, these multilayer samples contain a main FM$_1$/NM/FM$_2$ structure, as is schematically displayed in Fig. 5.2(a). The main FM$_1$/NM/FM$_2$ structure is a hexagonal close-packed (hcp) crystal structure with $(\mathbf{10\bar{1}0})$ crystal orientation formed by a 2.1 nm thick Co$_{0.86}$Pt$_{0.14}$ and a 2 nm Co magnetic layers, both having in-plane EA along the crystallographic c-axis, which are separated by a Co$_{0.59}$Ru$_{0.41}$ non-magnetic interlayer which also has hcp $(\mathbf{10\bar{1}0})$ crystal orientation and preserves the epitaxial alignment of the FM layers.

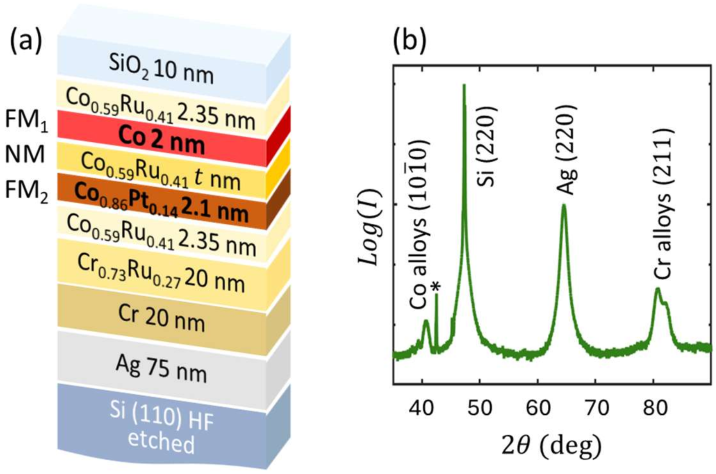

Figure 5.2 (a) Layer geometry and epitaxial sequence utilized in our sample series with the respective materials and thicknesses indicated; (b) exemplary $\theta - 2\theta$ XRD measurement scan of the t = 4 nm sample from our sample series; the corresponding crystallographic peaks associated with the epitaxial growth sequence are labelled Co alloys $(10\bar{1}0)$*, Si* (220)*, Ag* (220) *and Cr alloys* (211)*; the additional peak marked with a star corresponds to the Si* (220) *crystallographic plane and is generated by a secondary wavelength of our x-ray source.*

The specific alloy composition of the Co-Pt alloy with 14% Pt is chosen to assure good epitaxial growth while at the same time ensuring that the material is FM at room temperature and has a magneto-crystalline anisotropy constant larger than the pure Co layer. The Co-Ru non-magnetic interlayer alloy selected with 41% of Ru does mediate a FM interlayer exchange coupling J for sufficiently thin films and provides a good template for the epitaxial growth of the second FM layer [5]. Furthermore, it enables a tuning of J because its selected alloy composition makes it almost a FM in and by itself, and accordingly, its induced interface spin polarization falls off slowly on the nm length scale when put into contact with a FM layer [1,5].

In this way, the $Co_{0.59}Ru_{0.41}$ interlayer thickness t is varied from 0.5 to 6 nm, for different samples in the overall sample series in order to tune the FM interlayer coupling strength J in between the two FM layers within the different samples. As a result, the adjacent FM layers will be strongly coupled when t is small, and such samples can be expected to behave in an almost perfectly collinear way, independent from the applied magnetic field strength. As t increases, one can expect a transition to weakly coupled and eventual uncoupled magnetization behavior in between both layers. Following the same procedure as for the sample described in Chapter 4, to achieve the intended epitaxy and in-plane EA, the samples have been grown onto Si (110)-wafer substrates, which were first etched by hydrofluoric acid to remove the oxide layer. Afterwards, the following film sequence has been deposited by means of sputter deposition at room temperature in a 3 mTorr pure Ar atmosphere, to achieve good epitaxial quality [5,6]: 75 nm of Ag (110), 20 nm of Cr (211), 20 nm of $Cr_{0.73}Ru_{0.27}$ (211) and 2.35 nm of $Co_{0.59}Ru_{0.41}$ $(10\bar{1}0)$. The specific thickness and alloy compositions of the underlayer sequence have been chosen to assure that the FM layers are fully epitaxial [5,7]. Furthermore, the Co-Pt/Co-Ru/Co trilayer structure is covered by 2.35 nm of $Co_{0.59}Ru_{0.41}$ and 10 nm of SiO_2, to have symmetric interfaces for both FM layers and to protect the sample from oxidation. All alloy layers are grown by co-sputter deposition of the two materials forming the alloy.

Its structural properties have been characterized by x-ray diffraction (XRD) measurements, such as the one shown exemplary in Fig 5.2(b) for the sample with $t = 4$ nm. Figure 5.2(b) shows the $\theta - 2\theta$ measurements in which all the observed diffraction peaks correspond to the intended crystallographic planes for each of the deposited layers at the Cu-K_α wavelength, and therefore highlights the epitaxial nature of the samples, consistent with previous reports for similar growth sequences [6–10]. The additional peak at $2\theta = 42.3$ deg corresponds to the Si (220) crystallographic plane produced by the Cu-K_β wavelength radiation of the used x-ray source, and it is the only XRD-peak visible for this radiation. The quality of the XRD results also implies that the sample system has laterally uniform magnetization properties, which is important as it permits a quantitative accurate interpretation of macroscopic magnetization and MO data [7,11,12].

Additionally, to isolate the contributions of each FM layer, two reference samples with only one FM layer and the same total thickness were grown, for which the main $FM_1/NM/FM_2$ structure is substituted by

- Co (2 nm)/ $Co_{0.59}Ru_{0.41}$ (6.95 nm) and
- $Co_{0.59}Ru_{0.41}$ (6.85 nm)/ $Co_{0.86}Pt_{0.14}$ (2.1 nm), respectively.

These reference samples help disentangle overlapping MO signals in the two FM layer samples and aid in the validation of the layer-specific analysis.

To characterize the magnetic behavior, the Kerr rotation θ_K, which is proportional to the magnetization component along the field direction, was measured for different NM interlayer thicknesses. The resulting hysteresis loops (Fig. 5.3) illustrate the dependence of magnetic switching on coupling strength. In these measurements, the sample was oriented with its EA at an angle $\varphi_0 = 65$ deg away from the applied field direction.

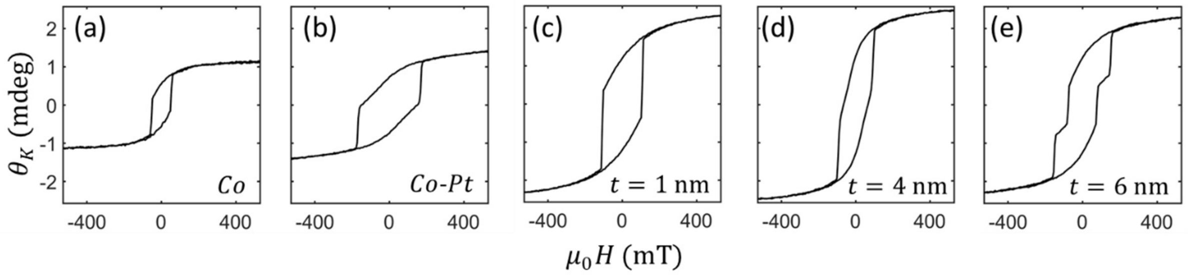

Figure 5.3 Experimentally determined hysteresis loops for the two reference samples (a,b) and for three magnetic bilayer samples having different interlayer thickness t *(c, d, e) by plotting the measured Kerr rotation* θ_K *as a function of the applied magnetic field strength H for a sample orientation of* $\varphi_0 = 65$ *deg.*

Figures 5.3(a,b,c) show a conventional FM hysteresis loop, with a single jump happening at the coercive field and a very significant gradual change that is associated with the rotation of the magnetization away from the EA by means of the applied field. This response is the expected behavior for a single magnetic film, which is also consistent with a bilayer sample with strong FM interlayer coupling (high-J case), so that the magnetic behavior in both layers is synchronized. Specifically, Figs. 5.3(a,b) correspond to the reference samples with only one FM layer, and Fig 5.3(c) corresponds to the sample with NM interlayer thickness $t = 1$ nm, as indicated in the bottom right corner of each subfigure.

Figure 5.3(e), on the other hand, shows an independent switching of the two FM films in the FM bilayer sample, and thus two jump segments occur in the hysteresis loop at two distinctively different field strengths. In addition, a significant gradual signal change is visible here as well, which is associated with a relevant magnetization rotation also in the case of an uncoupled or weakly coupled FM bilayer. These data were measured for the FM bilayer sample in which the NM interlayer thickness is 6 nm, and therefore no or only very small FM interlayer coupling should occur.

Figure 5.3(d) illustrates an intermediate case, where the NM interlayer thickness is $t = 4$ nm. Here, only a single jump is visible in addition to a non-monotonous slope modulation prior to the jump. Thus, the behavior neither fits to the fully coupled nor the uncoupled bilayer scenarios of Figs. 5.3(c) and (e), but represents a more complex collective behavior. Moreover, one can observe that the Kerr rotation θ_K of the samples with two FM layers reaches bigger values than those of the reference samples, as those have smaller total FM thickness.

These exemplary hysteresis loops show the different collective magnetization reversal processes for samples with different interlayer thicknesses and confirm that qualitatively different levels of FM interlayer coupling strengths are achieved by means of the devised sample design, just as intended. In turn, this means that the sample set can be expected to generate different levels of non-collinearity in field dependent measurements, and thus it enables to test the ability to monitor non-collinear magnetization states by means of MO measurements. These same samples, which show clearly distinct magnetization states for each FM layer, were used for both non-collinear detection and layer-resolved vector magnetometry for two FM layer structures.

5.2.2 Multilayers with three FM layers

After verifying that the non-collinear detection and layer resolved vector magnetometry works for bilayers, the next logical sample structure to advance further consists of growing multilayer samples with three FM layers. In a similar fashion, the three FM layers should be independent from each other while individually exhibiting macrospin behavior. The conditions and limitations for structures containing three FM layers are the following:

- Three different FM layers with different anisotropies.
- The insertion layers have to maintain the epitaxial growth, but the thickness and composition of this alloy should allow independent rotation of the FM layers. Similarly to the two FM layer samples, this means that the FM interlayer coupling would be weak or absent.
- The total structure has to be thin enough to access the information of all the layers by means of magneto-optics, i.e. the penetration depth of light should be bigger than the thickness of the whole multilayer structure.

With these conditions in mind, a set of multilayer samples was grown, containing a main $FM_1/NM/FM_2/NM/FM_3$ structure, as is schematically displayed in Fig. 5.4(a). The main structure is a hcp crystal structure with $(10\bar{1}0)$ crystal orientation, as for the two FM layer samples. Now, the FM layers have thickness of 2 nm and the alloy compositions are $Co_{0.91}Pt_{0.09}$, $Co_{0.82}Pt_{0.18}$ and Co, all having in-plane EA along the crystallographic c-axis, which are separated by a $Co_{1-x}Ru_x$ non-magnetic interlayer.

The specific alloy compositions of the FM layers (Co-Pt alloys with 9% and 18% of Pt) are chosen to enable good epitaxial growth while at the same time assuring that the material is FM at room temperature and has a magneto-crystalline anisotropy constant larger than the pure Co layer. I used the same base strategy as for the two FM layer samples, but utilized a $Co_{1-x}Ru_x$ alloy with less Co to get comparable coupling levels for thinner interlayers in an attempt to limit the total magnetic multilayer thickness in this case, making MOKE measurements viable. Therefore, different samples with different Co-Ru interlayer alloy compositions were grown, with 45%, 50% and 55% of Ru, providing a good template for the epitaxial growth of the second and third FM layers [5], mediating a FM interlayer exchange coupling for sufficiently thin films and furthermore exhibiting the associated NM layer thickness dependence wanted [1]. The thickness t is varied from 2 to 5 nm, for different samples in the overall sample series. The complete multilayer structure shown in Fig 5.4(a) is designed to achieve epitaxial growth and in-plane EA. Its structural properties have been characterized by x-ray diffraction (XRD) measurements, such as the one shown exemplary in Fig 5.4(b), in which all the observed diffraction peaks correspond to the intended crystallographic planes for each of the deposited layers. Reference samples with only one FM layer but same total thickness were also grown.

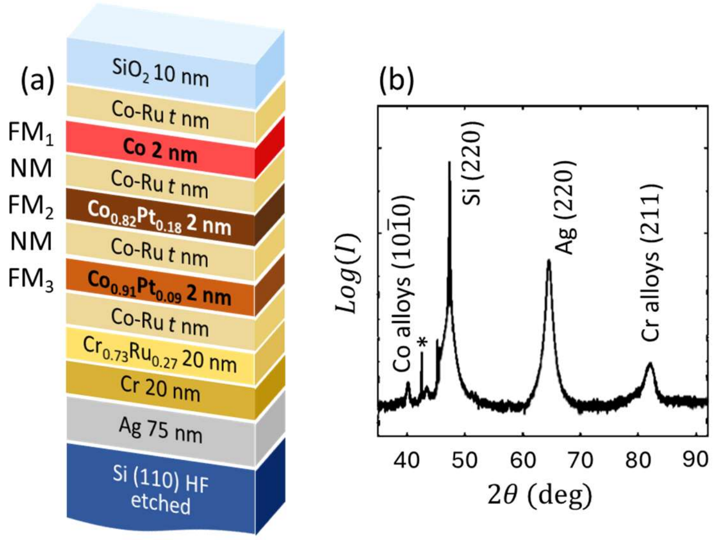

Figure 5.4 (a) Layer geometry and epitaxial sequence utilized in our sample series with the respective materials and thicknesses indicated; (b) exemplary $\theta - 2\theta$ *XRD measurement scans of four samples from our sample series; the corresponding crystallographic peaks associated with the epitaxial growth sequence are labelled Co alloys* $(10\bar{1}0)$*, Si* (220)*, Ag* (220) *and Cr alloys* (211)*; the additional peak marked with a star corresponds to the Si* (220) *crystallographic plane and is generated by a secondary wavelength of our x-ray source.*

To characterize the magnetic behavior, vibrating sample magnetometry (VSM) measurements were made for a sample orientation of $\varphi_0 = 15$ deg. The resulting normalized hysteresis loops (Fig. 5.5) illustrate the dependence of magnetic switching on the composition and thickness of the Co-Ru alloy in the interlayers. Figures 5.5(a-c) show the hysteresis loops for the reference samples:

- CoRu$_{0.50}$ (2 nm)/ CoPt$_{0.09}$ (2 nm)/ CoRu$_{0.50}$ (16 nm),
- CoRu$_{0.50}$ (8 nm)/ CoPt$_{0.18}$ (2 nm)/ CoRu$_{0.50}$ (8 nm),
- CoRu$_{0.50}$ (16 nm)/ Co (2 nm)/ CoRu$_{0.50}$ (2 nm).

The different coercive fields for each Co alloy concentration are clearly observed here. Figures 5.5(d-f) include the hysteresis loops for the same interlayer thickness of $t = 4$ nm but different

CoRu alloy concentrations. The trilayer FM samples with 45% and 50% of Ru have the intended independent switching of each FM layer, however, the trilayer with 55% of Ru does not show this behavior, indicating that for this Ru concentration the FM layers do not grow epitaxially anymore. Finally, Figs. 5.5(g-i) represent the hysteresis loops for an interlayer with 50% of Ru but different thicknesses, namely 2, 3 and 5 nm. Although $t = 2$ nm allows the coupling of the FM layers, as shown by the single switching in the hysteresis loop, $t = 3$ and 5 nm have independent switching. Given this set of samples, I managed to fabricate samples that have trilayer FM films with independent switching and to tune their coupling by the interlayer thickness keeping the growth of the FM layers epitaxial.

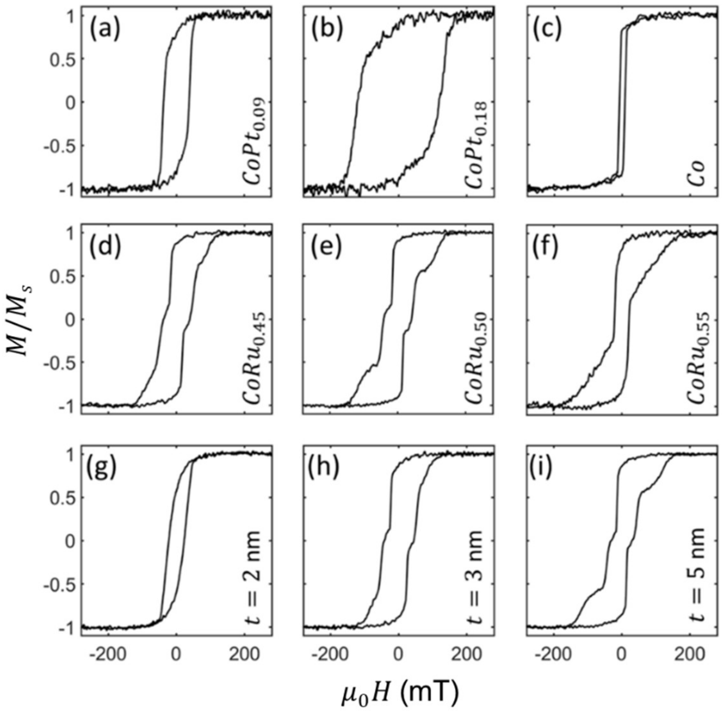

Reference samples

Different concentrations of Ru in the Co-Ru interlayer with $t = 4$ nm

An interlayer alloy of $CoRu_{0.50}$ with different interlayer thicknesses t

Figure 5.5 Experimentally determined VSM hysteresis loops for the three reference samples (a,b,c), for the multilayer structure having different concentrations of Ru in the Co-Ru alloy interlayer with a thickness $t = 4$ nm (d,e,f) and for an interlayer alloy of $CoRu_{0.50}$ with different interlayer thickness t (g,h,i). All $M/M_S(H)$ hysteresis loops correspond to a sample orientation of $\varphi_0 = 15$ deg.

5.3 Results and discussion

In my experimental system, the magnetization is designed to remain in the sample plane, as the GME set up utilized is the one shown in Fig 4.3(a). Deviations from the pure in-plane orientation that one could expect would be due to field misalignment. Initial test measurements confirmed that the polar MOKE is indeed very small and thus our analysis focuses on the in-plane MOKE parameters, $\tilde{\alpha}$ and $\tilde{\beta}$. As these parameters are complex quantities, they can be expressed as:

$$\tilde{\alpha} = |\tilde{\alpha}|e^{i\phi_{\tilde{\alpha}}}, \tag{5.1}$$

$$\tilde{\beta} = |\tilde{\beta}|e^{i\phi_{\tilde{\beta}}}, \tag{5.2}$$

where $\phi_{\tilde{\alpha}}, \phi_{\tilde{\beta}}$ are the phases of $\tilde{\alpha}$ and $\tilde{\beta}$. For a single FM layer exhibiting macrospin behavior, one can furthermore relate $\tilde{\alpha}$ and $\tilde{\beta}$ with the magnetization orientation angle φ_m as

$$\tilde{\alpha} = \tilde{\alpha}_0 \cdot \cos\varphi_m, \tag{5.3}$$

$$\tilde{\beta} = \tilde{\beta}_0 \cdot \sin\varphi_m, \tag{5.4}$$

for which $\tilde{\alpha}_0$ and $\tilde{\beta}_0$ are complex constants that are independent from the magnetization angle φ_m, which is defined with respect to the applied field direction (see Fig 2.2). Given that $\sin\varphi_m$ and $\cos\varphi_m$ are real numbers, Eqs. (5.3) and (5.4) now imply that phases $\phi_{\tilde{\alpha}}, \phi_{\tilde{\beta}}$ should not depend on the angle of the magnetization vector φ_m, as was already shown in Chapter 4 [4].

In the case of a magnetic multilayer thin film sample containing several FM layers, one has to take into account the individual contributions from each of the FM layers. Under the assumption of single layer superposition, the $\tilde{\alpha}$ and $\tilde{\beta}$ coefficients can be expressed as a linear combination of the coefficients associated with each of the FM layers, each of which having its own magnetization vector orientation φ_{m_1} and φ_{m_2} [13]. Considering the two FM layer case as an example of a general system with "L" FM layers, $\tilde{\alpha}$ and $\tilde{\beta}$ can be written as

$$\tilde{\alpha} = \tilde{\alpha}_1 \cos\varphi_{m_1} + \tilde{\alpha}_2 \cos\varphi_{m_2}, \tag{5.5}$$

$$\tilde{\beta} = \tilde{\beta}_1 \sin\varphi_{m_1} + \tilde{\beta}_2 \sin\varphi_{m_2}, \tag{5.6}$$

where $\tilde{\alpha}_i$ and $\tilde{\beta}_i$ incorporate the multi reflection optics of a multilayer sample. The only approximation is that the magneto-optical effect of one layer does not impact the magneto-optics of the other. So, optical layer-layer interference is included in this picture, but MOKE-MOKE interference is not, a distinction that will be discussed in the next section.

In the specific case that the two FM layers exhibit magnetic collinear behavior, the angle of the magnetization vector is the same for the two FM layers and $\tilde{\alpha}$ and $\tilde{\beta}$ can be expressed as

$$\tilde{\alpha} = (\tilde{\alpha}_1 + \tilde{\alpha}_2) \cos \varphi_m \, , \tag{5.7}$$

$$\tilde{\beta} = \left(\tilde{\beta}_1 + \tilde{\beta}_2\right) \sin \varphi_m, \tag{5.8}$$

which implies constant MO phases $\phi_{\tilde{\alpha}}, \phi_{\tilde{\beta}}$, in the exact same way as when having one FM layer only.

On the other hand, if the two FM layers are sufficiently decoupled, a field induced non-collinearity can occur that also exhibits a relevant field strength dependence, starting from being aligned at zero field along the EA to having different field orientations under field conditions, given that the magnetization vector of each layer rotates differently, as displayed in Fig. 5.1(b). In this case, the angles of magnetization vary differently with field, resulting in $\varphi_{m_1} \neq \varphi_{m_2}$. From Eqs. (5.5) and (5.6) one can observe that in this case the phases $\phi_{\tilde{\alpha}}, \phi_{\tilde{\beta}}$ do not have to remain constant [1], which in turn allows for a rigorous test and the detection of non-collinear state evolutions in magnetic multilayers. I will make use of this very fact to detect and study the occurrence of non-collinear magnetization states in our multilayer samples.

Moreover, the real and imaginary part of $\tilde{\alpha}$ and $\tilde{\beta}$, that are obtained from Eq. (5.5) and (5.6), represent two signal sums of the two layers, to which both layers contribute with a different weight, meaning that they represent different averaging procedures, and therefore these data might allow in principle for a disentanglement or separation of the individual layer contributions.

5.3.1 Verification of layer superposition assumption

A central assumption of the above data analysis and interpretation is the assumption that the total MO response of a multilayer can be interpreted as a linear superposition of the MO contributions from the individual magnetic layers, as was done in Eq (5.5) and (5.6). This assumption is critical for detecting non-collinear magnetic behavior and will also be needed for the layer-resolved vector magnetometry analysis. However, the superposition assumption is an approximation and to make practical use of it, it has to be numerically very precise. Therefore, here I verify that this approximation is indeed very precise and deviations from it will not impact the data analysis, given that they are substantially smaller than experimental noise.

---

[1] if the $\tilde{\alpha}_i$ and $\tilde{\beta}_i$ of the individual layers have different phase angles, which one would generally presume to be the case.

The superposition assumption is not exact, though, and thus, it will have an error associated with it. However, this error should be of quadratic order in the MO effects, given that the effective optical index of refraction is changed quadratically by the existence of linear MO effects, and correspondingly defines the impact that different magnetic states in different layers should have onto each other. So, to test if a methodology that is based on the linear superposition assumption can produce quantitatively meaningful results, one needs to know what the level of deviation from an exact solution is. I will continue with the consideration of the two FM layer case as an example of a general system with "L" FM layers throughout this section.

As already described, our samples are multilayer stacks composed of two FM layers that are separated by a NM layer. The exact size of MO effects in such multilayer stacks can be obtained in a numerically precise way by means of the 4x4 transfer matrix method [14–16]. Therefore, I calculated the MO signal of our sample type by means of the 4x4 transfer matrix method in two ways. First, I performed the calculation in the numerical exact way, by reproducing each layer of the sample. In a second calculation, I then mimicked the superposition approach, calculating the individual layer responses, assuming each time that only one of the FM layers is actually magneto-optically active, and then add up the two single layer contributions to compare the sum to the exact result.

Moreover, the collinear and non-collinear behavior were also modelled by means of the angular rotation of the two magnetization vectors, which depend on the strength of the applied field, as illustrated in Figs. 5.6(a) and (d), mimicking the hard axis (HA) behavior. In Fig. 5.6(a) the two layers rotate in a quantitatively identical way, as it would happen in a collinear magnetization scenario, and in Fig. 5.6(d), each layer magnetization rotation is different. Additionally, in Fig. 5.6(d) the mean magnetization rotation $\langle\varphi_m\rangle$ is included, given that I am using this quantity to define the x-axis in the main plots of Fig. 5.6. Accordingly, a high $\langle\varphi_m\rangle$ value is equivalent to the case in which the magnetization is near the EA ($H \rightarrow 0$), while for small $\langle\varphi_m\rangle$ angles, the magnetization is near the applied magnetic field orientation ($H \rightarrow H_s$).

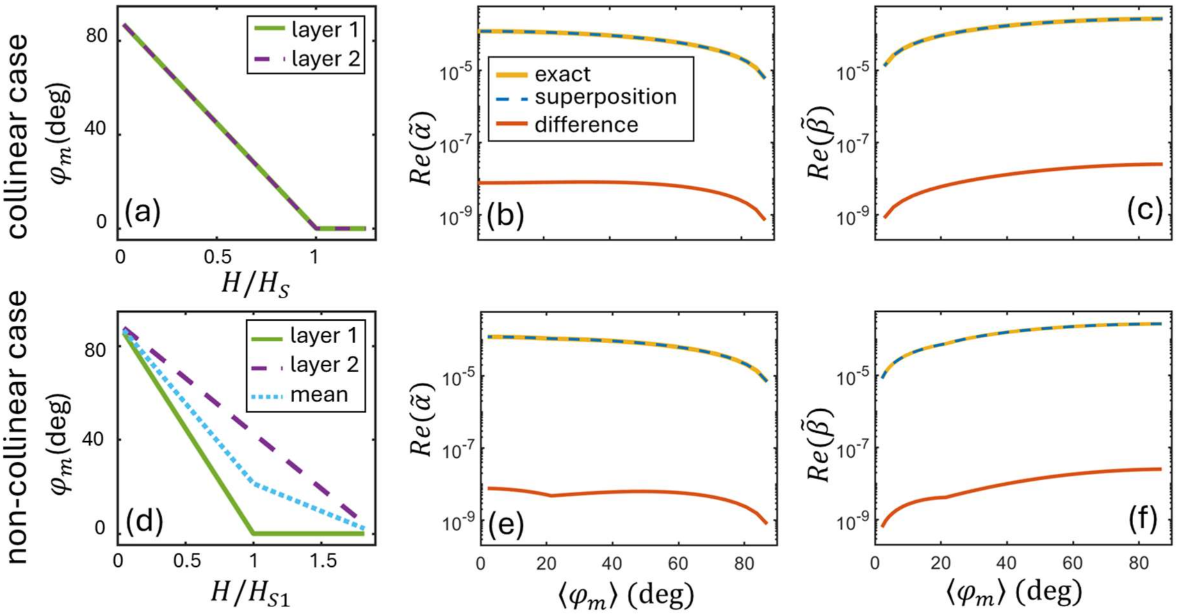

Figure 5.6 Numerical results of the exact optical multilayer simulation of the MOKE signal in comparison to the layer superposition approximation described in Eqs. (5.5) and (5.6) and the difference between these two calculations for collinear (first row) and non-collinear (second row) magnetic behavior. Specifically, the figures show the presumed rotation of the magnetization vectors in a FM bilayer sample with respect to the applied magnetic field strength H for the case of a HA sample orientation for (a) the collinear case and (d) the non-collinear case. Also, it is shown, on logarithmic scale, the real part of $\tilde{\alpha}$ (b, e) and the real part of $\tilde{\beta}$ (c, f) for a FM bilayer sample as a function of the mean orientation angle $\langle\varphi_m\rangle$ of the magnetization vectors, respectively.

Based upon this assumed field dependence mimicking the HA behavior, I display our computation results, including the exact calculation, the superposition approach and the difference between them, as a function of the average magnetization orientation in Fig. 5.6(b,c) and (e,f). Figures 5.6(b) and (e) represent the results obtained for $Re(\tilde{\alpha})$ in the collinear and the non-collinear case, respectively, while Figs. 5.6(c) and (f) show the corresponding data for $Re(\tilde{\beta})$. The first thing that one notices in these plots is the rotation of the magnetization, given that for small $\langle\varphi_m\rangle$ angles, $Re(\tilde{\alpha})$ has relatively high values, while $Re(\tilde{\beta})$ is comparatively small, which indicates that the magnetization is mostly aligned with the applied field orientation. As $\langle\varphi_m\rangle$ values increase, $Re(\tilde{\alpha})$ gets smaller and $Re(\tilde{\beta})$ gets accordingly larger, so that for $\langle\varphi_m\rangle$ angles near 90 deg, the signal is coming from a magnetization that is nearly aligned with the EA orientation along the transverse direction. The second, and most relevant aspect that one can see in Fig. 5.6, is the fact that the deviations in between the superposition approach and exact solutions are extremely small, namely four orders of magnitude smaller than the actual values. I calculated all the different magnetization orientations and collinear and non-collinear scenarios in order to properly analyze the error of the superposition approach, which is consistently found to be extremely small under all these conditions for any of the resulting magnetic states. The corresponding calculations for $Im(\tilde{\alpha})$ and $Im(\tilde{\beta})$ show identical behavior. This finding is in full agreement with previous studies that have identified a depth-dependent additivity of complex MO signals [13,17,18]. Therefore, in the analysis and interpretation of our experimental results, I can confidently justify the assumption that the MO results of our multilayer stacks can be numerically analyzed as the sum of the corresponding MO signals of two individual FM layers according to Eqs. (5.5) and (5.6).

5.3.2 Detection of non-collinear magnetization states in two FM layer systems

To experimentally validate the methodology, I performed GME measurements for the set of samples with two FM layers with interlayer thickness of $t = 0.5$ to 6 nm under a field orientation of $\varphi_0 = 65$ deg. As an example for the experimental GME results that I compiled, the complete extracted information of the $t = 5$ nm sample is shown in Fig. 5.7, where data for the in-plane hysteresis loop are represented in Fig. 5.7(a)-(e). Specifically, Fig. 5.7(a) and (b) show the real and imaginary values of the MO parameter $\tilde{\alpha}$ as a function of the applied field H, and Figs. 5.7(c) and (d), the corresponding real and imaginary parts of $\tilde{\beta}$.

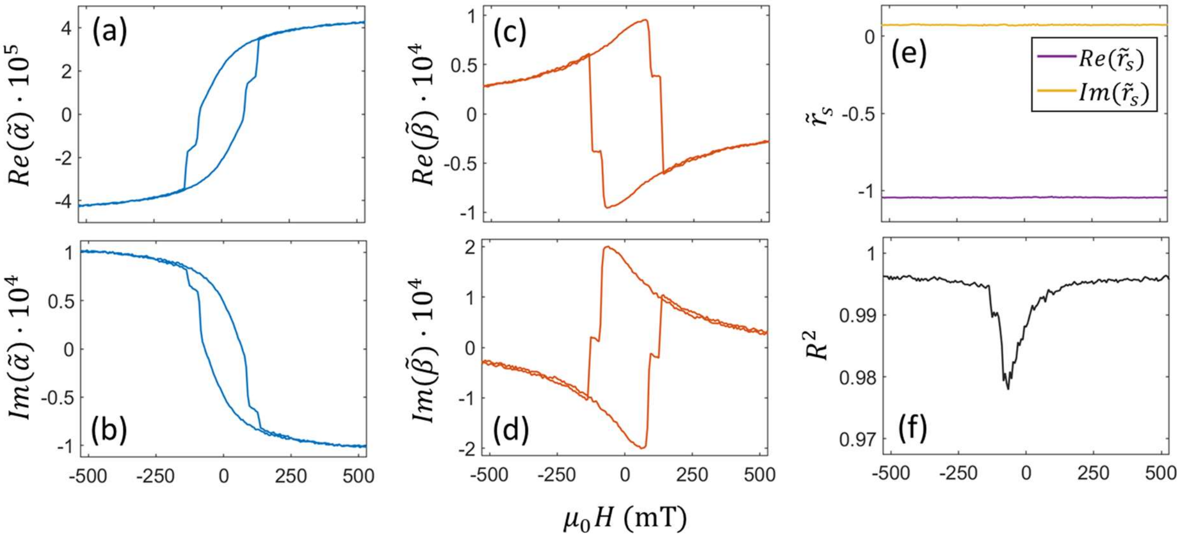

Figure 5.7 Experimental in-plane hysteresis loop data for the multilayer sample with $t = 5$ nm for a sample orientation of $\varphi_0 = 65$ deg, with (a), (b) displaying the real and imaginary parts of $\tilde{\alpha}$ vs. the applied field strength H, and (c), (d) showing the simultaneously measured real and imaginary parts of $\tilde{\beta}$ vs. H; (e) displays the experimentally determined Fresnel coefficient $\tilde{r}_S$ of this sample vs. H and (f) shows the associated field dependent R^2 values of the least-squares fits to our GME data sets, from which the parameters in (a)–(e) are extracted.

For this specific interlayer thickness, one can observe a double step reversal process, which is due to the different coercive field values of Co and Co-Pt thin layers and an absent or weak FM interlayer coupling in between these two FM layers. This double step is therefore related to the seemingly independent switching of the two FM layers. Co exhibits lower anisotropy values than Co-Pt and accordingly lower H_c and therefore, the first step coming from high field saturation corresponds to the inversion of the magnetization of the Co layer. The Co-Pt alloy layer has a higher H_c, which means that the second step of the hysteresis loop is related to the inversion of this second layer. Moreover, the MO coefficients represented in Figs. 5.7(a)-(d) show a continuous variation with field in addition to the abrupt magnetization reversal steps, which is associated with the rotation of the magnetization vector. The sample exhibits a magnetization rotation in both layers, starting along the EA orientation when no magnetic field is applied, towards an alignment with the magnetic field orientation as its strength increases. This translates to having a transition from mostly transverse to mostly longitudinal MO signal as H increases, which is exactly what one can see in Figs. 5.7(a)-(d) where the values of the real and imaginary part of $\tilde{\beta}$ decrease from a maximum near $H = 0$ as one applies higher H values, while the reverse occurs for $\tilde{\alpha}$.

Moreover, the real and imaginary parts of the MO signals shown in Fig. 5.7 are fairly similar as one would normally expect, but they also display relevant differences from each other. For example, it can be seen that the step heights of the two inversion processes are different in the real and imaginary contributions of $\tilde{\alpha}$ and $\tilde{\beta}$. This means real and imaginary parts do not provide simply the same information, but provide distinctively different information, which is formally encapsulated in Eqs. (5.5) and (5.6). It is this difference in information contained in the real and imaginary parts for each of the MO signal components what enables us to separate the layer contributions of each vector component and detect the existence of non-collinear magnetic behavior. Therefore, the complete data set shown in Fig. 5.7 will allow for the robust detection of non-collinearity in our samples, as will be discussed in the following.

Additionally, Fig. 5.7(e) shows the real and imaginary parts of the pure optical parameter $\tilde{r}_s$ as a function of the applied external field H. As pure optical parameters, they should not depend on H and instead remain constant for any H value, as indeed they do. From the field dependence of R^2 represented in Fig. 5.7(f) one can see that our $\Delta I/I$ experimental data are very precisely reproduced by the fit to the $\Delta I/I(\theta_1, \theta_2)$ theoretical description given by Eq (3.11) everywhere, as the R^2 values are better than 0.98 virtually in the entire field range. The R^2 values are at their lowest in the immediate vicinity of the coercive field, where the magnetization switching of the layers progresses via laterally non-homogeneous magnetic states by forming magnetic domains, so that the MO signal becomes rather small and thus relatively noisy. For this reason, I am going to focus our further analysis only on results, in which each layer is in a laterally uniform state by utilizing only positive field value data for the decreasing field branch of the hysteresis loop. In this parameter range, one can be assured by fundamental energy considerations that the magnetization state is in its stable energy minimum and thus, no meta-stable domain formation occurs.

As previously documented in this section, a mere magnetization rotation does not change the phase factors of the various MO elements of the reflection matrix if the rotation happens to be collinear throughout the rotation process. However, if the magnetization state does not fulfill this condition and non-collinear alignments occur upon field application, the MO coefficient phases can actually change. Therefore, we are going to observe the field evolution of the experimental MO coefficient phases in different samples and compare them to the single FM layer samples that were grown as references. The experimentally determined values of these phases are represented in Fig. 5.8. Specifically, in Figs. 5.8(a)–(f) I plot $\phi_{\tilde{\beta}}$ vs $\phi_{\tilde{\alpha}}$ for different NM interlayer thickness values and for the stable hysteresis loop regime highlighted in Fig. 5.8(g). Figure 5.8(a) also includes results for the two single layer reference samples.

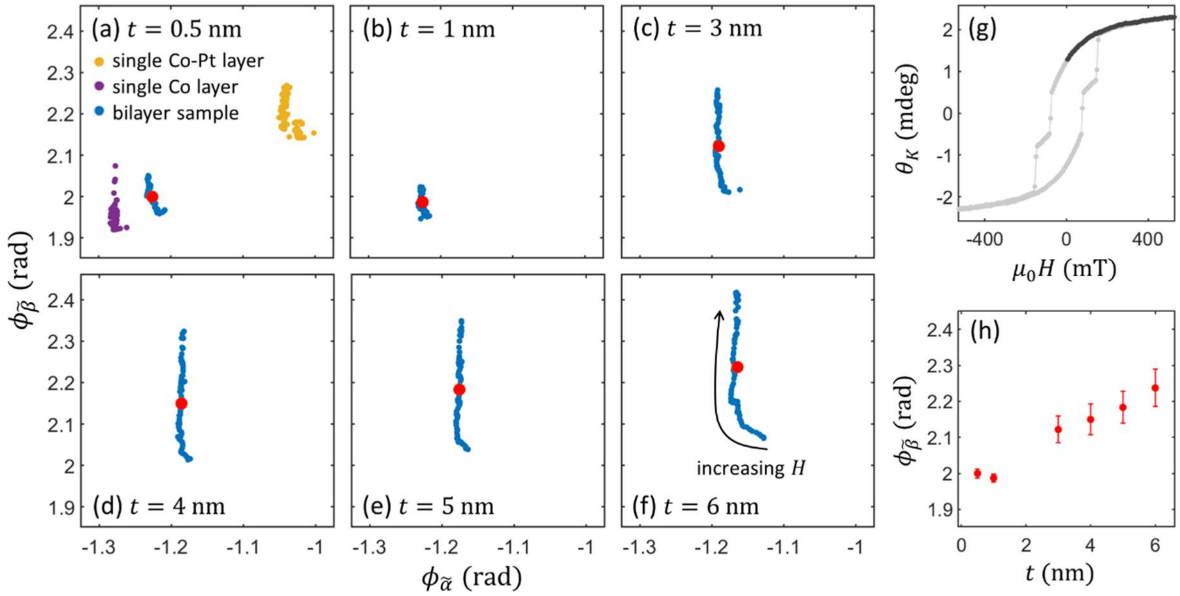

Figure 5.8 From (a) to (f), experimentally determined $\phi_{\tilde{\beta}}$ vs. $\phi_{\tilde{\alpha}}$ values for all magnetic field H values in the thermodynamically stable regime, measured for several samples with different interlayer thicknesses, from $t = 0.5$ nm to $t = 6$ nm; the respective t values are displayed in each subfigure. The red point in each subfigure indicates the mean value. (a) also includes for comparison the results for the two single FM layer reference samples and (f) includes an arrow indicating the increasing H direction with which the quantities evolve as a guide to the eye. (g) Exemplary hysteresis loop highlighting the stable magnetization regime with a darker color, utilized for the data shown in (a)–(f), measured for the case of the $t = 6$ nm sample. (h) Displays the mean values of $\phi_{\tilde{\beta}}$ as a function of the interlayer thickness t; the error bars are the associated standard deviations of the mean.

Figure 5.8(a) shows the thinnest interlayer thickness data (in blue), for which very strong coupling is expected and thus a collinear rotation of the magnetization for both FM layers. Indeed, we observe that $\phi_{\tilde{\alpha}}$ and $\phi_{\tilde{\beta}}$ change only minimally throughout the entire field sequence, even if they do not collapse onto exactly one point. However, they nonetheless seem to indicate a collinear magnetization rotation, given that the individual layer samples show very comparable small spreads of $\phi_{\tilde{\alpha}}$ and $\phi_{\tilde{\beta}}$ in the same applied field range. The small variations in these single layers and the strongly coupled bilayer film shown in Fig. 5.8(a) are likely to be caused by small MO anisotropy effects [12]. As we have already seen in Chapter 4, for these types of in-plane uniaxial film samples under chosen applied field direction away from the HA ($\varphi_0 = 65$ deg), relevant levels of MO anisotropy effect are expected, leading to a partial mixture of longitudinal and transverse MO effects. In Fig. 5.8(b), it can be seen that the $t = 1$ nm sample shows a very similar behavior to the one observed in Fig. 5.8(a) given that the FM interlayer coupling is expected to be very strong still for this sample, leading to collinear magnetization rotation throughout the field cycle.

As a counter example, I represent in Fig. 5.8(f) the results for the $t = 6$ nm interlayer sample, for which weak or no FM coupling is expected and thus a non-collinear rotation of the individual layer magnetizations with applied field. Indeed, we observe a very substantial variation of $\phi_{\tilde{\alpha}}$ and $\phi_{\tilde{\beta}}$ with changing field strength, that is far larger than for the strongly coupled bilayer samples or the single FM films, and thus consistent with the occurrence of non-collinear magnetization states. Thus, the expected non-collinear magnetization trajectory does indeed lead to very large phase modifications of the MO quantities $\tilde{\alpha}$ and $\tilde{\beta}$. The specific phase trajectory for the $t = 6$ nm sample consists of an initial shift of $\phi_{\tilde{\alpha}}$ as H starts increasing and a subsequent and even larger change in $\phi_{\tilde{\beta}}$ for large H values. At low magnetic fields, $\tilde{\alpha}$ is relatively small, given that the magnetization will lie along the EA, which is oriented at $\varphi_0 = 65$ deg, so that the relative change in the phase of $\tilde{\alpha}$ is bigger and a significant shift towards smaller $\phi_{\tilde{\alpha}}$ values can be observed. As the field H increases, the magnetization vectors rotate, $\tilde{\alpha}$ gets bigger and $\tilde{\beta}$ smaller, so that for high field values the relative change in the phase of $\tilde{\beta}$ becomes the dominant effect, leading to very high $\phi_{\tilde{\beta}}$ values. In turn, this means that following $\phi_{\tilde{\alpha}}$ and $\phi_{\tilde{\beta}}$ in our MO measurements indeed allows for the detection of non-collinear magnetic states in magnetic multilayers and enables a quantitative observation of their field evolution, which was the first step of our study here.

Figures 5.8(c)-(e) represent intermediate cases, for which the NM interlayer thickness t is 3, 4 and 5 nm, respectively. The MO measurements clearly exhibit intermediate levels of phase changes as a function of the field strength and thus constitute non-collinear behavior as well, even if to a slightly smaller degree. In Fig. 5.3(d), I had represented the hysteresis loop corresponding to the NM interlayer thickness sample of $t = 4$ nm, for which no double jump was observed, but in Fig. 5.8(d) a clear phase trajectory is visible. Thus, even if the exchange coupling is sufficiently strong to synchronize the switching during the magnetization reversal process, it does not necessarily mean that the magnetization is collinear throughout the entire reversal sequence, as our data clearly demonstrates.

Also, for the entire interlayer thickness series, one can observe that the absolute position of the phases changes from sample to sample, given that changing t modifies the multilayer optics, even if only very slightly. The resulting position shift with t can be better observed by looking at the measurement averaged phase values represented as red points in the different subfigures of Fig. 5.8(a)–(f). Additionally, the interlayer thickness evolution of the averaged $\phi_{\tilde{\beta}}$ values is explicitly shown in Fig. 5.8(h), with the error bars representing the associated standard deviation of the mean for all measurements performed on the same sample. This shift is rather modest and, it is an expected purely optical effect that comes from the different optical interference conditions due to the different interlayer thickness t in different samples. It has no impact on the magnetic state-induced evolution of the MO phases.

5.3.3 Layer-resolved vector magnetometry in multilayers with two FM layers

To continue with the next step and achieve layer-resolved vector magnetometry in multilayers with two FM layers, I will focus on the samples that show double-step magnetization reversals as these samples really exhibit a large range of relative magnetization orientations and thus present a very suitable test case to explore the wide applicability of the method in terms of the magnetization states covered. Figure 5.9 shows the results of our GME measurements for the sample with $t = 8$ nm and $\varphi_0 = 75$ deg, in a similar way as it was shown in Fig 5.7 for the sample with $t = 5$ nm and $\varphi_0 = 65$ deg. Specifically, Figs. 5.9 (a) and (b) show the real and imaginary values of the longitudinal MOKE parameter $\tilde{\alpha}$ as a function of H and Figs. 5.9 (c) and (d) the corresponding parts of the transverse MOKE parameter $\tilde{\beta}$ [2]. Also, in comparison with the detection of non-collinear magnetic states, here I increased the angle φ_0 from 65 to 75 deg so that the angular amplitude of the rotation of the magnetization vectors is even wider.

In Figs. 5.9(a)–(d) we see a double-step reversal process, related to the two FM layers switching independently, as two decoupled FM layers with different anisotropy will exhibit magnetization reversal at different fields [19]. Other variations of the MOKE coefficients are

---

[2] The polar MOKE parameter $\tilde{\gamma}$ was also analyzed but was found to be very small in the entire field range and therefore I limited the discussion to a two-dimensional magnetization vector in the subsequent numerical analysis, as was done in the detection of non-collinear magnetic states.

associated with the expected magnetization vector rotations: magnetization is aligned with the EA (large transverse $\tilde{\beta}$ values) when $H = 0$ and changes toward the direction of the applied field for large H values (large longitudinal $\tilde{\alpha}$ values, given that the magnetic field is aligned with the x-direction). The MOKE signals in Fig. 5.9 are fairly similar to each other as one would normally expect, but they also display relevant differences. One obvious difference is the step height at the two magnetization switching processes in the real and imaginary parts of $\tilde{\beta}$, in Figs. 5.9(c) and (d), for instance. This is a crucial aspect of our measurements because it demonstrates that the real and imaginary parts of the MOKE coefficients in $\boldsymbol{R}$ do not simply provide the same information but exhibit distinctive differences enabling us to later separate the magnetization vector contributions of both layers.

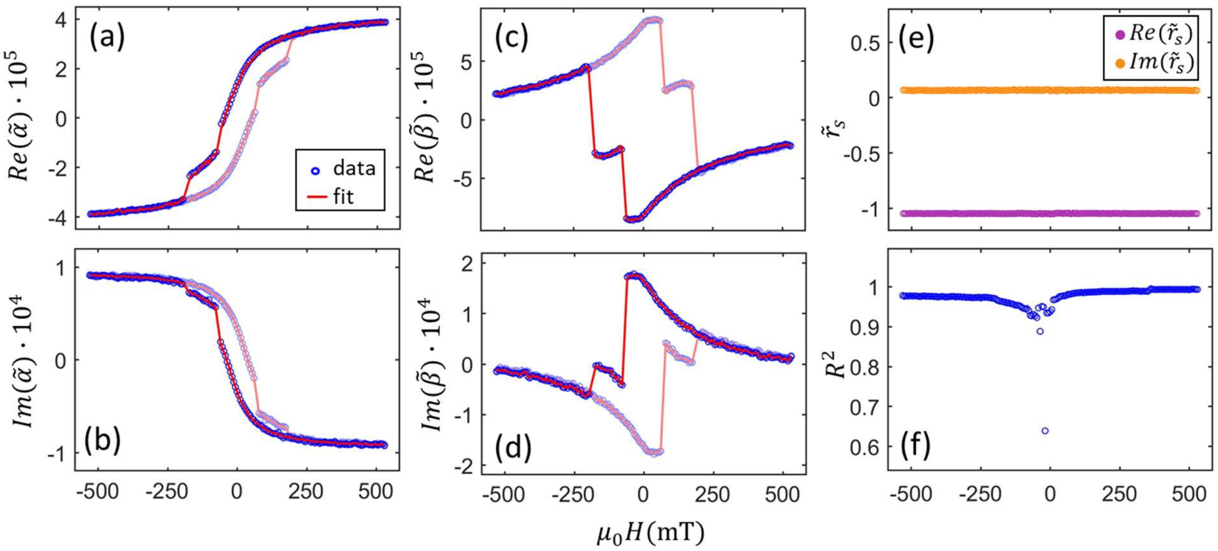

Figure 5.9 Reflection matrix values experimentally obtained for the $t = 8$ *nm sample and orientation* $\varphi_0 = 75$ *deg, with (a) and (b) displaying the real and imaginary parts of* $\tilde{\alpha}$ *and (c) and (d) those of* $\tilde{\beta}$ *vs. the applied field* H*. The red lines in (a)–(d) represent the results of the least squares fit of Eqs. (5.5) and (5.6) to the GME data. (e) displays the experimentally determined Fresnel coefficient* $\tilde{r}_s$ *vs H and (f) the associated field-dependent* R^2 *values of the least squares fits, from which the parameters in (a)–(e) are extracted. The* R^2 *values are only displayed for the field decreasing hysteresis loop branch.*

For completeness, the purely optical parameters of $\boldsymbol{R}$ are represented in Fig. 5.9(e) and, as expected, they are independent of H because they are independent of the magnetization state. The excellent R^2 values of our individual GME data fits at every H value are shown in Fig. 5.9(f) and confirm the precision of the GME methodology. The smaller R^2 values between zero and the switching field are due to the nearly vanishing MOKE signals in partially compensated domain states.

Having $\tilde{\alpha}(H)$ and $\tilde{\beta}(H)$ as a function of the applied field H means that the data in Figs. 5.9(a-d) contain $4N$ independent data points, with N being the number of measured H values. Accordingly, if we go back to Eqs (5.5) and (5.6), the mathematical identification problem is overdetermined, having 2 angles $\varphi_{\mathrm{m}_1}(H)$ and $\varphi_{\mathrm{m}_2}(H)$ for each field value and 4 complex or 8 real prefactors $\tilde{\alpha}_i$ and $\tilde{\beta}_i$ that are independent from the field, which in sum are $2N + 8$ values to be determined. Thus, I can perform a least-squares fit of $\varphi_{\mathrm{m}_1}(H)$ and $\varphi_{\mathrm{m}_2}(H)$ and $\tilde{\alpha}_1$, $\tilde{\alpha}_2$, $\tilde{\beta}_1$ and $\tilde{\beta}_2$ to the measured data set in Figs. 5.9 (a–d). The so-obtained fits of $\tilde{\alpha}(H)$ and $\tilde{\beta}(H)$ to Eqs. (5.5) and (5.6) reproduce these data with high accuracy, as shown by the red lines in Figs. 5.8(a–d), which represent the fit for the $t = 8$ nm sample. Hereby, $\tilde{\alpha}(H)$ and $\tilde{\beta}(H)$ in Eqs. (5.5) and (5.6) represent independent linear equations, which means that real and imaginary parts add up the individual layer signals in different proportions. This is the case for our samples, given that $\tilde{\alpha}(H)$ and $\tilde{\beta}(H)$ have small but significant differences, as already mentioned above. Exactly at the switching fields, however, there are nonuniform magnetization states, for which my present analysis is not applicable and thus no magnetization angles are determined in their immediate vicinity [3].

I measured samples with four different thicknesses t and their results for the decreasing field branch of the hysteresis loops are included in Fig. 5.10. Figure 5.10(a) contains the magnetization angles for the sample with $t = 8$ nm, representing an interlayer thickness that is sufficiently large to completely decouple the two FM layers. For $H = 0,$ I find φ_{m_1} and φ_{m_2} to be the same. This is a result that is fully consistent with the expected behavior of the designed sample, given that both films have the same EA orientation, and thus the magnetization vectors naturally align even without coupling. As H is increased, the Co layer rotates more strongly and in near saturation, φ_{m_1} achieves values close to zero, as this layer is magnetically softer than the Co-Pt layer [20,21]. The Co-Pt magnetization also rotates upon applying an increased field strength, but it does not reach saturation with the field values available in our experiment. The results also exhibit the expected behavior regarding the magnetization switching at each layer's coercive field, which requires larger reverse H values for the Co-Pt layer than for the Co layer.

---

[3] Ten number of points are not considered, compared to the total field value number of 241 utilized.

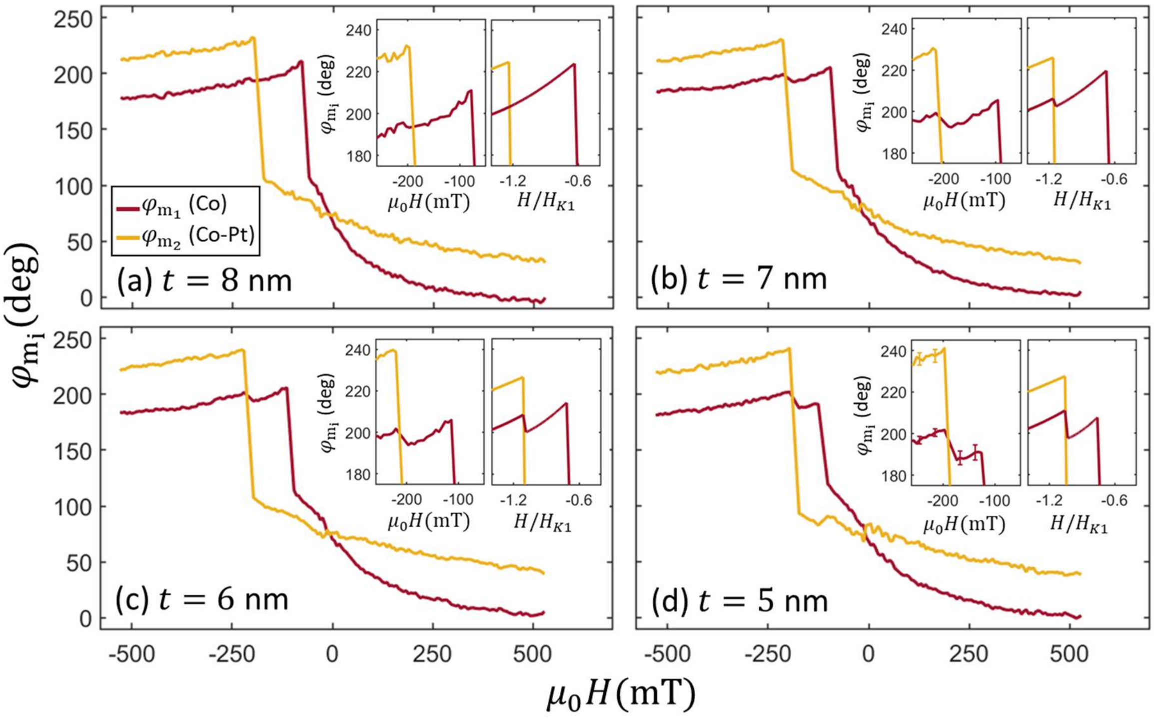

Figure 5.10 Magnetization vector orientations φ_{m_1} *and* φ_{m_2} *vs* H *for the decreasing field hysteresis loop branch. The dark red lines represent the Co layer magnetization angle and the yellow line the corresponding angle of the Co-Pt layer. From (a) to (d), the results correspond to samples with NM interlayer thickness* t *of* 8, 7, 6, *and* 5 *nm, respectively, with the same nominal EA orientation* $\varphi_0 = 75$ *deg. Insets in the top right corner of each subfigure are included, with two representations. The first ones are a zoomed-in view to better observe the details of the Co layer magnetization angle and the coercive field values with the inset in (d) having illustrative error bars representing the 95% confidence intervals of our fitting procedure. The second representation included on the insets of all sub-figures are model calculations for two macrospins exhibiting different anisotropy constants and a FM coupling strength that increases from (a) to (d), with* H *normalized to the anisotropy field* H_{K1}.

The results for samples with $t = 7, 6$ and 5 nm are shown in Figs. 5.10(b-d). We observe here a similar behavior to the one shown by the sample with $t = 8$ nm, namely that the Co layer saturates for high field values while the Co-Pt layer does not. We also see again that the magnetization switch of the Co layer happens before that of the Co-Pt layer. Moreover, there are two additional effects to notice here, best visible for $t = 5$ nm sample, shown in Fig. 5.8(d): the coercive fields of each of the two FM layers are more similar to each other if compared to the thicker $t = 8$ nm sample of Fig. 5.10(a); also one can see that the Co layer magnetization angle shifts by a few degrees at the very field value at which the Co-Pt layer inverts. These effects are better observed by looking at the zoom-in of the angle vs. field data displayed in the left insets of Figs. 5.10(a-d), with the one of Fig. 5.10(d) displaying representative error bars. The progression of the coercive fields with thickness t indicates that a noticeable FM interlayer exchange coupling occurs upon decreasing t. For $t < 5$ nm, this FM interlayer coupling becomes strong enough, so that the double step switching is not observed. Additionally, as the Co-Pt switches, the local free energy minimum of the Co layer changes slightly, if there is a FM coupling between both layers. This induces the small, but abrupt rotation of the Co layer at this field, even if it is not inverting its magnetization at this point. Therefore, I can detect the magnetization reversal impact of a modest FM interlayer exchange coupling for the sample with $t = 5$ nm. We also see the evolution of the FM interlayer coupling, starting from the uncoupled state for the $t = 8$ nm sample via intermediate thicknesses $t = 7$ and 6 nm in Figs. 5.10(b,c) towards the significant magnetization reversal modifications for the sample with $t = 5$ nm (Fig. 5.10(d)).

To verify this data interpretation, I have modelled the magnetization reversal behavior for a two macrospin model with aligned EA, different anisotropy constants and exhibiting different interlayer exchange coupling strengths J. A zoom-in of these model calculations are shown as the right insets in Figs. 5.10(a-d) with increasing J from (a) to (d), while keeping all other model parameters constant. As observed, these calculations confirm the key experimental features and associated explanations extremely well. In turn, this means that, while the observation of a magnetization orientation jump in the Co layer at the Co-Pt switching point seemed to imply a methodological limitation of isolating individual layer signals, it is instead an accurate observation of the exact physical behavior that the FM interlayer coupling generates in the Co layer. Correspondingly, these experimental results underscore the ability of the here-tested methodology to detect such fine details, just as true layer-resolved vector magnetometry should.

5.3.4 Extension to more than 2 layers: limits and perspectives of depth-resolved vector magnetometry

A natural next step in advancing layer-resolved vector magnetometry is its extension to multilayer systems with more than two FM layers. To explore this possibility, the fabricated FM trilayer samples were specifically engineered to exhibit three-step magnetization reversal processes. These samples contain three FM layers with differing magnetic anisotropies and interlayer coupling strengths tailored to ensure that each layer reverses at a distinct coercive field. This behavior is a necessary prerequisite for enabling independent tracking of each layer's magnetization vector.

From a theoretical standpoint, resolving the magnetization vectors of three (or more) independent FM layers should still be formally overdetermined. It would require increasing the number of independent data sets measured. While the two-layer case is solved using the real and imaginary parts of the two in-plane magneto-optical coefficients $\tilde{\alpha}$ and $\tilde{\beta}$, the addition of a third FM layer introduces N+4 values to be determined: the third magnetization angle φ_3 and its corresponding complex MO coefficients $\tilde{\alpha}_3$ and $\tilde{\beta}_3$. To solve this expanded system, an additional linearly independent data set is required.

This additional information can be obtained by performing GME measurements at a second wavelength. Since the MO coefficients depend on the optical constant N and the MO coupling constant Q of each layer of the sample and both N and Q depend on the wavelength, the real and imaginary parts of $\tilde{\alpha}$ and $\tilde{\beta}$ measured at two different wavelengths represent distinct linear combinations of the layer contributions. This multi-wavelength strategy would enable the mathematical overdetermination of the system and, in principle, allows for the extraction of the full vector magnetization profile across three FM layers.

The results from GME measurements of the sample with Co-Ru alloy interlayer with 50% of Ru and with a thickness $t = 4$ nm are included in Fig 5.11. The measurements were performed under a field orientation of $\varphi_0 = 15$ deg with the ultralow-noise 635 nm laser (a-f) and the tunable wavelength laser with $\lambda = 596$ nm (g-l). The in-plane hysteresis loops are represented in Fig. 5.11(a-e) and (g-j) for the two laser sources, where the real and imaginary values of the MO parameter $\tilde{\alpha}$ as a function of the applied field H are included in Figs. 5.11 (a,b) and (g,h), and Figs. 5.11(c,d) and (i,j), the corresponding real and imaginary parts of $\tilde{\beta}$. In a similar fashion as for the two FM layer samples, the reversal steps can be observed, which now are three, each one corresponding to one of the three independent FM layers of the sample. Now, the continuous variation with field associated with the rotation of the magnetization vector is smaller, because the field orientation angle is smaller in these measurements ($\varphi_0 = 15$ deg), as a compromise between seeing the three reversals clearly and achieving some degree of rotation of the magnetization vectors. Additionally, Fig. 5.11(e) and (k) show the real and imaginary parts of the pure optical parameter $\tilde{r}_s$ as a function of the applied external field H, remaining constant for all H values. From the field dependence of R^2 represented in Fig. 5.11(f) for the ultra-low noise 635 nm laser, one can see that our $\Delta I/I$ experimental data are very precisely reproduced by the fit to the $\Delta I/I(\theta_1, \theta_2)$ theoretical description given by Eq (3.11) everywhere, as the R^2 values are better than 0.98 virtually in the entire field range. In the case of the tunable wavelength laser with $\lambda = 596$ nm, the R^2 represented in Fig. 5.11(l) is not as good.

Indeed, the tunable wavelength laser source did not have sufficient stability and signal-to-noise ratio to produce a comparably good data set. Figure 5.12 shows the intensity stability of the ultra-low noise 635 nm laser and the tunable wavelength laser in comparison. As a result, the acquired data set lacked the precision and robustness required to reliably extract the magnetization angles of all three FM layers over the full field range.

Despite these limitations, the framework for depth-resolved vector magnetometry with three FM layers has been established. The experimental observations confirm the presence of independent magnetization switching events, and the theoretical requirements for full vector resolution are well-defined. Future efforts will focus on improving the optical setup to enable reliable multi-wavelength GME measurements. Additionally, complementary approaches such as angular-dependent GME could be explored to further increase the level of overdetermination by the data sets.

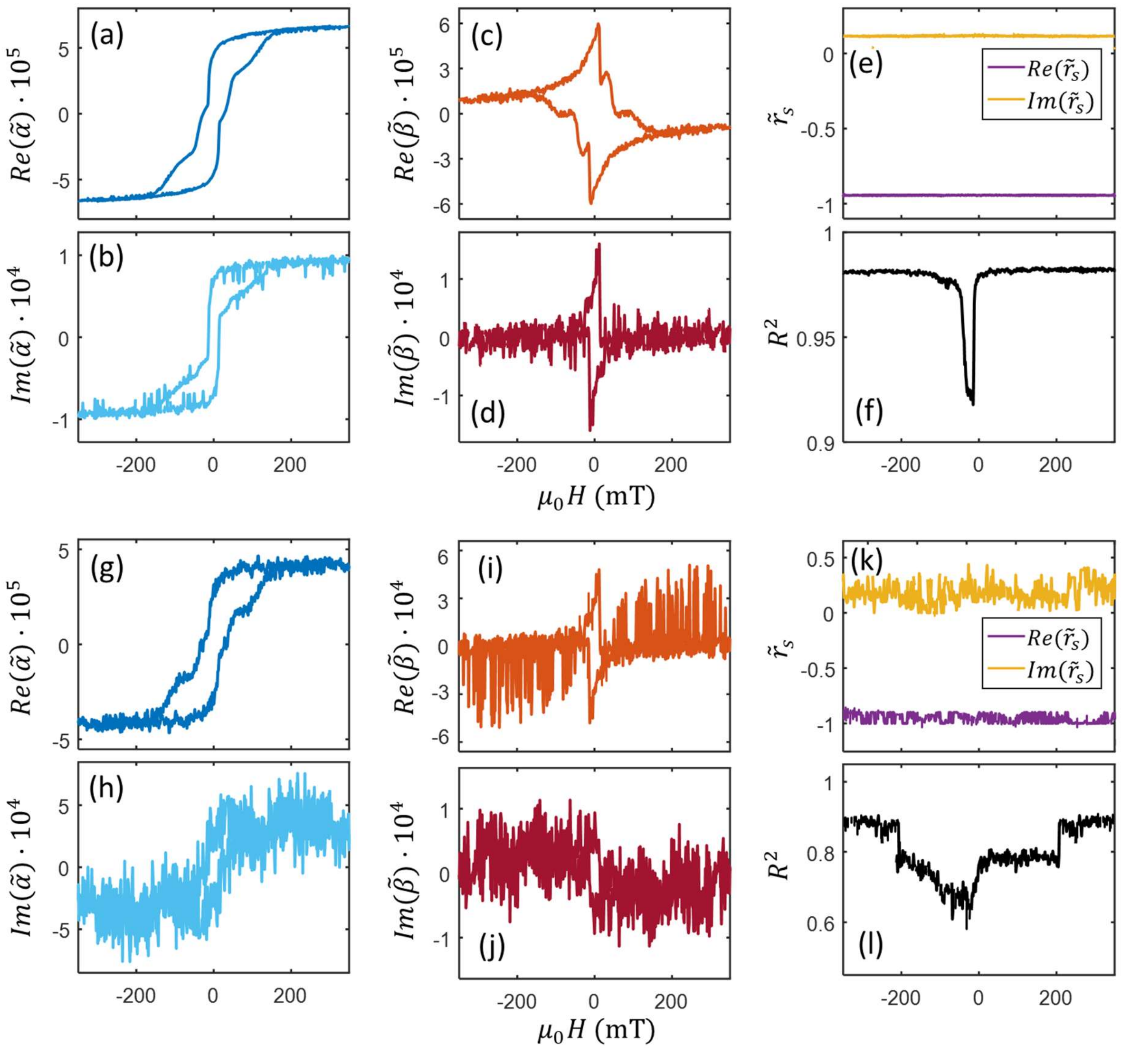

Figure 5.11 Experimental in-plane hysteresis loop data for the three FM layers sample with $CoRu_{0.5}$ *(*$t = 4$ *nm) alloy interlayer for a sample orientation of* $\varphi_0 = 15$ *deg, with (a-f) displaying the GME results for the ultra-low noise* 635 *laser and (g-l) the equivalent results for the tunable wavelength laser with* $\lambda = 596$ *nm.*

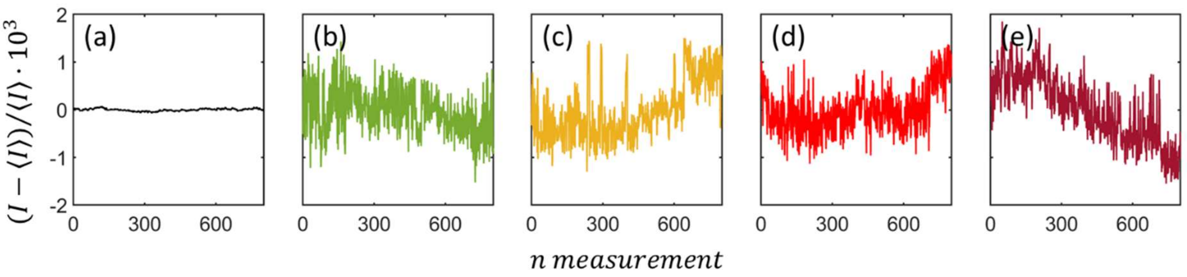

Figure 5.12 Intensity stability of the ultra-low noise $\lambda = 635$ *nm laser (a) in comparison with the tunable wavelength laser (b-e) for four different wavelengths (b)* 550 *nm, (c)* 596 *nm, (d)* 635 *nm and (e)* 675 *nm.*

5.4 Conclusions and outlook

In our study here, I accomplished the unambiguous detection of non-collinear magnetization states in $FM_1/NM/FM_2$ multilayers by measuring the complete set of field-dependent MO coefficients via GME. In order to demonstrate non-collinearity clearly, I grew a series of epitaxial samples with Co/Co–Ru/Co–Pt magnetic multilayers, which contained different Co–Ru thicknesses t in order to vary the FM interlayer exchange coupling strength between the two FM Co and Co–Pt layers. These samples were specifically designed to exhibit uniaxial magneto-crystalline anisotropy in both FM layers with aligned in-plane EA and macrospin behavior, which permitted us to rotate the magnetization vectors in both layers and accordingly induce collinear to non-collinear magnetization state transitions by varying the applied field strength. For the MOKE measurements, I utilize the GME characterization technique to precisely determine the full complex values of the MO coefficients of the reflection matrix as a function of the applied field strength H. In these measurements, one observes that the phase factors of the complex-valued MO coefficients for the in-plane magnetization components vary with field, which is a clear indication for the evolving non-collinear magnetization state with field strength in films that have sufficiently weak interlayer coupling strength, i.e. large t. This data interpretation is based on the assumption that the MO parameters in magnetic multilayers can be expressed as a sum of the individual MO parameters for each layer, which I tested numerically by means of simulations based on the transfer matrix method. Thus, I have successfully demonstrated the ability of MO measurements to detect non-collinear magnetization states in magnetic multilayers by monitoring the phase evolution of $\tilde{\alpha}$ and $\tilde{\beta}$ with applied field.

Moreover, I achieved layer-resolved vector magnetometry by means of MO measurements. Utilizing a suitable test set of FM/NM/FM multilayers, I demonstrated the ability of GME measurements to independently follow the magnetization angles of two different FM layers with in-plane macrospin behavior as a function of the applied field. This achievement is a significant step toward the long-term goal of characterizing the full depth dependence, in a layer-resolved way, of the magnetization vector in complex multilayer samples. A measurement and analysis scheme including the corresponding length variations of the magnetization vector is not necessarily beyond the capabilities of our general approach, but it is not demonstrated by our work here.

It should be feasible for a larger number of layers to be included in the analysis if the database is extended by other means, such as multiple angles of incidence or wavelengths. However, the full vectorial resolution for three FM layers was not achieved in the present work due to technical constraints, but the path towards multilayer vector magnetometry is clearly defined. With appropriate enhancements in measurement capability, GME can be extended to enable quantitative, depth-resolved analysis of increasingly complex magnetic multilayer systems.

To sum up, this chapter introduces and validates the GME methodology for the detection of non-collinear magnetic states and the achievement of layer-resolved vector magnetometry in multilayer systems. The approach is broadly applicable, experimentally accessible, and capable of yielding detailed magnetic information without destructive sample preparation or restrictive assumptions. It represents a significant advance in experimental magnetometry.

Chapter references

[1] A. Berger, E. E. Fullerton, O. Hellwig, B. Lengsfield, and E. E. Marinero, Patterned perpendicular magnetic recording medium with exchange coupled recording layer structure and magnetc recording systemusing the medium, United States Pat. US 8,021,769 B2 (2011).

[2] Z. R. Nunn, C. Abert, D. Suess, and E. Girt, Control of the noncollinear interlayer exchange coupling, Sci. Adv. **6**, eabd8861 (2020).

[3] Z. R. Nunn, J. Besler, P. Omelchenko, S. Koraltan, C. Abert, D. Suess, and E. Girt, Controlling the angle between magnetic moments of Co layers in Co|RuCo|Co, J. Appl. Phys. **133**, 123901 (2023).

[4] C. Martín Valderrama, M. Quintana, and A. Berger, Experimental verification of the reflection matrix description in linear magneto-optics, Phys. Rev. B **108**, 014415 (2023).

[5] O. Idigoras, U. Palomares, A. K. Suszka, L. Fallarino, and A. Berger, Magnetic properties of room temperature grown epitaxial Co 1-xRux-alloy films, Appl. Phys. Lett. **103**, 102410 (2013).

[6] W. Yand, D. N. Lamberth, and D. E. Laughlin, Unicrystal Co – alloy media on Si (110), J. Appl. Phys. **85**, 110 (1999).

[7] O. Idigoras, A. K. Suszka, P. Vavassori, B. Obry, B. Hillebrands, P. Landeros, and A. Berger, Magnetization reversal of in-plane uniaxial Co films and its dependence on epitaxial alignment, J. Appl. Phys. **115**, 083912 (2014).

[8] L. Fallarino, P. Riego, B. J. Kirby, C. W. Miller, and A. Berger, Modulation of Magnetic Properties at the Nanometer Scale in Continuously Graded Ferromagnets, Materials (Basel). **11**, 251 (2018).

[9] L. Fallarino, B. J. Kirby, M. Pancaldi, P. Riego, A. L. Balk, C. W. Miller, P. Vavassori, and A. Berger, Magnetic properties of epitaxial CoCr films with depth-dependent exchange-coupling profiles, Phys. Rev. B **95**, 134445 (2017).

[10] M. Quintana, A. Melendez, C. Martín Valderrama, L. Fallarino, and A. Berger, Temperature-Independent Coercivity in Compositionally Graded Ferromagnetic Multilayers M., Phys. Rev. Appl. **18**, 054024 (2022).

[11] P. Riego, L. Fallarino, C. Martínez-Oliver, and A. Berger, Magnetic anisotropy of uniaxial ferromagnets near the Curie temperature, Phys. Rev. B **102**, 174436 (2020).

[12] J. A. Arregi, *Magneto-Optical Ellipsometry and Magnetometry of Thin Films and Multilayers* (Ph.D. Thesis, University of the Basque Country, 2020).

[13] J. Zak, E. R. Moog, C. Liu, and S. D. Bader, Additivity of the Kerr effect in thin-film magnetic systems, J. Magn. Magn. Mater. **88**, 261 (1990).

[14] K. Mok, N. Du, and H. Schmidt, Vector-magneto-optical generalized ellipsometry, Rev. Sci. Instrum. **82**, 033112 (2011).

[15] P. J. Lin-Chung and S. Teitler, 4 × 4 Matrix formalisms for optics in stratified anisotropic media, J. Opt. Soc. Am. A **1**, 703 (1984).

[16] P. Yeh, Optics of anisotropic layered media: A new 4 × 4 matrix algebra, Surf. Sci. **96**, 41 (1980).

[17] Z. Q. Qiu and S. D. Bader, Surface magneto-optic Kerr effect (SMOKE), J. Magn. Magn. Mater. **200**, 664 (1999).

[18] J. Zak, E. R. Moog, C. Liu, and S. D. Bader, Magneto-optics of multilayers with arbitrary magnetization directions, Phys. Rev. B - Condens. Matter Mater. Phys. **43**, 8 (1991).

[19] F. Ilievski, J. C. Perkinson, and C. A. Ross, Magnetic reversal phenomena in pseudo-spin-valve films with perpendicular anisotropy, J. Appl. Phys. **101**, 1 (2007).

[20] F. Bolzoni, F. Leccabue, R. Panizzieri, and L. Pareti, Magnetocrystalline anisotropy and phase transformation in Co-Pt alloy., IEEE Trans. Magn. **20**, 1625 (1984).

[21] T. Thomson, *Magnetic Properties of Metallic Thin Films*, in *Metallic Films for Electronic, Optical and Magnetic Applications* (Elsevier, 2014)

Chapter 6

Other applications of GME

This chapter provides a continuation of the magneto-optical investigations presented in earlier parts of the thesis, but with a focus on applications other than vector magnetometry. More specifically, with a focus on the observation of anomalous/unexpected magneto-optical (MO) signals in magnetic multilayer structures, where novel magnetic behavior emerges due to structural asymmetry, interfacial interactions, or complex coupling. These findings not only expand the understanding of the MO Kerr effect (MOKE) but also establish it as a powerful probe in systems with subtle or complex magnetic textures.

The chapter is divided into two Sections:

- observation of anomalous polar MOKE (P-MOKE) behavior in asymmetric Co/Tb multilayers, associated with magnetic non-uniformities that can generate topological MOKE, and
- observation of anomalous P-MOKE in exchange-coupled uniaxial magnetic thin films, accurately explained by interlayer Dzyaloshinskii-Moriya interaction (DMI),

with each section having its own introduction and motivation, a description of the sample details, the experimental results, and conclusions and outlook.

6.1 Observation of excess P-MOKE signals in asymmetric Co/Tb-multilayers

We study the MO properties of asymmetric Co/Tb-multilayers that are designed to exhibit considerable DMI and weak perpendicular magnetic anisotropy. These structural features should enable the formation of non-uniform magnetization states at intermediate magnetic field strengths, which cause a corresponding net magnetization reduction.

However, at the same time, we observe an excess P-MOKE signal that increases beyond its value at saturation and that is fully anticorrelated with the magnetization in its field dependency. We also find a very strong wavelength dependence of this excess polar MOKE signal that is very different from the MOKE behavior at saturation. All experimental data can be quantitatively explained by an additional P-MOKE mechanism that is associated with magnetic non-uniformities, such as for instance skyrmions, which have already been demonstrated to generate topological MOKE in certain compounds.

6.1.1 Introduction and motivation

As already presented in Chapters 4 and 5 of this thesis, some deviations from the linear approximation of MOKE are related to materials symmetry and require a full tensorial description of Q [1,2]. Other or additional magnetic order parameters, such as non-collinear antiferromagnetic order, can also generate effects analogous to the linear MOKE of ferromagnets [3–6]. It has also been reported that non-uniform magnetic structures that exhibit nontrivial topologies, such as magnetic skyrmions, can give rise to an unconventional linear magneto-optical effect, the topological MOKE [7,8]. Even if it is generally expected that this effect should be vanishingly small [9], there have been recent reports of topological MOKE observations that are associated with the skyrmion lattice states of Gd_2PdSi_3 and the two-dimensional ferromagnet $CrVI_6$ [8,10], in addition to the linear MOKE observations of non-collinear antiferromagnets [3–6].

This raises the question, if unconventional linear MOKE is an occurrence in materials that have the potential to exhibit unconventional magnetic order, including topological non-uniform magnetization structures. My goal in this part of the thesis is to investigate this question experimentally and quantitatively in a precise manner. Specifically, I aim to determine if anomalous excess MOKE signals might occur in otherwise rather conventional magnetic multilayers.

6.1.2 Sample design and fabrication

We fabricated a series of polycrystalline multilayer samples by means of DC-sputter deposition. These samples exhibit perpendicular magnetic anisotropy and asymmetry in the layer structure, as can be seen in Fig. 6.1(a). The repeated multilayer unit consists of Pt/Co/Tb/W. Below and above it, Ta layers are included for the purpose of improved adhesion and oxidation protection only.

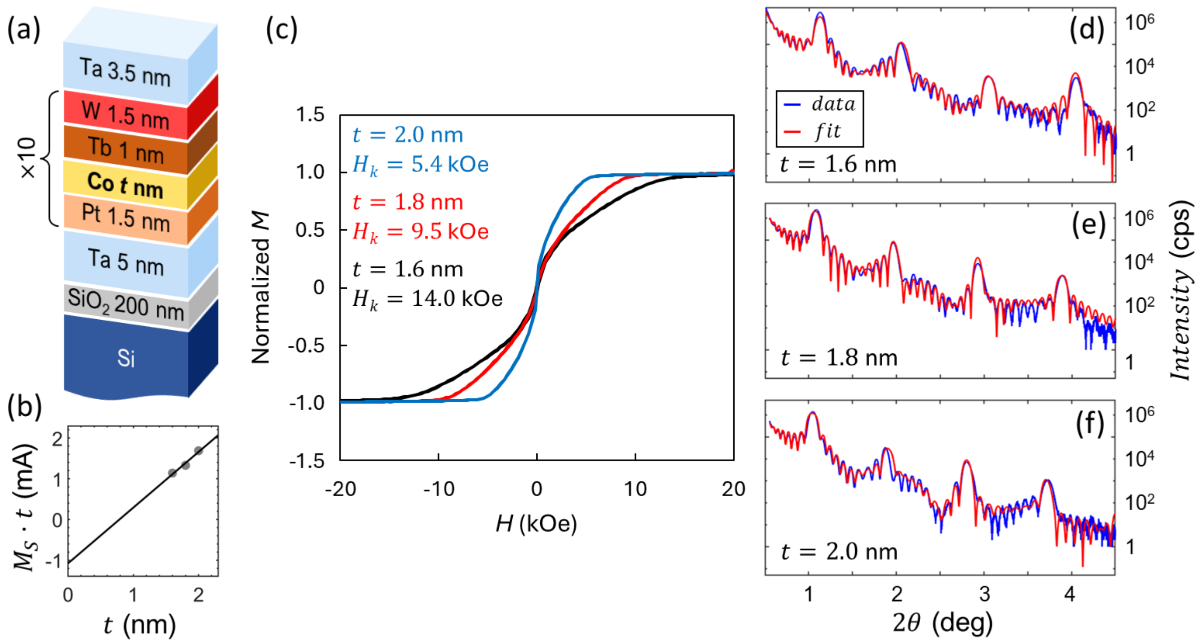

Figure 6.1 (a) Schematic of our sample structure: the multilayer sequence consisting of Pt, Co, Tb and W layers is repeated 10 times; all layer thicknesses are listed with the exception of the Co layer, whose thickness t *was varied. (b) Co thickness* t *evolution of the saturation magnetization* M_s *of our multilayer films and associated linear fit. (c) Normalized in-plane magnetization curves for our magnetic multilayer samples having Co-layer thicknesses* t *of* 1.6 *nm,* 1.8 *nm and* 2.0 *nm, exhibiting anisotropy fields of* 14.0 *kOe,* 9.5 *kOe, and* 5.4 *kOe, respectively. (d) – (f) grazing angle x-ray reflectivity data of 3 samples (blue lines), representing* $t = 1.6$ *nm (d),* 1.8 *nm (e), and* 2.0 *nm (f) in comparison to least-squares fits of the multilayer structures (red lines).*

The idea of the sample structure is two-fold: first, to break inversion symmetry by choosing different top and bottom non-magnetic interface materials, namely Pt and W. Additionally, the central magnetic layer itself is made asymmetric by using Co on the bottom and Tb on top. This approach is designed to facilitate the generation of sizeable DMI strength, which has the potential to generate deviations from simple ferromagnetic order [11–13].

Secondly, the interface induced perpendicular anisotropy in these multilayers can be tuned by a simple variation of the Co layer thickness t. This allows one to generate rather easily magnetic film samples that have only a very weak overall magnetic anisotropy due to a near perfect balancing of interface induced perpendicular and magnetostatic in-plane anisotropy [14,15]. Corresponding anisotropy measurements for our samples exhibit exactly this dependency. Fig. 6.1(c) includes the normalized in-plane magnetization curves for samples having a nominal Co-layer thickness t of 1.6, 1.8 and 2.0 nm, identifying the corresponding anisotropy fields H_k of 14.0, 9.5 and 5.4 kOe, respectively. This demonstrates a very relevant reduction of effective anisotropy upon increasing the Co layer thickness, leading to an energy balance that makes non-uniform magnetic textures viable for sufficiently large t. It is well known, that in this parameter range, magnetic multilayers are very susceptible to small energy variations and already small modifications can cause very relevant magnetic state modifications, such as the formation of various non-uniform states [12]. Thus, upon tuning t, the net magnetic anisotropy can be modified and thus the relevance of DMI can be turned on or off in a very simple manner.

Furthermore, it is worth noting that the antiparallel orientation of the Co and Tb magnetizations, which is experimentally confirmed by the negative axis intercept at $t = 0$ in Fig. 6.1(b), leads to an overall reduced total magnetization. This modifies the critical Co thickness, at which the anisotropy is compensated to larger t values, which in turn can be better controlled [14,15].

The growth quality of our samples has been confirmed by means of x-ray reflectivity (XRR) measurements, as shown in Figs. 6.1(c)-1(e) for three samples having different t. Both, the total thickness and the multilayer oscillations are very clearly visible and they match the utilized multilayer model very well. Least-squares fits to the model have been done utilizing the AMASS XRR software, with the fitting parameters being included in Tables 6.1, 6.2 and 6.3. The multilayer peak shifts that are associated with increasing t are very visible if one compares the results for these three samples with relevant peaks moving towards smaller 2θ values in the XRR data.

Layer	*Density (g/cm³)*	*Thickness (nm)*	*Roughness (nm)*
Ta_2O_5	7.99	1.90	0.18
Ta	16.33	2.37	0.01
W	21.51	1.05	0.11
Tb	18.42	0.78	0.2
Co	4.77	1.49	0.19
Pt	24.95	1.09	0.53
Ta	20.86	4.75	0.19
SiO_2	2.39	193.5	0.40
Si	2.388	600000	0.11

T*able 6.1. Fitting results of the logarithm of the x-ray reflected intensity for the sample with nominal Co thickness* $t = 1.6$ *nm. The corresponding* R^2 *value is* 0.984*. The layers marked in grey have been repeated 10 times in the model structure with the fitting parameters being identical for all repetitions.*

Layer	*Density (g/cm³)*	*Thickness (nm)*	*Roughness (nm)*
Ta_2O_5	7.90	1.87	0.22
Ta	15.84	2.20	0.15
W	21.08	1.18	0.17
Tb	18.22	0.73	0.15
Co	5.93	1.87	0.01
Pt	26.18	0.79	0.53
Ta	18.31	4.87	0.27
SiO_2	2.61	207.93	0.36
Si	2.32	600000	0.01

Table 6.2 Fitting results of the logarithm of the x-ray reflected intensity for the sample with nominal Co thickness $t = 1.8$ *nm. The corresponding* R^2 *value is* 0.976. *The layers marked in grey have been repeated 10 times in the model structure with the fitting parameters being identical for all repetitions.*

Layer	*Density (g/cm³)*	*Thickness (nm)*	*Roughness (nm)*
Ta_2O_5	8.68	2.13	0.31
Ta	17.39	2.25	0.003
W	22.39	0.93	0.24
Tb	20.77	0.85	0.01
Co	5.06	2.06	0.14
Pt	26.38	0.97	0.35
Ta	20.14	5.01	0.1
SiO_2	2.91	197.14	0.26
Si	2.32	600000	0.03

Table 6.3. Fitting results of the logarithm of the x-ray reflected intensity for the sample with nominal Co thickness $t = 2.0$ *nm. The corresponding* R^2 *value is* 0.957. *The layers marked in grey have been repeated 10 times in the model structure with the fitting parameters being identical for all repetitions.*

In summary, we have fabricated a multilayer thickness series with an asymmetric structure that can generate relevant levels of DMI and is furthermore tunable in terms of its net perpendicular anisotropy, so that DMI related magnetization states and potentially associated excess MOKE have favorable conditions or are suppressed, depending on t. After fabrication, we have investigated our samples by means of vibrating sample magnetometry (VSM) to verify their magnetization orientation and reversal properties and by means of generalized magneto-optical ellipsometry (GME) and Kerr microscopy to quantify their precise MO properties and micromagnetic structures.

6.1.3 Results and discussion

Figures 6.2(a)-(c) show VSM measurements of the out-of-plane magnetization M as a function of field H for three samples with nominal Co-thicknesses $t = 1.6$, 1.8, and 2.0 nm. All curves show weak perpendicular anisotropy behavior with low saturation fields and a pinched central hysteresis that is indicative of perpendicular domain formation at low fields [15-17]. Also, the slanting of the central hysteresis loop portion increases with increasing t, which is fully consistent with the intended reduction of perpendicular anisotropy [15-17].

GME measurements were performed for the same samples and perpendicular field orientation to corroborate all aspects of our VSM observations. Figures 6.2(d)-(f) show the obtained MOKE coefficients. Given the vector magnetometry capabilities of GME [18–22], all three magnetization components associated parameters are determined simultaneously. We observe that the in-plane longitudinal MOKE $\tilde{\alpha}$ and transverse MOKE $\tilde{\beta}$ are vanishingly small in the entire field range, while the out-of-plane polar MOKE $\tilde{\gamma}$ shows a hysteresis-like behavior. This corroborates the occurrence of a perpendicular domain state in the low field region with no net in-plane magnetization being observed. We also find that the polar MOKE signal in saturation shows no relevant field dependence and that its amplitude scales with t, as displayed in the inset of Fig. 6.2(f), in almost the exact same manner as the magnetization in Fig. 6.1(b). Accordingly, all films exhibit an antiparallel magnetization state in between the Co and Tb films for the maximum field strength applied here, with the total magnetization and the polar MOKE amplitude linearly increasing with t.

There is, however, one aspect of the data in Fig. 6.2 that is not compatible with this conventional picture. For the $t = 2.0$ nm sample that exhibits weak effective anisotropy as well as DMI, the VSM magnetization shows a noticeable reduction of its magnetization in the field range $\mu_0 H = 70 - 450$ mT, even before conventional domain states form, which does not occur for thinner films. Furthermore, this M reduction is not accompanied by a polar MOKE reduction, but instead $\tilde{\gamma}$ vs. H seems to increase slightly above its saturation value upon reducing H in this intermediate field range.

To visualize this anomaly better, Fig. 6.3(a) shows a zoom-in of $|\tilde{\gamma}|$ vs. H data for these three samples for the hysteresis loop branch with decreasing field strength. Here, we observe conventional behavior for two of the samples ($t = 1.6$ and 1.8 nm), whereas the data show an anomalous increase of the polar MOKE signal upon decreasing the field for the $t = 2.0$ nm sample. This increase of $|\tilde{\gamma}|$ occurs simultaneously with the small and non-hysteretic magnetization reduction in the $H = 70 - 450$ mT field range. Thus, in the $t = 2.0$ nm sample and this field range, the conventional linear relationship in between magnetization and linear MOKE is not conserved and is instead inverted.

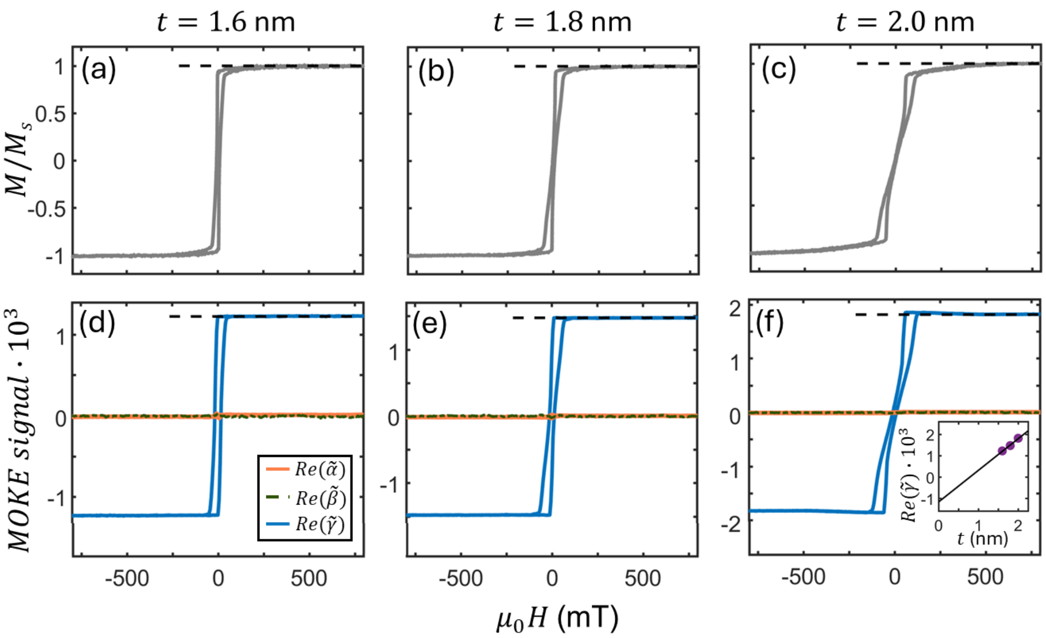

Figure 6.2 VSM magnetometry $\boldsymbol{M}$ *vs.* $\boldsymbol{H}$ *data (a) – (c), compared to GME data (d) – (f) for the same samples using an applied magnetic field* $\boldsymbol{H}$ *along the surface normal. The plots show data for* $\boldsymbol{t} = 1.6$ *nm (a, d),* 1.8 *nm (b, e), and* 2.0 *nm (c, f) samples. The dashed lines in each subplot represent high field saturation values as guides to the eye. The plots (d) – (f) display in addition to the polar MOKE quantity* $\boldsymbol{Re(\tilde{\gamma})}$ *(blue line), signals associated with the longitudinal MOKE (*$\boldsymbol{Re(\tilde{\alpha})}$*, orange line) and transverse MOKE (*$\boldsymbol{Re(\tilde{\beta})}$*, green dash-dotted line). The inset in (f) displays the thickness* $\boldsymbol{t}$ *evolution of* $\boldsymbol{Re(\tilde{\gamma})}$ *in saturation for our multilayer films (dots) in comparison to a linear fit (line).*

This aspect is displayed in Fig. 6.3(b), which shows a conventional linear polar MOKE $|\tilde{\gamma}|$ vs. M correlation for the $t = 1.6$ and 1.8 nm samples in the $\mu_0 H > 70$ mT field range, while the $t = 2.0$ nm sample shows a clear anti-correlation behavior between $|\tilde{\gamma}|$ and M. Hereby, it is important to emphasize that we do not observe a loss of correlation, but an obvious inversion of its sign, resulting in the anti-correlation of excess polar MOKE $|\tilde{\gamma}|$ with the field strength and the magnetization reduction. It is also worth noting that second order magneto-optical effects cannot be responsible for this deviation, because they are rigorously removed from the data in the GME analysis scheme [19]. So, an unconventional excess polar MOKE occurs in this type of sample, which exhibits a still linear magnetization dependence, but with inverted slope, in addition to the also present conventional linear MOKE that is proportional to M, and which can be visualized by directly comparing MOKE with magnetometry data [1].

---

[1] The fact that the linear slope for the t = 1.6 and 1.8 nm samples in Fig. 2(b) is not 1, but considerably smaller is a common occurrence if one compares VSM and MOKE data. It stems from the fact that in MOKE only a central portion of the sample is measured, whereas VSM measurements include the entire sample, including sample boundaries, in which imperfect magnetization behavior due to an increased defect density occurs more frequently. The different sample averaging in between VSM and MOKE measurements can lead to a slope modification, but it cannot result in the type of slope inversion that is observed

In this anomalous field regime, the excess γ does not coincide with any in-plane MOKE signal (see Fig. 6.2(f)) and does not exhibit any hysteresis, as can be seen in Fig. 6.3(c), where the difference signal $\delta\tilde{\gamma}$ between the two hysteresis loop branches is plotted. Here, we find no difference in behavior between the field ranges that correspond to saturation at high field values and intermediate field strengths (yellow highlighted), where the excess polar MOKE occurs for both branches of the field cycle. The here observed behavior is very different from other multilayer observations, in which samples exhibit a breakdown of MOKE vs. M correlation due to spin-flop transitions, for instance, that can be associated with the different layers contributing differently to the total signal as a function of field [23]. In the case here, the correlation is fully preserved, just its sign is inverted. Also, no phase transition seems to occur in the anomalous regime, given the complete lack of hysteresis. Furthermore, the M vs. H, the $|\tilde{\gamma}|$ vs. H, and the M_s vs. t behavior are all fully consistent with an antiparallel Co/Tb magnetization state, even at the largest applied field, so that there is no apparent mechanism that would drive a layer dependent magnetization reorientation as a function of field.

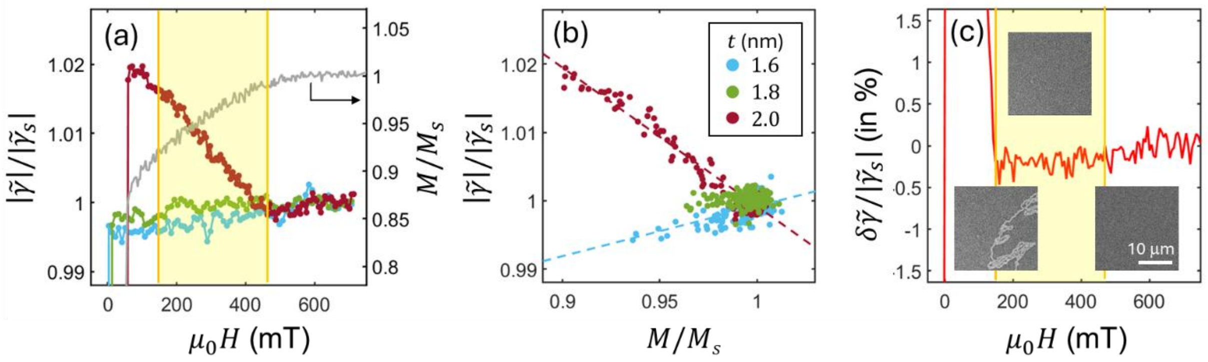

Figure 6.3 Saturation behavior of the polar MOKE signal $|\tilde{\gamma}|$ in our samples; (a) displays $|\tilde{\gamma}|$ vs. H for decreasing field amplitude for the $t = 1.6$, 1.8, and 2.0 nm (blue, green and red dots, respectively) samples; the thin colored lines are guides to the eye. For comparison, the M vs. H data for decreasing field strength for the $t = 2.0$ nm sample are displayed as a grey line (the respective axes assignment is indicated by the black arrows); (b) $|\tilde{\gamma}|$ vs. M dependence, measured for decreasing field amplitude for the three $t = 1.6$, 1.8, and 2.0 nm samples; the dashed colored lines represent linear fits to the data; (c) polar MOKE signal difference $\delta\tilde{\gamma}$ between the decreasing and the increasing field branch measurements vs. H for the $t = 2.0$ nm sample; insets in (c) are MOKE microscopy images taken at $\mu_0 H = 60, 75$ and 360 mT, respectively, demonstrating the absence of detectable domain pattern for all fields $\mu_0 H > 70$ mT on the decreasing field branch; the vertical yellow lines in (a) and (c) indicate the field range, where anomalous MOKE signals occur in both branches.

To further elucidate the nature of this anomalously increased polar MOKE signal, my collaborators have conducted Kerr microscopy observations for different field strengths [24].

---

for the t = 2.0 nm sample, given that no MOKE signal increase can occur due to mere averaging differences in between the two measurement methods.

Exemplary MOKE-microscopy images are displayed as insets in Fig. 6.3(c). Here, the $t = 2.0$ nm sample shows the expected high field and low field behavior, displaying a saturated uniform state at high field and a perpendicular multi-domain state at sufficiently low magnetic fields after surpassing the domain nucleation threshold [15]. In the anomalous MOKE regime, it cannot be observed any indication for static domain or skyrmion generation. Instead, uniform magnetization states are found on the time and spatial resolution level that can be achieved with the MOKE microscope. This indicates that the magnetic non-uniformities that occur in the $t = 2.0$ nm sample, and which lead to the magnetization reduction must be smaller than the resolution limit or fluctuation like states into which the uniform state locally fluctuates, because DMI and perpendicular anisotropy are designed to be in near balance. The latter possibility seems to be supported by the lack of hysteresis in the intermediate field range in my GME and VSM data. In addition, it should be mentioned that my observation of having an intermediate field strength occurrence of M and polar MOKE anomalies is consistent with other skyrmion and skyrmion lattice observations [8,25].

The simultaneous nature of our M vs. H and $\tilde{\gamma}$ vs. H observations can be understood in that below a threshold field of about 450 mT, a field-dependent fraction $f(H)$ of the sample is in a non-uniform magnetization state, such as for instance, a skyrmion or skyrmion fluctuation. Such a state would reduce the total magnetization as

$$\frac{M}{M_s}(H) = 1 - f(H). \tag{6.1}$$

At the same time, the conventional linear polar MOKE $\tilde{\gamma}_{lin}$ will be reduced proportionally

$$\frac{\tilde{\gamma}_{lin}}{\tilde{\gamma}_s}(H) = 1 - f(H). \tag{6.2}$$

with $\tilde{\gamma}_s$ being the polar MOKE at saturation. However, the experimentally observed polar MOKE $\tilde{\gamma}_{exp}$ does not reduce, so that the non-uniform magnetization entities must generate an unconventional excess polar MOKE $\tilde{\gamma}_E$ proportional to their relevant density $f(H)$. Thus, in total

$$\tilde{\gamma}_{exp}(H) = \tilde{\gamma}_s\big(1 - f(H)\big) + \tilde{\gamma}_E f(H) = \tilde{\gamma}_s + \Delta\tilde{\gamma}_E f(H) \ = \tilde{\gamma}_s + \Delta\tilde{\gamma}_E \left[1 - \frac{M}{M_s}(H)\right], \tag{6.3}$$

with $\Delta\tilde{\gamma}_E = \tilde{\gamma}_E - \tilde{\gamma}_s$. Accordingly, the $\tilde{\gamma}_{exp}$ vs. M anticorrelation in Fig. 6.3(b) is clearly possible as long as an excess MOKE mechanism exists and is larger per unit area than the conventional linear polar MOKE $\tilde{\gamma}_{lin}$. As one can see from Fig. 6.3(b), my experimental data are very well described by Eq. (6.3), which supports my formal excess MOKE description.

To better characterize the excess MOKE and possibly elucidate its origin, I have conducted spectroscopic MOKE measurements. If this excess polar MOKE has a topological MOKE origin, it should exhibit a wavelength dependence that is substantially different from the conventional linear MOKE, due to its different formal origin, and thus one would expect to find a strongly λ-dependent $\Delta\tilde{\gamma}_E/\tilde{\gamma}_s$ [7,8]. This is indeed what I observe.

Figure 6.4(a) shows that there is a very significant wavelength dependence of the excess polar MOKE with the anomaly becoming stronger for longer wavelengths λ and basically disappearing at $\lambda = 545$ nm. One can also see that the field value, at which the anomaly sets in, is the same for all measurements independent from λ, and consistent with an observation-independent occurrence of magnetic non-uniformities, such as skyrmions or skyrmion-like entities [8]. Thus, all data in Fig. 6.4(a) are described by Eq. (6.3), making the assumption of a unique and λ-independent $M(H)$ and a λ-dependent $\Delta\tilde{\gamma}_E$. The solid lines in Fig. 6.4(a) are fits to Eq. (6.3) under the additional assumption that $M(H) = M_s$ for $\mu_0 H > 450$ mT, which describe all data very well.

Figure 6.4(b) shows the resulting quantitative $\Delta\tilde{\gamma}_E/\tilde{\gamma}_s$ values vs. λ for the combined fit of all data, displaying a strong variation of $\Delta\tilde{\gamma}_E/\tilde{\gamma}_s$. While it essentially vanishes for $\lambda = 545$ nm, it increases strongly for larger wavelengths and leads to significant excess polar MOKE amplitudes in the $t = 2.0$ nm Pt/Co/Tb/W multilayer sample, which exhibits very low effective anisotropy and thus is designed to enable non-uniform magnetization structures that depend on the DMI-to-anisotropy balance. It should also be mentioned that the quantitative $\Delta\tilde{\gamma}_E/\tilde{\gamma}_s$-values, shown in Fig. 6.4(b), represent a lower estimate, given that they are based on VSM determined $M(H)$-data, which might differ slightly from $M(H)$ in the laser spot area that is utilized for my MOKE measurements.

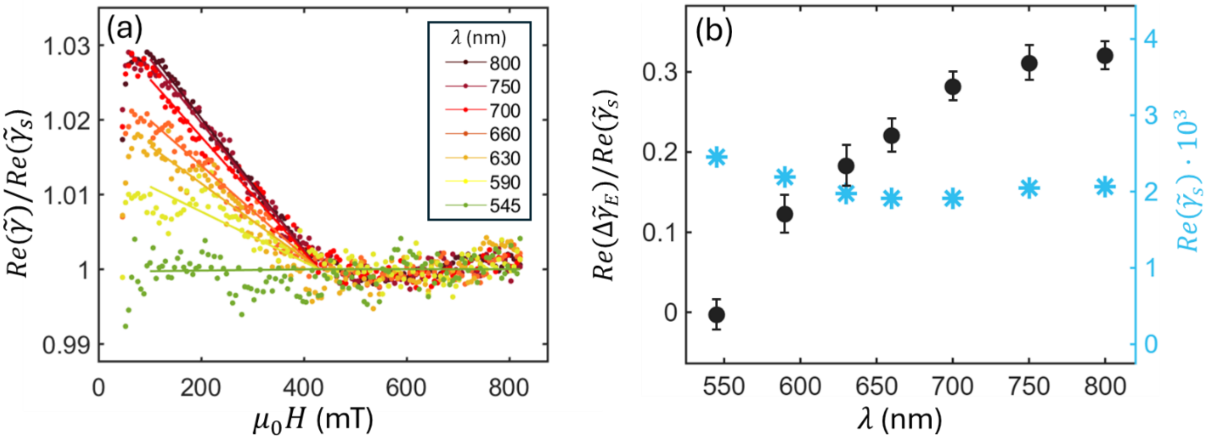

Figure 6.4 (a) Saturation behavior of the polar MOKE signal $Re(\tilde{\gamma})$ vs. H for the $t = 2.0$ nm sample and different wavelengths λ; the experimental data are shown as points, whereas the lines represent least-squares fits of the data to Eq. (6.3); the different wavelength data are represented by different colors as defined in the legend; (b) extracted excess polar MOKE values $Re(\Delta\tilde{\gamma}_E)/ Re(\tilde{\gamma}_S)$ vs. λ according to Eq. (6.3), shown as black dots using the left-side scale, in comparison to the λ dependence of the saturation polar MOKE signal $Re(\tilde{\gamma}_S)$, shown as blue stars using the right-hand scale. Error bars for $Re(\tilde{\gamma}_S)$ are consistently smaller than the symbol size and thus not shown.

6.1.4 Conclusions and outlook

I have studied the magnetic and MO properties of asymmetric Pt/Co/Tb/W multilayers that are designed to exhibit considerable DMI and low effective perpendicular magnetic anisotropy. By tuning the Co layer thickness, we created samples with varying net anisotropy, which should enable the controlled appearance (or suppression) of non-uniform magnetic states.

Accordingly, in samples where DMI and anisotropy are nearly balanced, we observe a net magnetization reduction at intermediate field strengths that is indicative of the occurrence of non-uniform magnetization states in some fraction of the sample. Simultaneously with this non-hysteretic magnetization reduction, we observe a polar MOKE signal in the visible spectrum that increases beyond the saturation level, exhibiting a very precise anti-correlation of magnetization and excess polar MOKE signal.

All observations are quantitatively described by a model in which a field-dependent fraction of the sample enters a non-uniform magnetic state. This fraction reduces the conventional magnetization and linear MOKE response, while simultaneously generating an additional polar MOKE contribution. The resulting excess MOKE behaves linearly, but with an inverted slope relative to the magnetization.

Spectroscopic measurements reveal that the excess polar MOKE has a different wavelength dependence compared to conventional MOKE. This strong spectral dependence supports an interpretation in terms of a topological MOKE, consistent with the presence of skyrmions or skyrmion-like fluctuations as the origin of the observed excess signal [26,27].

6.2 Anomalous P-MOKE signal in exchange-coupled uniaxial magnetic thin films

Interlayer exchange coupling between magnetic films in a multilayer structure has long been a fundamental research topic in magnetism. Recent interest has focused on interlayer exchange coupling mediated by the DMI across a mediating layer, which introduces the possibility of engineering 3-dimensional magnetic structures into multilayer systems. In this work, I come back to the epitaxial ferromagnetic (FM_1)/non-magnetic (NM)/FM_2 multilayers investigated in Chapter 5, where the FM layers have different composition and anisotropy strengths, but both possess uniaxial in-plane anisotropy and share the same easy axis (EA) orientation. In Chapter 5 I focused on the in-plane MOKE parameters ($\tilde{\alpha}$ and $\tilde{\beta}$), but an anomalous out-of-plane MOKE observation was found for some of these samples under certain conditions. This polar MOKE does not affect the results nor conclusions stated in Chapter 5: as an estimation, the polar effect is typically 10 times larger than the longitudinal effect for full magnetization orientation along the respective axis. Now the longitudinal effect for these samples and measurements is about 3 times larger. This would mean that the out-of-plane angle is about 1/30 in radians, which means that the magnetization rotates about 2 deg out of plane. In turn, the in-plane magnetization components are $cos(2°) = 0.999$ of the full in-plane case. Thus, the in-plane behavior can be sensibly assumed to be unperturbed from the pure in-plane case.

This experimentally observed anomalous polar MOKE signal cannot be explained by conventional bilinear or biquadratic coupling, but it could be replicated considering interlayer DMI (IL-DMI). My findings demonstrate how interlayer coupling interactions can work to produce a net out-of-plane magnetization in nominally in-plane magnetic multilayers, that can be directly determined with GME measurements.

6.2.1 Introduction and motivation

The phenomenon of interlayer exchange coupling in magnetic multilayers has been the subject of intense study for several decades already, largely due to its impact on fundamental magnetic properties and relevance for technological applications [26–30]. While bilinear and biquadratic coupling mechanisms were already thoroughly established in the 1990s, focus has recently shifted towards exchange interactions that have a helical nature and originate from the DMI [31,32]. Originally introduced by Dzyaloshinskii [31] and later formulated by Moriya [32], the DMI arises from spin-orbit coupling in systems lacking inversion symmetry and has been widely recognized for stabilizing non-collinear and chiral spin textures such as spin spirals and skyrmions [27,33]. Although most DMI studies center on interfacial phenomena within ultrathin FM/ heavy metal interfaces, emerging experiments and theory show that DMI can also propagate across non-magnetic spacers, giving rise to interlayer DMI [27,34–39]. This interlayer interaction provides new possibilities and additional design freedom for achieving three-dimensional chiral magnetic textures in multilayers.

Indeed, recent theoretical and experimental studies have shown that DMI contributions can be both interlayer and intralayer in nature, and that IL-DMI related magnitude can oscillate with spacer or capping thickness due to RKKY-type interactions or orbital hybridization effects [34,35,40]. Moreover, IL-DMI can be manifested in synthetic antiferromagnets and multilayers with strong spin-orbit coupling (SOC) materials such as Ru, Pt, Pd and Ir where it can induce orthogonal magnetization alignments, chiral domain wall motion, and field-free spin-orbit torque switching [40–42]. Experimental confirmation of IL-DMI has relied primarily on transport-based methods such as anomalous Hall effect (AHE) and loop asymmetry measurements [41,42], while Brillouin light scattering has been used to probe interfacial DMI via non-reciprocal spin-wave dispersion [43]. More recently, MO techniques have also been used to detect IL-DMI in systems with weak SOC, as in the case of Co/Ag/Co trilayers [22].

Here, I demonstrate that IL-DMI can be generated in a fully epitaxial system with in-plane uniaxial anisotropy, in contrast to previously studied systems with perpendicular magnetic anisotropy (PMA) or a combination of PMA and in-plane anisotropy. I measure the MO signal produced by a FM/ NM/ FM multilayer system. The two FM thin films share the same in-plane EA, but differ in their composition and anisotropy strength in order to break the symmetry and generate IL-DMI. Indeed, the symmetry breaking in our study does not come from the overall structure itself, but from the different composition of the two FM layer. By means of GME, I quantify the three-dimensional magnetization vector, observing an out-of-plane magnetic signal that cannot be explained by conventional bilinear or biquadratic exchange models, but is successfully reproduced by including an IL-DMI term in a macrospin model.

6.2.2 Sample design and fabrication

The multilayer system here utilized consists of the FM$_1$/ NM/ FM$_2$ epitaxial multilayer created to accomplish layer-resolved vector magnetometry for two FM layer samples. Let me remind you that the two FM thin layers consisted of a 2 nm Co layer and a 2.1 nm Co$_{0.86}$Pt$_{0.14}$ (Co-Pt) layer, as previously included in Fig. 5.2(a) and indicated here again in Fig. 6.5(a). These layers have different anisotropy strengths but the same EA orientation. The NM layer of Co$_{0.59}$Ru$_{0.41}$ has a thickness t systematically varied from sample to sample. By its sheer designed nature, the structure is asymmetric, thus DMI could in principle appear. The out-of-plane signals for these samples are very weak, but not completely absent in all of these samples. Therefore, I conducted an in-depth study for a few selected films to check if anomalous P-MOKE signals occur and how they could be explained, given that without DMI, no mechanism should move the layer magnetizations out of the plane. Specifically, I look in detail at three thickness cases: $t = 0$, 2.35 and 8 nm.

- For $t = 0$ nm, the FM layers are fully coupled, and as the two magnetization vectors rotate synchronously, there is no symmetry breaking happening and no IL-DMI should be generated.
- For $t = 8$ nm, the FM layers are fully decoupled (see Fig. 5.10(a)), which means that there is no interlayer exchange between the two FM layers, and therefore no IL-DMI should be generated neither.
- For intermediate thickness cases, as $t = 2.35$ nm, there is a relevant FM coupling happening between the two FM layers but it allows independent rotations of each layer's magnetization vector so the symmetry of the magnetization vectors is broken. Therefore, for $t = 2.35$ nm case, IL-DMI should be generated [44,45].

Reference samples containing only one of the FM layers to establish baseline MO signatures in the absence of interlayer coupling are also here considered. Given the epitaxial nature of each FM layer, the magnetization of each film behaves like an in-plane macrospin, confirmed experimentally for this sample type [20,46–48].

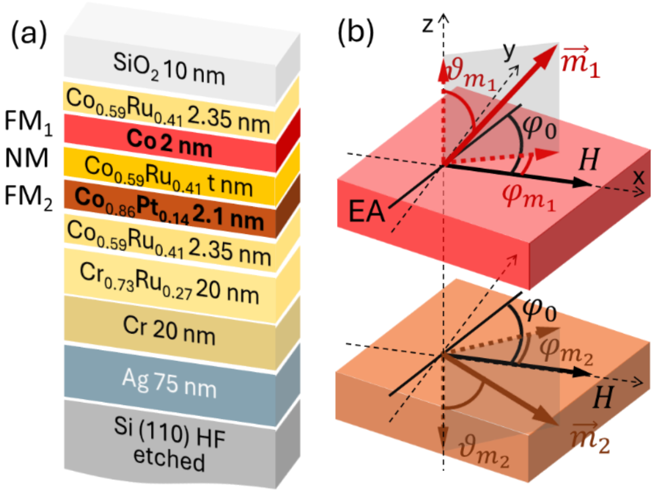

Figure 6.5 Schematic of the layer geometry and epitaxial sequence utilized, with the respective materials and thicknesses indicated. (b) definitions of the EA and normalized magnetization vector $\vec{m}$ orientation and angles φ_0, φ_{m_i} and ϑ_{m_i} with respect to the sample surface and the applied field direction H.

The growth strategy of the FM/NM/FM structure to achieve the intended epitaxy was already explained in Chapter 5 and the schematic of the magnetization behavior of two FM layers was also already shown in Fig. 5.1. However, let me include here an additional schematic in Fig 6.5(b) including the magnetization behavior of the two FM layers considering an out of plane component. The magnetization vectors and their projections onto the cartesian axis are defined by the sample's surface plane and the direction of the applied field H.

6.2.3 Results and discussion

GME measurements were done, with the set up in the in-plane geometry (Fig. 4.3(a)) and with the samples oriented with $\varphi_0 = 75$ deg. Figure 6.6 includes the experimentally determined real parts of $\tilde{\alpha}$, $\tilde{\beta}$ and $\tilde{\gamma}$ for the samples with $t = 0$, 2.35 and 8 nm and the reference samples with one FM layer only. The magnetization vectors align with the EA at low H values, producing a mostly transverse ($\tilde{\beta}$) MOKE signal. Upon increasing H, the magnetization rotates towards the x-axis, aligning with it for high H values and therefore generating a mostly longitudinal ($\tilde{\alpha}$) MOKE signal. We can see the aforementioned variation of the longitudinal and transverse signal with H in the first and second row of Fig. 6.6, where the behavior is exactly as expected for a perfect in-plane rotation. They also present a hysteresis-like behavior: there is an abrupt switch in the MOKE signals happening at the coercive field of the sample. In the case of the completely decoupled sample of $t = 8$ nm, one can see two switches, one for each FM layer at the corresponding coercive fields of each layer.

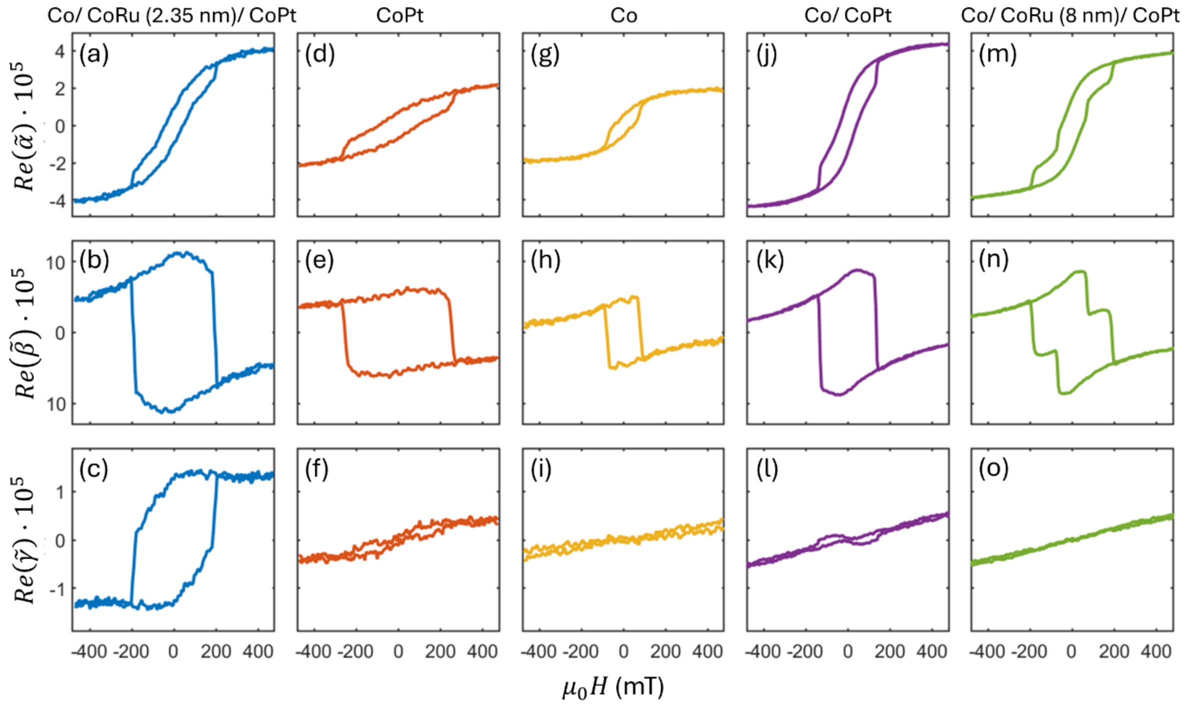

Figure 6.6 Applied field evolution of the real part of the MO parameters $\tilde{\alpha}$, $\tilde{\beta}$ and $\tilde{\gamma}$ for (a-c) the multilayer sample with the two FM thin films and a CoRu interlayer of 2.35 nm, for the reference samples with thin CoPt (d-f) and Co (g-i) films, and for the multilayer samples without interlayer (j-l) and with a thick interlayer of 8 nm (m-o). The EA orientation is equal to $\phi_0 = 75$ deg.

The third row of Fig 6.6 shows the polar ($\tilde{\gamma}$) MOKE signal, related to the out-of-plane magnetization component, which is expected to be very small and vary linearly with the field, if there is a misalignment of the applied field orientation. Indeed, for the reference samples (Figs. 6.6(f,i)) the out-of-plane signal shows this expected small out-of-plane behavior, as well as for the completely coupled (Fig. 6.6(l)) and decoupled (Fig. 6.6(o)) FM layer samples. However, for the multilayer sample with intermediate coupling (Fig. 6.6(c)), $\tilde{\gamma}$ shows a significant non-linear signal. This unexpected out-of-plane behavior should not be present, and different possible mechanisms for this unexpected signal will have to be considered.

To further understand this out-of-plane signal obtained for the $t = 2.35$ nm sample, GME measurements were performed for different φ_0 values on this sample. Any accidental out-of-plane signal should not exhibit a systematic angular pattern, so that a detailed angular dependence measurement should allow for a very clear distinction between noise and real data pattern. For the layer resolved vector magnetization, this would not have been helpful, because each different magnetic field orientation represents an independent data set and different magnetization orientation. Thus, it cannot improve the quantitative accuracy of vector magnetometry. However, it is indeed very helpful in the identification of anomalous signal pattern. The reference samples were also measured under the same conditions to have a clear comparison and better understanding. The resulting $\tilde{\alpha}, \tilde{\beta}$ and $\tilde{\gamma}$ dependences as a function of H and φ_0 are represented in Fig. 6.7. The first and second rows of Fig. 6.7 include the in-plane results for the three samples. For φ_0 values close to 180 deg, the magnetization vector keeps its orientation fixed and aligned with the EA and the field orientation until it switches abruptly. One can observe this switch of the magnetization vector in the x-axis magnetization-related MOKE parameter α in Fig. 6.7(a,d,g), which is represented by the abrupt color change from yellow to blue at the coercive field as the field H decreases. For the same φ_0 orientation close to 180 deg values, no y-axis magnetization related MOKE parameter $\tilde{\beta}$ is observed, as one can see in Fig. 6.7(b,e,h). For smaller φ_0 angles, one can see the rotation of the magnetization vector already explained, as both $\tilde{\alpha}$ and $\tilde{\beta}$ decrease and increase, respectively, (in absolute values) with H going from the maximum positive value to zero, before switching at negative fields. Moreover, the out-of-plane magnetization related to $\tilde{\gamma}$ for the reference samples (Figs. 6.7(c,f)) does not change with φ_0, having the same small linear signal for all φ_0 values. However, for the $t = 2.35$ nm multilayer sample, the previously observed non-linear signal of the out-of-plane component $\tilde{\gamma}$ in Fig. 6.6(c) shows a strong variation with φ_0 that differs from that of $\tilde{\alpha}$ and $\tilde{\beta}$ and from the small linear signal of $\tilde{\gamma}$ of the reference samples.

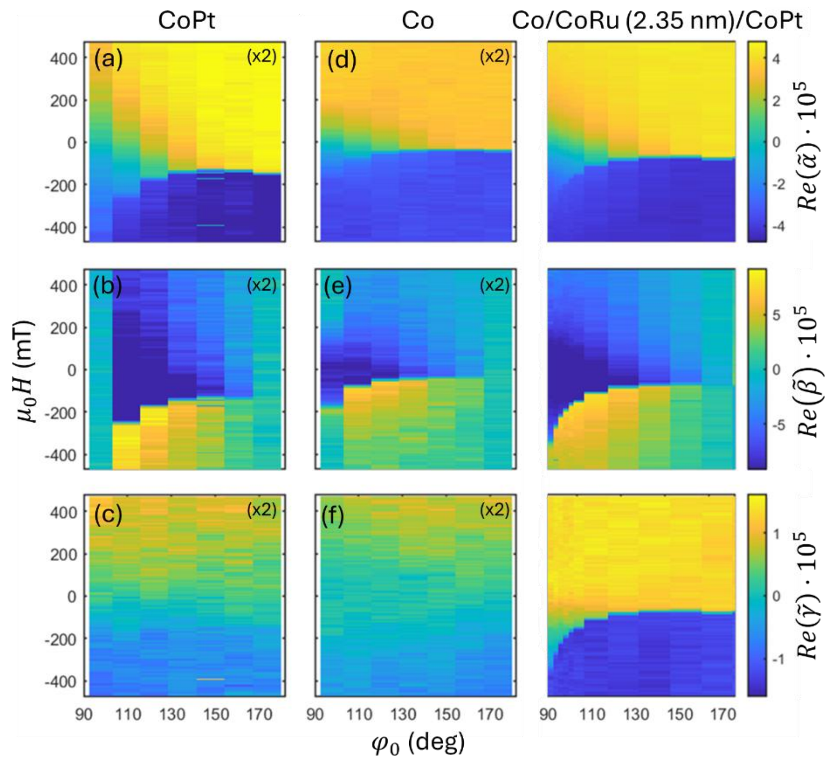

Figure 6.7 Experimental color-coded maps of the real part of the MOKE parameters $\tilde{\alpha}, \tilde{\beta}$ *and* $\tilde{\gamma}$*, represented in function of* H *and* φ_0*. Each column corresponds to a different sample, being (a-c) and (d-e) for the reference samples and (g-i) for the multilayer sample with* 2.35 *nm of CoRu interlayer. The color scale for the maps of the reference samples is two times bigger than for the multilayer sample.*

To understand this unexpected effect, I calculated the magnetization vector orientation of each FM layer in a system that replicates the experimental multilayer sample. I focused on the interlayer coupling because individual layers, uncoupled layers and very strongly coupled layers do not show this effect, because they behave like a single in-plane layer. Thus, it is the intermediate interlayer coupling strength that makes the 2.35 nm sample different from the other and thus, it is sensible to assume that interlayer coupling is relevantly connected to the origin of this MOKE anomaly.

Therefore, I modeled the system as two macrospins ($\overrightarrow{m_1}$ and $\overrightarrow{m_2}$), having different uniaxial anisotropy strengths given by the first-order anisotropy energies K_{m1} and K_{m2}, respectively, coupled by bilinear $E_{bl} = -J_{bl}\,\overrightarrow{m_1} \cdot \overrightarrow{m_2}$, biquadratic $E_{bq} = -J_{bq}\,(\overrightarrow{m_1} \cdot \overrightarrow{m_2})^2$ and DMI $E_{DMI} = -\vec{D} \cdot (\overrightarrow{m_1} \times \overrightarrow{m_2})$ interactions, so that one can compare the effect of DMI, biquadratic and bilinear coupling upon turning them on separately. Including the Zeeman energy for each macrospin, the total energy reads:

$$E_{tot} = K_{m1}(1 - (\overrightarrow{m_1} \cdot \vec{e})^2) + K_{m2}\,(1 - (\overrightarrow{m_2} \cdot \vec{e})^2) - \mu_0\,\vec{H} \cdot \overrightarrow{m_1} - \mu_0\,\vec{H} \cdot \overrightarrow{m_2} - J_{bl}\,\overrightarrow{m_1} \cdot \overrightarrow{m_2} - J_{bq}\,(\overrightarrow{m_1} \cdot \overrightarrow{m_2})^2 - \vec{D} \cdot (\overrightarrow{m_1} \times \overrightarrow{m_2}), \tag{6.4}$$

where $\vec{e}$ is a unit vector that represents the EA direction. Considering different orientations of the EA and different H values, in a way to replicate the experimental procedure and conditions, I obtained the magnetization vector components represented in Fig. 6.8. The experimental color-coded maps of the real part of the MOKE parameters $\tilde{\alpha}, \tilde{\beta}$ and $\tilde{\gamma}$ are also included in Fig. 6.8(a,b,c) to better compare them with the calculated solutions; here the angular range φ_0 is shifted to appreciate the signal symmetries around the HA of the sample.

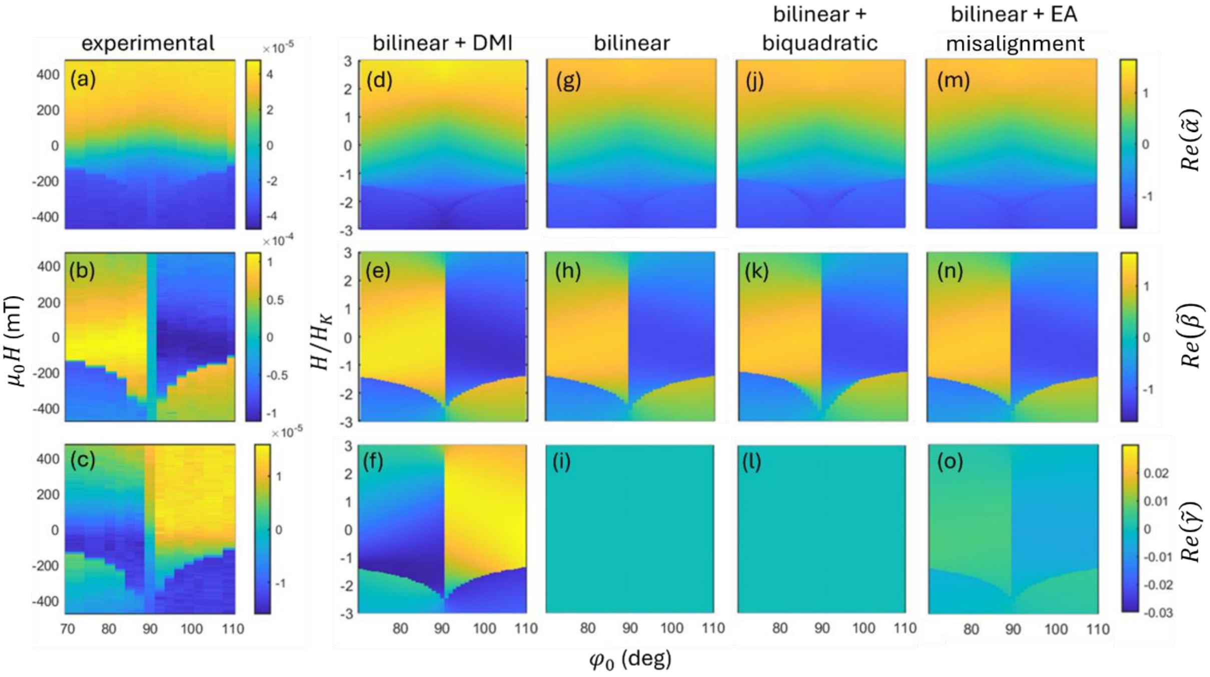

Figure 6.8 Comparison between the experimental (a-c) and calculated (d-l) MO signals for the multilayer sample represented as color-coded maps, for the real part of the MOKE parameters $\tilde{\alpha}, \tilde{\beta}$ and $\tilde{\gamma}$, *as function of* H *and* φ_0. *The calculated results represented correspond to having a bilinear and DMI interaction between the two FM layers (d-f), only a bilinear interaction (g-i), a bilinear and biquadratic interaction (j-l) and a bilinear interaction and a misalignment of the EA (m-o).*

Considering only the bilinear coupling, the behavior of the in-plane signal is successfully replicated (Fig. 6.8(g,h)), but no out-of-plane magnetization is observed (Fig. 6.8(i)). Adding the biquadratic term modifies slightly the in-plane components (Fig. 6.8(j,k)), without generating any out-of-plane magnetization (Fig. 6.8(l)). However, upon adding a DMI term to the bilinear coupling case, I successfully captured the observed emergence of a significant and non-linear out-of-plane magnetization component (Fig. 6.8(f)).

It is interesting to note that the γ signal in the very extended data range of Fig. 6.7 looks very similar to the $\tilde{\alpha}$ signal near the EA and similar orientations, but very different from $\tilde{\alpha}$ for orientation closer to the HA. This is in stark contrast with data in Fig. 6.8 that focus more on the HA behavior, for which $\tilde{\gamma}$ starts to look more like the $\tilde{\beta}$ signal. This is interesting from an overall physics perspective, but also relevant in that the $\tilde{\gamma}$ signal cannot simply be a misidentified $\tilde{\alpha}$ or $\tilde{\beta}$ signal.

For the calculations shown in Fig. 6.8(d-f), the DMI vector considered was $\vec{D} = (1,1,1) \cdot \frac{1}{\sqrt{3}}$, which fits best to the experimental results. This can be observed in Fig. 6.9, where I show a comparison of the different components of the $\vec{D}$ vector, each having a different impact on the out-of-plane magnetization. Figures 6.9 (a-c), representing the $\vec{D} = (0,0,0)$ case, and (m-o), representing the $\vec{D} = (1,1,1) \cdot \frac{1}{\sqrt{3}}$ case, are replicated from Figs. 6.8(g-i) and (d-f), included again here to have the full comparison of the $\vec{D}$ dependence on the signal pattern.

Another possible source of a non-linear out-of-plane signal could be a misalignment of the EA, not being perfectly in-plane but having a small out-of-plane deviation. Calculations replicating this case are also considered in Fig 6.8(m-o), with the EA having an out-of-plane deviation of 1 deg. The features experimentally observed are not replicated in this geometry. No other consideration investigated here could explain the experimental data.

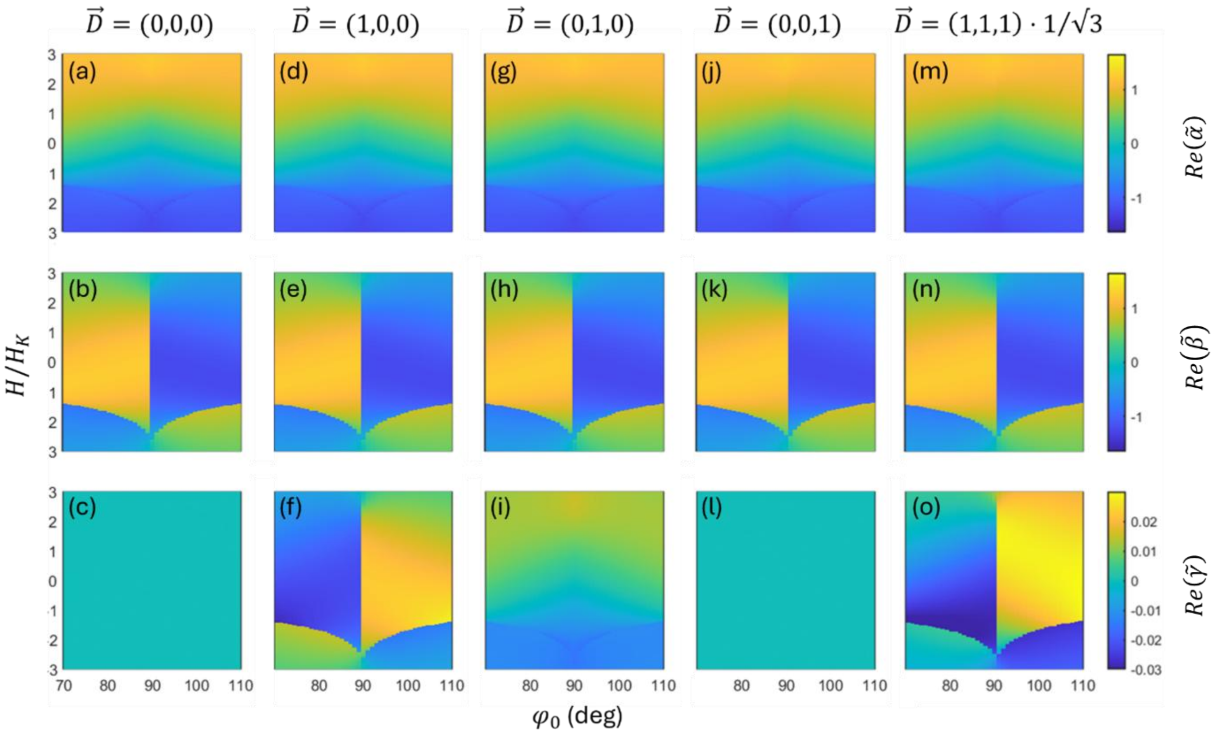

Figure 6.9 Calculated MO signals for the individual components of the DMI vector, with (a-c) having $\vec{D} = 0$, (d-f), (g-i) and (j-l) having a DMI vector with only one cartesian component, and (m-o) having a $\vec{D} = (1,1,1) \cdot 1/\sqrt{3}$.

The total magnetic vector of the system was considered as $\vec{m} = 0.75\,\vec{m_1} + 0.25\,\vec{m_2}$, as experimentally, the MO signal of the second layer is attenuated by the layers above it. The superposition assumption approximation of the MOKE parameters was also verified with the transfer matrix method, similarly as it was done in Chapter 5. Therefore, I calculated the MOKE signal of the sample by means of the 4×4 transfer matrix method in two ways. First, I performed the calculation in the numerical accurate way, by reproducing each layer of the sample. In a second calculation, I then mimic the superposition approach, calculating the individual layer responses, assuming each time that only one of the FM layers is actually MO active, and then add up the two single layer contributions to compare the sum to the exact result.

I display the computation results, including the exact calculations, the superposition approach and the difference between them, as a function of $H/H_{K_{m_1}}$ in Fig. 6.10 for the three cases considered: bilinear + DMI, bilinear and bilinear + biquadratic. The first row includes the results obtained for $Re(\tilde{\alpha})$, the second row shows the corresponding data for $Re(\tilde{\beta})$ and the last row represents $Re(\tilde{\gamma})$. The different columns refer to different EA orientation angles, $\varphi_0 = 79$, 92 and 105 deg. For the bilinear and bilinear+biquadratic cases, only the $\varphi_0 = 105$ deg case is shown, as it serves the purpose of showing the deviations between superposition approach and exact solutions for those cases (other angle orientations presented similar results). Indeed, the deviations in between the superposition approach and exact solutions are extremely small, namely four orders of magnitude smaller than the actual values, similarly as it was shown in Chapter 5 for the in-plane collinear and non-collinear cases. The deviations are consistently found to be extremely small and do not show any feature that could be misinterpreted as a polar signal.

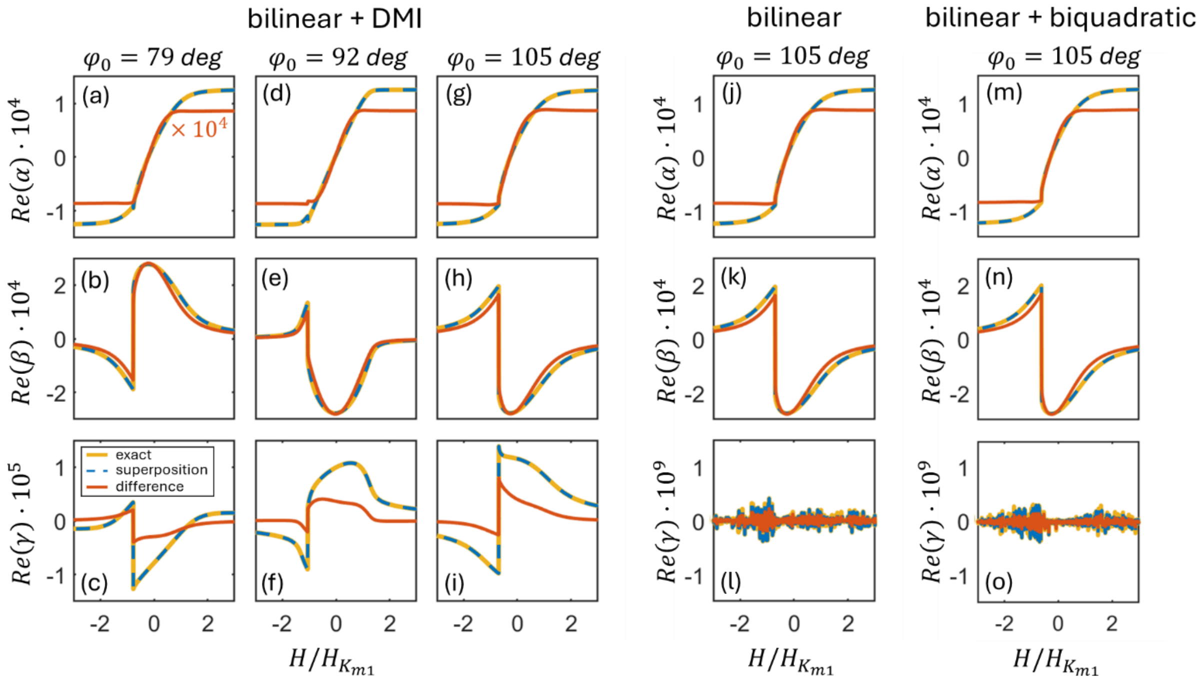

Figure 6.10 Numerical results of the exact optical multilayer simulation of the MOKE signal in comparison to the layer superposition approximation and the difference between these two calculations (10^4 times smaller) for the bilinear+DMI calculated magnetization angles. Specifically, the figures show the real part of $\tilde{\alpha}, \tilde{\beta}$ and $\tilde{\gamma}$ for three different angular orientations of the EA.

6.2.4 Conclusions and outlook

I have experimentally and theoretically demonstrated the emergence of a substantial out-of-plane MOKE signal in a nominally in-plane exchange-coupled multilayer. My systematic GME measurements indicate that such signals cannot be accounted for by bilinear or biquadratic terms alone. Instead, only the inclusion of a IL-DMI term coupling of the two FM layers explains the observed three-dimensional magnetization response.

Although $Co_{0.59}Ru_{0.41}$ is not typically considered a heavy element system, prior work has shown that the Ru 4d states can still provide sufficient spin-orbit scattering for a DMI-like coupling when combined with local asymmetry or epitaxial alignment [27,37,39]. As such, the unexpectedly robust out-of-plane magnetization in our intermediate-thickness trilayer underscores the need to look beyond purely bilinear or biquadratic coupling in modest spin-orbit platforms.

Overall, this work expands the understanding of IL-DMI interactions in multilayered systems and demonstrates the sensitivity of GME in detecting such effects by measuring the full vectorial information of the magnetization vector. These findings open possibilities of tailoring and measuring IL-DMI. Moreover, a key aspect is the vectorial nature of the DMI and that the observed results are apparently very sensitive to the D-vector orientation. So, in principle the acquired data sets can have the potential to actually measure the DMI vector orientation for interlayer coupling.

Chapter references

[1] C. Martín Valderrama, M. Quintana, and A. Berger, Experimental verification of the reflection matrix description in linear magneto-optics, Phys. Rev. B **108**, 014415 (2023).

[2] J. A. Arregi, P. Riego, and A. Berger, What is the longitudinal magneto-optical Kerr effect?, J. Phys. D. Appl. Phys. **50**, 03LT01 (2017).

[3] T. Higo et al., Large magneto-optical Kerr effect and imaging of magnetic octupole domains in an antiferromagnetic metal, Nat. Photonics **12**, 73 (2018).

[4] M. Wu, H. Isshiki, T. Chen, T. Higo, S. Nakatsuji, and Y. C. Otani, Magneto-optical Kerr effect in a non-collinear antiferromagnet Mn3Ge, Appl. Phys. Lett. **116**, (2020).

[5] H. C. Zhao et al., Large ultrafast-modulated Voigt effect in noncollinear antiferromagnet Mn3Sn, Nat. Commun. **12**, 1 (2021).

[6] T. Uchimura et al., Observation of domain structure in non-collinear antiferromagnetic Mn3Sn thin films by magneto-optical Kerr effect, Appl. Phys. Lett. **120**, 172405 (2022).

[7] W. Feng, J. P. Hanke, X. Zhou, G. Y. Guo, S. Blügel, Y. Mokrousov, and Y. Yao, Topological magneto-optical effects and their quantization in noncoplanar antiferromagnets, Nat. Commun. **11**, 1 (2020).

[8] Y. D. Kato, Y. Okamura, M. Hirschberger, Y. Tokura, and Y. Takahashi, Topological magneto-optical effect from skyrmion lattice, Nat. Commun. **14**, 1 (2023).

[9] M. V. Sapozhnikov, N. S. Gusev, S. A. Gusev, D. A. Tatarskiy, Y. V. Petrov, A. G. Temiryazev, and A. A. Fraerman, Direct observation of topological Hall effect in Co/Pt nanostructured films, Phys. Rev. B **103**, 1 (2021).

[10] X. Li et al., Topological Kerr effects in two-dimensional magnets with broken inversion symmetry, Nat. Phys. **20**, 1145(2024).

[11] R. Wiesendanger, Nanoscale magnetic skyrmions in metallic films and multilayers: A new twist for spintronics, Nat. Rev. Mater. **1**, 16044 (2016).

[12] W. Jiang, G. Chen, K. Liu, J. Zang, S. G. E. te Velthuis, and A. Hoffmann, Skyrmions in magnetic multilayers, Phys. Rep. **704**, 1 (2017).

[13] A. Fert, N. Reyren, and V. Cros, Magnetic skyrmions: Advances in physics and potential applications, Nat. Rev. Mater. **2**, 17031 (2017).

[14] M. T. Johnson, P. J. H. Bloemen, F. J. A. Den Broeder, and J. J. De Vries, Magnetic anisotropy in metallic multilayers, Reports Prog. Phys. **59**, 1409 (1996).

[15] A. Hubert and R. Schäfer, *Magnetic Domains. The Analysis of Magnetic Microstructures* (Springer-Verlag Berlin Heidelberg New York, Germany, 1998)

[16] H. J. G. Draaisma and W. J. M. De Jonge, Magnetization curves of Pd/Co multilayers with perpendicular anisotropy, J. Appl. Phys. **62**, 3318 (1987).

[17] O. Hellwig, G. P. Denbeaux, J. B. Kortright, and E. E. Fullerton, X-ray studies of aligned magnetic stripe domains in perpendicular multilayers, Phys. B Condens. Matter **336**, 136 (2003).

[18] A. Berger and M. R. Pufall, Quantitative vector magnetometry using generalized magneto-optical ellipsometry, J. Appl. Phys. **85**, 4583 (1999)

[19] A. Berger and M. R. Pufall, Generalized magneto-optical ellipsometry, Appl. Phys. Lett. **71**, 965 (1997).

[20] J. A. Arregi, *Magneto-Optical Ellipsometry and Magnetometry of Thin Films and Multilayers* (Ph.D. Thesis, University of the Basque Country, 2020).

[21] M. R. Pufall and A. Berger, Studying the reversal mode of the magnetization vector versus applied field angle using generalized magneto-optical ellipsometry, J. Appl. Phys. **87**, 5834 (2000).

[22] J. A. Arregi, P. Riego, A. Berger, and E. Y. Vedmedenko, Large interlayer Dzyaloshinskii-Moriya interactions across Ag-layers, Nat. Commun. **14**, 6927 (2023).

[23] J. Becker, A. Tsukamoto, A. Kirilyuk, J. C. Maan, T. Rasing, P. C. M. Christianen, and A. V

Kimel, Ultrafast Magnetism of a Ferrimagnet across the Spin-Flop Transition in High Magnetic Fields, **117203**, 1 (2017).

[24] J. McCord, Progress in magnetic domain observation by advanced magneto-optical microscopy, J. Phys. D. Appl. Phys. **48**, 333001 (2015).

[25] S. Mühlbauer, B. Binz, F. Jonietz, C. Pfleiderer, A. Rosch, A. Neubauer, R. Georgii, and P. Böni, Skyrmion lattice in a chiral magnet, Science. **333**, 1381 (2009).

[26] P. Grünberg, R. Schreiber, Y. Pang, M. B. Brodsky, and H. Sowers, Layered Magnetic Structures: Evidence for Antiferromagnetic Coupling of Fe Layers across Cr Interlayers, Phys. Rev. Lett. **57**, 2442 (1986).

[27] T. Matthies, L. Rózsa, L. Szunyogh, R. Wiesendanger, and E. Y. Vedmedenko, Interlayer and interfacial Dzyaloshinskii-Moriya interaction in magnetic trilayers: First-principles calculations, Phys. Rev. Res. **6**, 43158 (2024).

[28] D. M. Edwards, J. M. Ward, and J. Mathon, Intrinsic and secondary mechanisms for biquadratic exchange coupling in magnetic trilayers, J. Magn. Magn. Mater. **126**, 380 (1993).

[29] J. Daughton, J. Brown, E. Chen, R. Beech, A. Pohm, and W. Kude, Magnetic Field Sensors Using GMR Multilayer, IEEE Trans. Magn. **30**, 4608 (1994).

[30] C. Reig, M. D. Cubells-Beltrán, and D. R. Muñoz, Magnetic field sensors based on Giant Magnetoresistance (GMR) technology: Applications in electrical current sensing, Sensors **9**, 7919 (2009).

[31] I. Dzyaloshinsky, A Thermodynamic Theory of “weak” ferromagnetism of antiferromagnetics, J. Phys. Chem. Solids **4**, 241 (1958).

[32] T. Moriya, Anisotropic superexchange interaction and weak ferromagnetism, Phys. Rev. **120**, 91 (1960).

[33] A. R. Fert, Magnetic and Transport Properties of Metallic Multilayers, Mater. Sci. Forum **59–60**, 439 (1991).

[34] E. Demiroglu, K. Hancioglu, I. Yavuz, C. O. Avci, and C. Deger, Oscillatory behavior of interlayer Dzyaloshinskii-Moriya interaction by spacer thickness variation, Phys. Rev. B **109**, 144422 (2024).

[35] F. Nickel, S. Meyer, and S. Heinze, Exchange and Dzyaloshinskii-Moriya interaction in Rh/Co/Fe/Ir multilayers: Towards skyrmions in exchange-frustrated multilayers, Phys. Rev. B **107**, 174430 (2023).

[36] S. D. Pollard, J. A. Garlow, K. W. Kim, S. Cheng, K. Cai, Y. Zhu, and H. Yang, Bloch Chirality Induced by an Interlayer Dzyaloshinskii-Moriya Interaction in Ferromagnetic Multilayers, Phys. Rev. Lett. **125**, 227203 (2020).

[37] C. O. Avci, C. H. Lambert, G. Sala, and P. Gambardella, Chiral Coupling between Magnetic Layers with Orthogonal Magnetization, Phys. Rev. Lett. **127**, 167202 (2021).

[38] R. B. Morgunov, A. I. Bezverkhnii, M. Hehn, J. L. Bello, T. Fache, and S. Mangin, Dzyaloshinskii-Moriya interaction probed by magnetization reversal in bilayer Pt/Co/Ir/Co/Pt synthetic ferrimagnets, Phys. Rev. B **104**, 134424 (2021).

[39] Y. C. Li, Y. H. Huang, C. C. Huang, Y. T. Liu, and C. F. Pai, Field-Free Switching in Symmetry-Breaking Multilayers: The Critical Role of Interlayer Chiral Exchange, Phys. Rev. Appl. **20**, 024032 (2023).

[40] C. Y. Lin, P. C. Wang, Y. H. Huang, W. B. Liao, M. Y. Song, X. Bao, and C. F. Pai, Field-Free Spin-Orbit Torque Switching via Oscillatory Interlayer Dzyaloshinskii-Moriya Interaction for Advanced Memory Applications, ACS Mater. Lett. **6**, 400 (2024).

[41] S. Liang, R. Chen, Q. Cui, Y. Zhou, F. Pan, H. Yang, and C. Song, Ruderman-Kittel-Kasuya-Yosida-Type Interlayer Dzyaloshinskii-Moriya Interaction in Synthetic Magnets, Nano Lett. **23**, 8690 (2023).

[42] W. He et al., Field-Free Spin-Orbit Torque Switching Enabled by the Interlayer Dzyaloshinskii-Moriya Interaction, Nano Lett. **22**, 6857 (2022).

[43] J. Cho et al., Thickness dependence of the interfacial Dzyaloshinskii–Moriya interaction in

inversion symmetry broken systems, Nat. Commun. **6**, 7635 (2015).

[44] C. Martín Valderrama, I. Prieto, M. Quintana, A. Martínez-de-Guerenu, and A. Berger, Layer-resolved vector magnetometry using generalized magneto-optical ellipsometry, Appl. Phys. Lett. **125**, 022401 (2024).

[45] C. Martín Valderrama, I. Prieto, M. Quintana, and A. Berger, Magneto-optical detection of non-collinear magnetization states in ferromagnetic multilayers, J. Phys. D. Appl. Phys. **57**, (2024).

[46] O. Idigoras, U. Palomares, A. K. Suszka, L. Fallarino, and A. Berger, Magnetic properties of room temperature grown epitaxial Co 1-xRux-alloy films, Appl. Phys. Lett. **103**, 102410 (2013).

[47] O. Idigoras, A. K. Suszka, P. Vavassori, B. Obry, B. Hillebrands, and P. Landeros, Magnetization reversal of in-plane uniaxial Co films and its dependence on epitaxial alignment, **115**, 083912 (2014).

[48] L. Fallarino, P. Riego, B. J. Kirby, C. W. Miller, and A. Berger, Modulation of Magnetic Properties at the Nanometer Scale in Continuously Graded Ferromagnets, Materials (Basel). **11**, 251 (2018).

Chapter 7
Conclusions and outlook

This thesis presents significant advancements in the experimental methodologies for the detection and characterization of depth-dependent vector magnetization states in nanoscale multilayers, particularly through the use of generalized magneto-optical ellipsometry (GME) to achieve layer-resolved vector magnetization. By establishing a solid framework based on the experimental verification of the reflection matrix description for linear magneto-optical (MO) effects and verifying and identifying the limits of the layer superposition assumption, this work effectively demonstrates the ability to probe complex and intricate spin configurations that play a crucial role in the ongoing evolution of spintronic technologies.

The conclusions drawn from this work highlight GME as a layer-resolved vector magnetometry methodology. GME demonstrates exceptional sensitivity in detecting magnetic properties at the layer level, effectively resolving contributions from two different layers in complex multilayered systems. This ability is particularly advantageous when dealing with layers of similar elemental compositions, a common challenge for competing methods, and allows for detailed insights into the magnetic behavior of multilayers. This level of resolution represents a significant advancement for studies requiring depth-dependent analysis of magnetic systems. Specifically, the work presented in this thesis demonstrates the capability of GME to identify and characterize non-collinear magnetization vectors in ferromagnetic (FM)/ non-magnetic (NM)/ FM multilayers, marking a substantial step towards understanding the depth-dependent behavior of magnetization states. Although technical constraints did not allow for an in-depth evaluation of the next step in multilayer systems with three FM layers, the groundwork laid provides a clear path for future explorations that could incorporate additional layers.

The findings of this research highlight the sensitivity of MO coefficients to variations in magnetization profiles, which offers a compelling tool for exploring the complexities of multilayer systems. Notably, the study on asymmetric Pt/Co/Tb/W multilayers made significant contributions to understanding how Dzyaloshinskii-Moriya interaction (DMI) and effective magnetic anisotropy can influence magnetization states. The detection of non-uniform magnetization states and its relationship with the out-of-plane MO signal paves the way for future research into topological magnetic states, such as skyrmions, presenting GME as a promising tool for further investigations in this area. Moreover, I observed DMI interlayer effects in multilayer films that were actually not specifically designed for this purpose and whose deviation from inversion symmetry is rather modest. Thus, it is possible that interlayer DMI is far more common than what prior research suggests, and might frequently be overlooked, because one does not typically have 3D vector magnetometry at one's disposal and certainly layer resolved vector magnetometry is especially relevant in discovering such effects. Therefore, the methodological advance shown in this work opens up the possibility of many more wide-reaching investigations of interlayer DMI.

The foundation established through this research positions GME as a powerful tool for future investigations into complex magnetic systems. I present here an outlook of three different examples of magnetic systems that we have already started to study with GME:

(i) Composition-graded FM thin films, which are relevant for technological applications upon suitable design of the graded profile [1-4]. By growing a similar epitaxial structure as the two FM layer samples utilized for non-collinear detection and layer-resolved magnetometry, but with a gradient of composition, changing from a pure Co to a Co-Pt alloy gradually over a thickness of 20 nm, as represented by the schematic inset of Fig. 7.1(c), a phase deviation related with non-collinear magnetic states can be observed. In these structures, instead of having two well defined magnetization vectors that can rotate independently, there is a “continuous” profile of magnetization vectors along the depth representing a “continuous” profile of orientations. Figure 7.1(c) includes the phase deviation of $\tilde{\alpha}$ and $\tilde{\beta}$ of such sample design, indicative of a change of collinear to non-collinear magnetization alignment, in comparison to a single FM layer sample (Fig. 7.1(a)) and a two FM layer sample (Fig. 7.1(b)), already studied in Chapter 5.

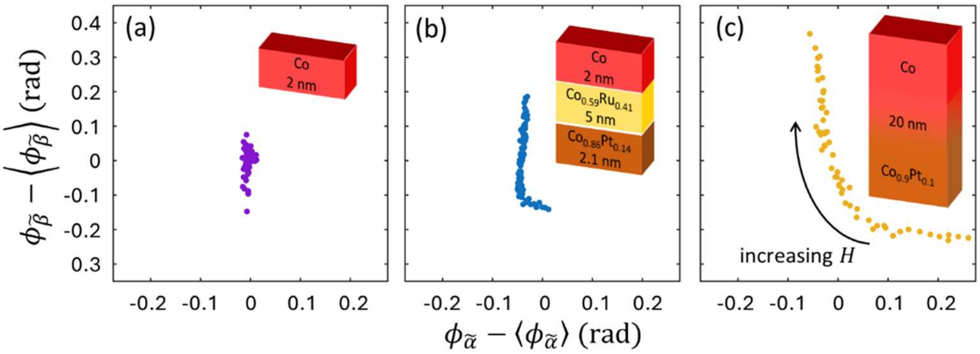

Figure 7.1 Experimentally determined $\phi_{\tilde{\beta}} - \langle\phi_{\tilde{\beta}}\rangle$ *vs.* $\phi_{\tilde{\alpha}} - \langle\phi_{\tilde{\alpha}}\rangle$ *values for all magnetic field* H *values in the thermodynamically stable regime, measured for a single Co FM layer sample (a), for a two FM layer sample separated by a NM layer (b) and for a graded sample (c); the respective main layers of the structures are schematically included in each subfigure; (c) includes an arrow indicating the increasing* H *direction with which the quantities evolve as a guide to the eye.*

(ii) Partially epitaxial FM films, consisting of thin films exhibiting moderate deviations from single-crystal behavior. A control of the intermediate regime between fully epitaxial and highly disordered polycrystalline films is the goal in this kind of samples. By introducing a SiO_2 layer right before the template layer sequence designed to achieve the epitaxial growth of Co, the epitaxial quality can be tuned [5]. The specific layers of a fully and partially epitaxial sample are represented in Fig. 7.2(a) and (f), respectively. The partially epitaxial sample was generated, as an exemplary case, by means of a 0.1 nm thick SiO_2 interlayer.

For this kind of samples, near the hard axis (HA), an anomalous magnetization reversal behavior was found in previous studies [5-7], which can be observed in the remanent magnetization represented in Fig. 7.2(g), compared with the ideal case in Fig. 7.2(b). Now, with the vector magnetization capabilities of GME, a better understanding of the magnetization behavior in this regime is achieved. Figures 7.2(c,d,h,i) include the real part of the in-plane MO parameters $\tilde{\alpha}$ and $\tilde{\beta}$ for two φ_0 sample orientations. The $\tilde{\beta}$ value for $\varphi_0 = 91$ deg shows a reduction when compared to the $\varphi_0 = 94$ deg case for the partially epitaxial sample (Fig. 7.2(i)). This reduction in $\tilde{\beta}$ is not observed in the fully epitaxial sample (Fig. 7.2(d)). By fitting the experimentally determined $\tilde{\alpha}$ and $\tilde{\beta}$ values to an effective magnetization vector of variable orientation and length, the absolute value and the rotation of the magnetization are extracted as a function of the applied field H and sample orientation φ_0. The results of the absolute value of the magnetization of the fully and partially epitaxial samples are included in Fig. 7.2(e) and (j), respectively, clearly observing a magnetization reduction in the partially epitaxial sample near the HA orientation. The magnitude of the magnetization for the fully epitaxial sample remains constant, but for non-stable situations as when the applied field orientation aligns precisely with the HA and during the transitions from meta-stable to stable states. These results have already been partially presented in [8].

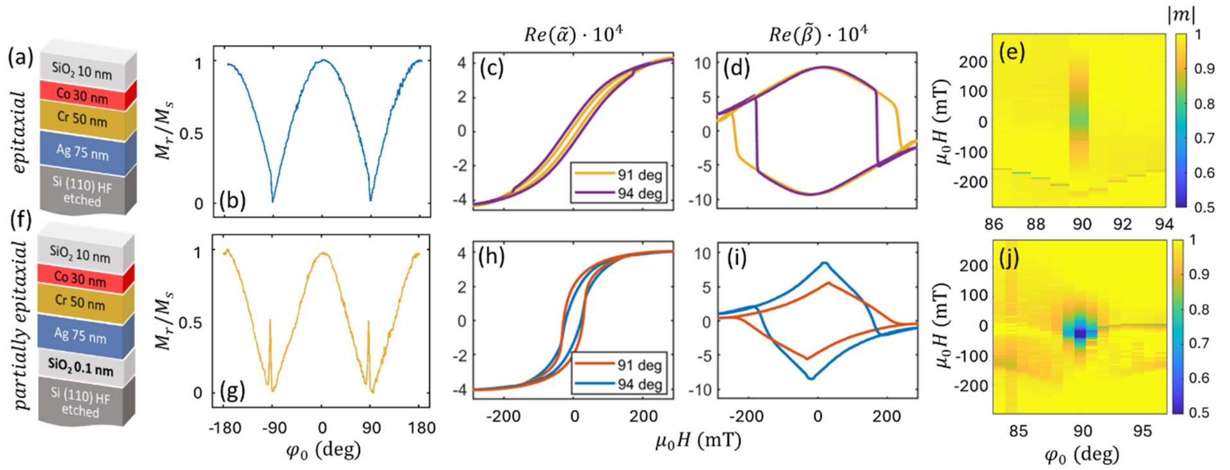

Figure 7.2 Fully and partially epitaxial samples results: (a) and (f) represent the layer structures, (b) and (g) the M_r/M_s dependence with the sample orientation, (c,d,h,i) the in-plane MO paraments and (e) and (j) the absolute value of the magnetization $|m|$ as a function of the applied field H and the sample orientation φ_0.

(iii) Multilayer samples with both in-plane and out-of-plane anisotropies. This orthogonal structure serves to test the abilities of GME of resolving another type of complex magnetization vector structures. The specific layer structure is included in Fig. 7.3(a), with the in-plane and out-of-plane anisotropies indicated. The initial GME results are represented in Fig. 7.3(b) and (c) for different out-of-plane orientations Ψ of the applied magnetic field with respect to the sample plane. Although the in-plane component $\tilde{\alpha}$ remains nearly the same for all Ψ, the out-of-plane component $\tilde{\gamma}$ shows a variation with Ψ. Further studies should be done to understand the overall magnetization vector behavior and the interaction between the in-plane anisotropy layer and out-of-plane anisotropy multilayer structure, as biquadratic magnetic coupling may occur.

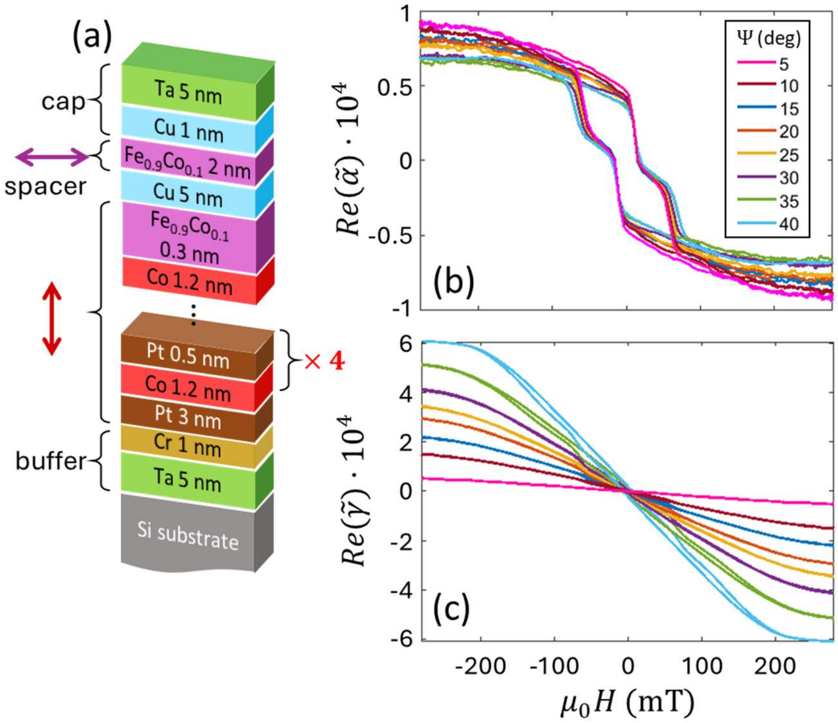

Figure 7.3 (a) Multilayer sequence of the sample, (b) and (c) real part of $\tilde{\alpha}$ *and* $\tilde{\gamma}$ *for different* Ψ *orientations as a function of the applied field* H*.*

Enhancements in measurement capabilities and the integration of broader parameter spaces, such as varying angles of incidence and wavelengths, has the potential to enable the quantitative, depth-resolved analysis of even more intricate multilayer structures. Furthermore, investigating the interplay between magnetization dynamics and external perturbations, such as temperature and current, could enhance the understanding of spintronic devices under operational conditions. As research in spintronics and magnetic technologies advances, GME has the clear potential to play a crucial role in unlocking new insights into the behavior of magnetic materials at the nanoscale.

Chapter references

[1] B. Saleh, et al., 30 years of functionally graded materials: an overview of manufacturing methods, applications and future challenges, Composites B **201** 108376 (2020).

[2] W. Li and B. Han, Research and Applications of Functionally Gradient Materials, Conf. Ser.: Mater. Sci. Eng. **394** 022065 (2018).

[3] L. Fallarino, B. J. Kirby, and E. E. Fullerton, Graded magnetic materials, J. Phys. D: Appl. Phys. **54**, 303002 (2021).

[4] M. Quintana, *Phase Transitions in Nanoscale Designed Magnetic Thin Films*, (Ph.D. Thesis, University of the Basque Country, 2023)

[5] O. Idigoras, A. K. Suszka, P. Vavassori, P. Landeros, J. M. Porro, and A. Berger, Collapse of hard-axis behavior in uniaxial Co films, Phys. Rev. B **84**, 132403 (2011)

[6] S. Kaushik et al., Growth-induced magnetic anisotropy in Co/C60 bilayers: In sights from a two-grain Stoner-Wohlfarth model, Phys. Rev. B **111**, 184426 (2025)

[7] M. Sedrpooshan et al., Magneto-optical study of anomalous magnetization reversal in the presence of anisotropy dispersion in CoPd thin films, Phys. Rev. B **98,** 214444 (2018)

[8] I. Garamendia, *Magneto-optical vector magnetometry of partially epitaxial films in the vicinity of their hard axis anomaly*, (Master Thesis, University of the Basque Country, 2025)

List of Abbreviations

Abbreviations are not listed here if they occur only in the immediate context of a statement.

AC	Alternating current
CPL	Circularly polarized light
DC	Direct current
DMI	Dzyaloshinskii-Moriya interaction
EA	Easy axis
FM	Ferromagnetic
GME	Generalized magneto-optical ellipsometry
HA	Hard axis
hcp	Hexagonal close-packed
HF	Hydrofluoric acid
IL-DMI	Interlayer DMI
L-MOKE	Longitudinal magneto-optical kerr effect
MCA	Magneto-crystalline anisotropy
MO	Magneto-optical
MOKE	Magneto-optical Kerr effect
NM	Non-magnetic
$P_{1,2}$	Linear polarizers 1, 2
PM	Paramagnetic
P-MOKE	Polar magneto-optical Kerr effect
QWP	Quarter wave plate
RF	Radio-frequency
SOC	Spin-orbit coupling
SQUID	Superconducting quantum interference device
T-MOKE	Transverse magneto-optical Kerr effect
UHV	Ultra-high vacuum
VSM	Vibrating sample magnetometry
XMCD	X-ray magnetic circular dichroism
XRD	X-ray diffraction
XRR	X-ray reflectivity

List of Variables

Variables are not listed here if they occur only in the immediate context of a statement.

Bold symbols represent tensors, symbols with an arrow on top represent vectors.

α	Longitudinal magneto-optical component of the reflection matrix
$\tilde{\alpha}$	L-MOKE coefficient divided by r_p
$\tilde{\alpha}_i$	L-MOKE coefficient associated with the FM layer “i”
$\tilde{\alpha}_0$	Complex constant describing the linear relationship between $\tilde{\alpha}$ and m_x
β	Transverse magneto-optical component of the reflection matrix
$\tilde{\beta}$	T-MOKE coefficient divided by r_p
$\tilde{\beta}_i$	T-MOKE coefficient associated with the FM layer “i”
$\tilde{\beta}_0$	Complex constant describing the linear relationship between $\tilde{\beta}$ and m_y
γ	Polar magneto-optical component of the reflection matrix
$\tilde{\gamma}$	P-MOKE coefficient divided by r_p
$\tilde{\gamma}_0$	Complex constant describing the linear relationship between $\tilde{\gamma}$ and m_z
$\Delta\theta_i$	Experimental angular offset correction of the polarizer “i”
ΔI	Change of light intensity upon magnetization reversal in a MOKE experiment
$\delta\tilde{\gamma}$	P-MOKE signal difference between the decreasing and the increasing field branch measurements
$\boldsymbol{\varepsilon}$	Dielectric tensor
ε_{Kerr}	Kerr ellipticity
θ_i	Angle of the polarizer “i”
θ	Reflected light angle with respect to the film surface
θ_{Kerr}	Kerr rotation angle
ϑ_{m_i}	Out-of-plane magnetization vector orientation angle of the FM layer “i” with respect to the normal direction of the sample surface.
λ	Wavelength of the electromagnetic radiation
$\vec{\mu}$	Magnetic moment vector
μ_0	Vacuum permeability
$\rho_{A,B}$	Density of the materials A and B
$\phi_{\tilde{\alpha}}$	Phase of the complex L-MOKE parameter $\tilde{\alpha}$
$\phi_{\tilde{\beta}}$	Phase of the complex T-MOKE parameter $\tilde{\beta}$
$\phi_{\tilde{\gamma}}$	Phase of the complex P-MOKE parameter $\tilde{\gamma}$
φ	Azimuthal angle
φ_{m_i}	In-plane magnetization vector orientation angle of the FM layer “i” with respect to the applied field direction
φ_0	Angle of the EA with respect to the applied field direction
χ	Magnetic susceptibility or angle between the normal of a sample surface and the x-rays plane of incidence
Ψ	Out-of-plane angle of the applied field with respect to the sample surface
ω	Grazing incidence angle; incident light angle with respect to the film surface
Ω	Incident light angle with respect to the surface normal
Ω'	Reflected light angle with respect to the surface normal
Ω''	Refracted light angle with respect to the surface normal

$\vec{B}$	Magnetic induction vector
B_i	Fitting parameters of GME related to the reflection matrix elements
$\vec{D}, \vec{D}_{ij}$	Dzyaloshinskii-Moriya interaction vector, DMI vector between spins “i” and “j”, with units of energy
d	Thickness of a layer or distance between crystallographic atomic planes
$\hat{e}$	Uniaxial anisotropy axis unit vector
E	Energy of a system
E_I	Incident electric field
E_D	Electric field at the detector
$\mathcal{F}$	Helmholtz free energy of a system
f_i	Trigonometric functions related to the GME methodology
$\vec{H}, H$	External magnetic field vector, external magnetic field
H_c	Coercive field
H_{cl}	Closure field
H_k	Anisotropy field
$\mathcal{H}$	Hamiltonian of a system
I	Intensity
I_{mean}	Averaged intensity detected for a magnetic state and the reversed one
I_0	Fitting parameter of GME describing noise in the light intensity
I_D	Light intensity at the detector in a MOKE experiment
J, J_{ij}	FM interlayer coupling strength, exchange constant between neighboring spins “i” and “j”
$K_{1,2}$	First and second order anisotropy constants
$k_{1,2}$	First and second order anisotropy energy densities
$\vec{k}_{i,f}$	Incident and diffracted wave vectors
L	Number of FM layers
$\vec{M}, M$	Magnetization vector, magnetization
$\vec{m}$	Normalized magnetization vector $\vec{M}/M_S$
$m_{A,B}$	Standard atomic masses of materials A and B
M_r	Remanent magnetization
M_s	Saturation magnetization
$m_{x,y,z}$	Cartesian components of the magnetization vector
N	Refractive index of a material
n	Real part of the refractive index of a material
Q	Magneto-optical coupling constant
$Q_{\parallel}, Q_{\perp}$	Magneto-optical coupling factors for magnetizations along and perpendicular to the symmetry axis
$\vec{Q}_i$	Vector of the reciprocal lattice
$\boldsymbol{R}$	Reflection matrix
r_p	p-polarized Fresnell reflection coefficient, defined as the ratio of the reflected electric field amplitude to the incident electric field amplitude for p-polarization; its value depends on the incidence angle and the refractive index
r_s	s-polarized Fresnell reflection coefficient, defined as the ratio of the reflected electric field amplitude to the incident electric field amplitude for s-polarization; its value depends on the incidence angle and the refractive index

$\widetilde{r_s}$	r_s coefficient divided by r_p
r_{pp}	Ratio of the reflected p-polarized electric field to the incident p-polarized field; in an isotropic, flat, non-magnetized material $r_{pp} = r_p$
r_{ss}	Ratio of the reflected s-polarized electric field to the incident s-polarized field; in an isotropic, flat, non-magnetized material $r_{ss} = r_s$
r_{ps}	Reflected p-polarized component generated by a s-polarized incident wave; in an isotropic, flat, non-magnetized material $r_{ps} = 0$
r_{sp}	Reflected s-polarized component generated by a p-polarized incident wave; in an isotropic, flat, non-magnetized material $r_{sp} = 0$
$\vec{S}_i$	Spin unit vector
t	Thickness of a specific layer in a multilayer structure
T	Temperature
T_c	Curie temperature
κ	Imaginary part of the refractive index of a material

List of publications

Work related to this thesis has also resulted in the following publications:

1. C. Martín Valderrama, M. Quintana, and A. Berger, Experimental verification of the reflection matrix description in linear magneto-optics, Phys. Rev. B **108**, 014415 (2023)
2. C. Martín Valderrama, I. Prieto, M. Quintana, and A. Berger, Magneto-optical detection of non-collinear magnetization states in ferromagnetic multilayers, J. of Phys. D: Appl. Phys. **57**, 315003 (2024)
3. C. Martín Valderrama, I. Prieto, M. Quintana, A. Martínez-de-Guerenu, and A. Berger, Layer-resolved vector magnetometry using generalized magneto-optical ellipsometry, App. Phys. Lett. **125**, 022401 (2024)
4. C. Martín Valderrama, M. Quintana, K. Tokunaga, Y. Urbina, Y. Kurokawa, P. Vavassori, H. Yuasa, and A. Berger, Observation of excess polar Magneto-optical Kerr Effect signals in Asymmetric Co/Tb-multilayers, accepted in App. Phys. Lett.
5. C. Martín Valderrama, I. Prieto, M. Quintana, and A. Berger, Anomalous Polar Magneto-Optical Kerr Effect observation in exchange-coupled uniaxial magnetic thin films, in preparation
6. C. Martín Valderrama, I. Garamendia, S. Kagi, and A. Berger, Hard-Axis Anomaly in Partially Epitaxial Co Films Investigated via Vector Magnetometry, in preparation

Other publications:

i. R. Weber, C. Martín Valderrama, L. Fallarino, and A. Berger, Dependence of the magneto-optical signal on the Co layer thickness asymmetry in Co/Pt/Co films, Phys. Rev. B **102**, 214434 (2020)

ii. C. Martín Valderrama, M. Quintana, A. Martínez-de-Guereñu, T. Yamauchi, Y. Hamada, Y. Kurokawa, H. Yuasa, and A. Berger, Insertion layer magnetism detection and analysis using transverse magneto-optical Kerr effect (T-MOKE) ellipsometry, J. of Phys. D: Appl. Phys. **54**, 435002 (2021)

iii. C. Martín Valderrama, M. Quintana, A. Martínez-de-Guereñu, T. Yamauchi, Y. Hamada, Y. Kurokawa, H. Yuasa, and A. Berger, Sensitivity and reproducibility of transverse magneto-optical Kerr effect (T-MOKE) ellipsometry, J. of Phys. D: Appl. Phys. **55**, 435007 (2022)

iv. M. Quintana, A. Meléndez, C. Martín Valderrama, L. Fallarino, and A. Berger, Temperature-independent coercivity in compositionally graded ferromagnetic multilayers, Phys. Rev. Appl. **18**, 054024 (2022)

v. M. Quintana, C. Martín Valderrama, and A. Berger, Metamagnetic fluctuation characteristics near dynamic phase transitions, Phys. Rev. E **108**, 064121 (2023)

Acknowledgements

They say this is the most difficult part of the writing of the thesis but also the one more enjoyable as one reflects on the past years and the journey that brought us up to this point (however, I doubt writing is enjoyable in anyway at this point…).

I want to start the acknowledgements by thanking my supervisor, Andreas Berger. This thesis would not have been possible without your help and assistance. Thank you for your time, guidance and advice. I deeply admire your scientific rigor and professionality, and I have learned a great deal from your example. I am also thankful to my supervisor from CEIT, Ane Martinez de Guereñu, always efficient and willing to help, I greatly value your support.

I am grateful to Txema Pitarke, for giving me such a nice opportunity to work and conduct my experiments at CIC nanoGUNE.

Special thanks to the Nanomagnetism group and to all the people at nanoGUNE who, in one way or another, contributed to this work and made day-to-day life in the lab both productive and enjoyable. I appreciate the engaging discussions, the technical help, the patience, and the camaraderie. Thanks to Matteo, Cesar, Irene, Iratxe, Paolo, Mikel, Ignacio, Yoav, Luciano, Jaylin, Simeon, Ralph, Roger, María, Edo, Raquel, Diana, Friedrich, Karina, Kristina, Aranzazu, Ane, Jaione, Eneko, Oksana… Extremely a big thanks here to Mikel and María, for all those sunny and rainy days together, all those coffees and hugs (I tried to take it as easy as possible…).

I gratefully acknowledge the Basque Government for the funding support that made this research possible.

This journey has taken me beyond borders. I want to thank everyone I met during my research stays at Kyushu University (Fukuoka, Japan) and at KAIST (Daejeon, South Korea), who made those experiences so enriching both professionally and personally. I thank Prof. Yuasa and Prof. Park for welcoming me and giving me the opportunity to be part of their group for a period of time.

I thank Dr. Satoshi Tomita and Dr. Olav Hellwig for reading my manuscript and for writing a favorable report and recommendation for the international PhD mention, as well as the thesis panel members for accepting to be part of the evaluation committee and for dedicating their time and expertise to assess my work.

To my friends, thank you for always being there, for encouraging me, for listening, and for reminding me of life beyond research. Thanks to Lara, Raquel, Lauri, Sofía, Karmele, Jon, Sara, Espe, Dimitri, Ana, Paco, Minha, Mer, Borja, Yvonne, Derek… To Markel (or better Prof. Arbulu?), thank you for your patience, your (very) special humor, your nice cooking abilities and your company in both the calm and the storm.

To my family, I cannot express enough how grateful I am for your unconditional support, love, and trust. Specially to my parents, Agustín and María Jesús, gracias por todo el apoyo y por mandarme toda la calma necesaria siempre que la necesitaba (¡Aurrera!).